POLITECNICO DI TORINO

Master of Science
in Mechanical Engineering

Master's Thesis

Structural Health Monitoring of Composite Materials with Optical Fibres under Fatigue Loading

Supervisors
Prof. Davide Salvatore Paolino

Candidate
Alessia Sepe

Co-supervisors
Ing. Raffaele Ciardiello
Ing. Carlo Boursier Niutta
Ing. Andrea Tridello

Academic Year 2025-2026

Contents

List of Tables

List of Figures

Chapter 1

Introduction and theoretical aspects

Structural Health Monitoring (SHM) is a growing ensemble of techniques devoted to collect and analyse data from structures in order to detect early damage, thus allowing to continuously evaluate their integrity and performance. The use of Structural Health Monitoring (SHM) is particularly challenging for composite materials due to their heterogeneous nature. The anisotropic behaviour, complex damage mechanisms, and poor visual detectability of internal defects make traditional inspection methods less effective. Among others, Distributed Fibre Optic Sensors (DFOS) represent a promising technique, ensuring full-field strain measurements with high resolution and real-time monitoring capability.

In this context, the present work investigates an innovative hybrid optical fibre designed to optimize both sensing accuracy and installation robustness. The hybrid configuration consists of alternating sections of fibres with acrylate and polyimide coatings. The central polyimide segment, which is responsible for high strain-transfer accuracy, is embedded within the composite laminate, while the acrylate-coated portions are welded to the polyimide-coated ones and positioned at the composite exit region, thereby improving handling and reducing the risk of unexpected breakage thanks to the greater flexibility of the acrylate.

To experimentally validate this design, carbon/epoxy composite specimens were manufactured using twill woven pre-pregs, with the hybrid optical fibre embedded along the longitudinal axis. Tensile tests were performed to evaluate the ability of the embedded polyimide section to accurately record mechanical strain through DFOS based on the Rayleigh backscattering principle, using the Luna ODiSI 6100 system as an interrogator. The results confirmed that the polyimide-coated region effectively captured the local strain field, enabling the determination of the elastic modulus in agreement with values previously reported for specimens instrumented with fully polyimide-coated fibres.

Subsequently, a fatigue testing campaign (tension-tension mode) was carried out to further assess the measurement capability of the DFOS under cyclic loading. The fatigue behaviour of specimens with embedded DFOS and specimens without sensors was compared to evaluate the influence of the embedded DFOS in carbon composite laminates.

Chapter 2

Composite Materials

Composite materials are combinations of two or more distinct phases: a continuous matrix that binds and protects a dispersed reinforcement, which carries the majority of the applied load. Their combined properties exceed those of the individual constituents: the matrix provides cohesion, transfers stresses, and maintains the shape and environment of the reinforcement, while the latter, typically fibre or particulate, improves the mechanical stiffness, strength and performance of the composite. A crucial role is played by the interface region between the fibre and the matrix, as it governs the efficiency of stress transfer between them, and its stiffness and strength control the onset of damage mechanisms [1, 2].

2.1 Matrix and Reinforcements Types

The matrix may be polymeric, metallic, ceramic or even carbon/carbon. In particular, metallic matrix composites usually employ aluminium, magnesium or titanium alloys as matrix, reinforced with ceramic or metallic fibres/particles to enhance high-temperature or wear properties. Ceramic matrix composites are designed for extreme temperature or corrosive environments. Carbon–carbon composites are a special case where both matrix and reinforcement are carbon, used in very high temperature or aerospace applications [2].

Among these materials, polymeric matrix composites (PMCs) are widely used due to their low density and manufacturability [3]. They typically employ either thermosetting or thermoplastic matrices, each exhibiting distinct characteristics. The selection between these matrix families significantly influences the composite's performance and long-term durability.

Thermosetting matrices, such as epoxy, polyester and vinyl ester resins, undergo an irreversible curing reaction during processing. As noted in the manufacturing overview by Wu et al. [4], thermosets polymerise through crosslinking, forming a three-dimensional network that, once cured, cannot be remelted. This permanent molecular structure provides high dimensional stability, good thermal and chemical resistance, excellent adhesion to fibres, and stiffness.

Thermoplastic matrices (e.g., polypropylene, nylon, PEEK), on the other hand, do not undergo crosslinking. Instead, they consist of linear or branched polymer chains which soften upon heating and solidify upon cooling without significant chemical change. Their processability is therefore reversible, allowing remelting and reshaping, granting an advantage for repair, recycling and automated processing [5]. They offer enhanced toughness, impact resistance and fatigue tolerance. Moreover, their ability to deform plastically without catastrophic cracking makes thermoplastic composites attractive for applications requiring damage tolerance and repeated loading. As highlighted in advanced composite reviews [6], the ductility of thermoplastics contributes to improved interlaminar toughness compared to more brittle thermoset matrices.

Regarding the reinforcement, synthetic fibres such as carbon and glass remain dominant in high-performance composites [6]. Other fibre materials include basalt or natural fibres (such as flax, hemp, bamboo) that are growing interest due to sustainability and lighter weight, and hybrid reinforcements (mixtures of fibre types or sizes) used to tailor multi-directional reinforcement or to reduce cost/weight while retaining performance [7].

2.2 Reinforcement Layout

The architecture of the reinforcement phase in fibre- or particulate-reinforced composites is a key design variable influencing the mechanical performance. The “architecture” refers to the spatial arrangement, orientation, length, continuity, and stacking sequence (for laminate structures) of the reinforcement relative to the matrix [8].

In the case of fibre-reinforced polymer matrix composites, typical layouts include:

- Unidirectional (UD): all fibres aligned in a single direction. This maximises stiffness and strength in the fibre direction, at the expense of transverse properties [8].

- Cross-ply or angle-ply laminates: plies with fibres at different orientations (e.g., 0°, 90°, ±45°) are stacked to tailor more isotropic or multi-directional behaviour. It has been observed that fibre orientation strongly influences tensile and compressive performance [9].

- Woven or fabric reinforcements: fibres are woven in two (or more) directions (warp/weft) to provide in-plane strength in more than one direction and better damage tolerance [10].

- Three-dimensional (3D) architectures: the reinforcement may include through-thickness reinforcements (e.g., Z-pins, stitched fibres) or functionally graded fibre orientations (e.g., helicoidal laminates) to improve out-of-plane strength and delamination resistance [9].

- Short/discontinuous fibre mats or random fibre mats: the reinforcement is not continuous, and orientation may be random or semi-aligned; this arrangement produces more nearly isotropic mechanical behaviour but at lower level of performance compared to continuous aligned fibres [8].

The stacking sequence and fibre architecture influence not only in-plane modulus and strength, but also failure mechanisms (fibre breakage, matrix cracking, fibre-matrix debonding, delamination). For instance, woven fabrics provide improved delamination resistance compared to UD plies [10]. The design of fibre architecture is therefore also a mean to tailor damage tolerance.

Moreover, the fibre volume fraction and packing arrangement (e.g., square vs hexagonal, fibre spacing) are also part of architecture considerations, as they influence the effective properties and load transfer.

2.2.1 Woven Reinforcement

Among the various reinforcement architectures used in composite materials, woven fabrics represent a particularly important class and are also the configuration adopted in the present work. In this layout, fibres are interlaced along two orthogonal directions, warp and weft, forming a balanced system capable of carrying in-plane loads along both axes [10].

The woven interlacing inevitably introduces fibre crimp, which leads to a modest reduction in tensile stiffness with respect to UD laminates. This drawback is compensated, however, by gains in shear performance, impact and delamination resistance. Moreover, the woven architecture promotes frictional interactions between yarns, thereby enabling energy-dissipating failure processes. Chowdhury et al. [10] highlight that this combination makes woven composites particularly suitable for panels, shells, and other components subjected to complex, multi-directional service loads.

Furthermore, woven fabrics allow improved handling during lay-up, reducing fibre misalignment and simplifying the stacking of large plies. Indeed, woven reinforcements help maintain consistent fibre angles during manufacturing, enhancing laminate uniformity and reducing process-induced defects [10].

Woven reinforcements can be produced using various weave patterns that govern the interlacing sequence between warp and weft yarns [10]:

- Plain Weave: the simplest and most tightly interlaced pattern, each warp yarn alternates over and under each weft yarn in a 1×1 sequence. The structure provides high stability and low fabric distortion, excellent resistance to delamination, but also relatively high fibre crimp, which slightly reduces tensile stiffness.

- Twill Weave: it follows a repeating pattern such as 2×2 (i.e., the warp passes over two fibres and under two). This creates the characteristic diagonal “twill line”. They exhibit lower crimp and higher drapability compared to plain weave, an improved conformability to complex geometries and higher in-plane strength due to more aligned fibres. Twill fabrics often provide a balance between mechanical performance and ease of lay-up, making them attractive in aerospace and automotive laminates.

- Satin Weave: they have long floats where warp or weft yarns pass over several yarns before interlacing again. This creates very low fibre crimp, high smoothness and excellent drapability, and higher tensile stiffness than plain and twill due to straighter fibres.

- Basket and Other Variants: basket weaves are a variation of plain weave where yarns are grouped which increase flexibility and reduce crimp while preserving stability.

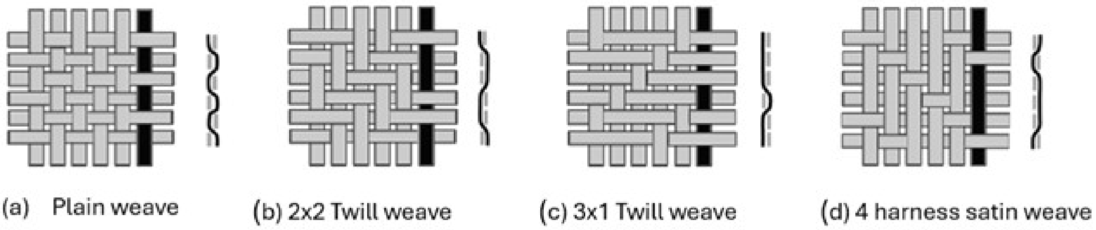

Figure 2.1: Different Woven Weaves [11].

2.3 Production Technologies for Polymer Matrix Composites

The manufacturing processes for polymer matrix composites (PMCs) play a decisive role in influencing defect formation, residual stresses and long-term durability; indeed, the process must ensure adequate wetting of the reinforcement, appropriate consolidation pressure, and controlled resin flow to avoid defects such as porosity, delamination and resin-rich areas [5]. Production technologies for PMCs can generally be categorised into open-mould, closed-mould, continuous, and advanced automated processes, each suited to specific fibre architectures and levels of performance.

2.3.1 Open-Mould Processes

Hand Lay-Up and Spray Lay-Up

Hand lay-up remains one of the most common and accessible technologies for fabricating large but relatively low-performance components. Dry reinforcement fabrics (woven cloths, mats, or UD layers) are manually placed in an open mould and impregnated with a liquid thermosetting resin using roller or brushes to promote impregnation. Air is removed mechanically and by gentle pressure. Subsequently, additional layers may be stacked until the target laminate thickness is achieved. The laminate is then covered with a release film and breather material before curing at room temperature or in an oven. Once cured, the part is demoulded and trimmed for finishing. This method, while simple and cost-effective, often results in higher void content, less uniform fibre distribution, and lower reproducibility because it suffers from operator-dependent quality, limited control over resin content [5, 12].

Spray lay-up is a variation where chopped fibres and resin are sprayed simultaneously onto the mould. While suitable for non-structural components, this approach further limits control over fibre orientation and resin content [13].

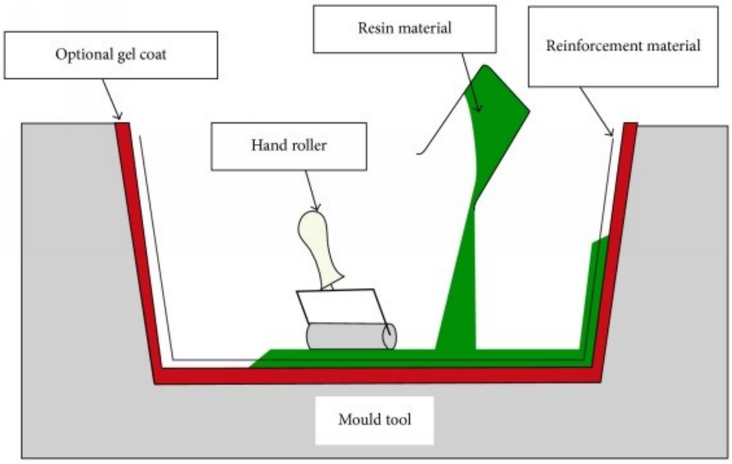

Figure 2.2: Hand lay-up process [14].

Vacuum Bagging

Vacuum bagging is an improvement of hand lay-up in which the impregnated reinforcement is sealed under a vacuum bag. Pulling vacuum extracts air and excess resin, compresses the stack and improves consolidation. The reduced pressure also helps drive the resin into the fabric, lowering void content relative to hand lay-up, although the reproducibility still depends on the operator's skill [12].

2.3.2 Closed-Mould Processes

Closed-mould processes improve dimensional accuracy, reduce emissions, and provide better consolidation than open moulding.

Resin Transfer Moulding (RTM)

RTM is a closed-mould process in which a dry fibre preform is placed inside a rigid mould, which is then sealed. A thermosetting resin is injected under controlled pressure to impregnate the reinforcement, after which the part is cured inside the mould. RTM is a scalable process suitable for medium–high production volumes, offering much better control over fibre volume fraction, surface quality, and dimensional stability compared to hand lay-up [5]. However, complete impregnation of dense or complex reinforcements can still be challenging. Preform architecture and permeability strongly influence resin flow, making process modelling essential for high-quality components.

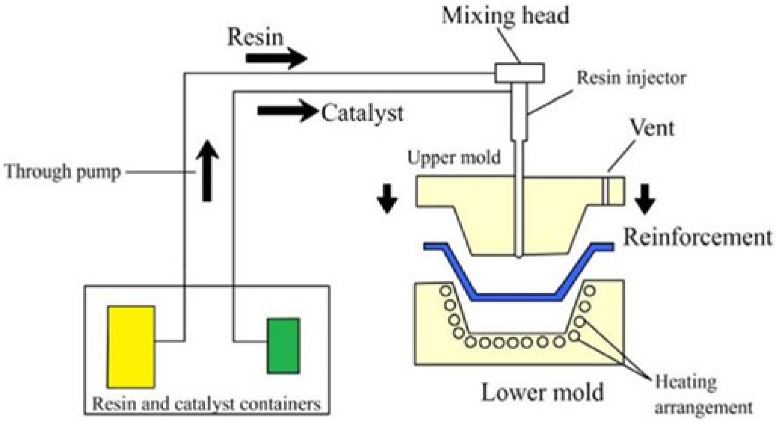

Figure 2.3: Resin Transfer Moulding (RTM) [15].

Vacuum-Assisted Resin Transfer Moulding (VARTM)

VARTM is a lower-pressure variation that uses vacuum to draw resin through the dry preform instead of injection pressure. The fibre stack is positioned on an open mould and sealed with a vacuum bag. Resin is introduced from one side and is pulled across the preform by the vacuum gradient. This method is widely used for large structures (e.g., marine hulls, wind turbine blades) due to its lower tooling costs and ability to produce large monolithic parts. Although VARTM can reduce void content relative to hand lay-up, control over local fibre wet-out and resin distribution remains a challenge, especially for thick laminates [5].

Compression Moulding

Compression moulding employs pre-mixed charges of fibre-filled thermosetting material, such as Sheet Moulding Compound (SMC) or Bulk Moulding Compound (BMC). The mould is preheated, and the charge is placed inside; the mould then closes under high pressure, forcing the material to flow and conform to the cavity. This method is ideal for high-volume automotive applications due to its short cycle times and good dimensional consistency, though performance is lower than continuous-fibre laminates [13].

2.3.3 Prepreg Processing

Pre-impregnated reinforcements represent one of the most advanced technologies for polymer composites. Fibres are pre-impregnated with a B-stage thermosetting resin, meaning that the matrix is partially cured to a tacky, semi-solid state that ensures easy handling, controlled resin content, and proper consolidation during the final curing cycle. These prepreg plies are laid up in the desired stacking sequence within a mould, vacuum-bagged or sealed, and then cured [5].

Prepregs ensure precise control over resin content, fibre alignment, and laminate quality.

Autoclave Curing

The prepreg lay-up is placed under vacuum and cured in an autoclave under elevated pressure and temperature. Autoclave curing ensures exceptional consolidation, minimal voids, and high structural integrity, making it the preferred process in aerospace and high-performance automotive components [5].

Out-of-Autoclave (OoA) Systems

Recent developments include out-of-autoclave prepregs, which cure under vacuum only, eliminating the need for costly autoclaves while still achieving relatively low void content. These systems broaden the industrial applicability of prepregs without compromising consistency.

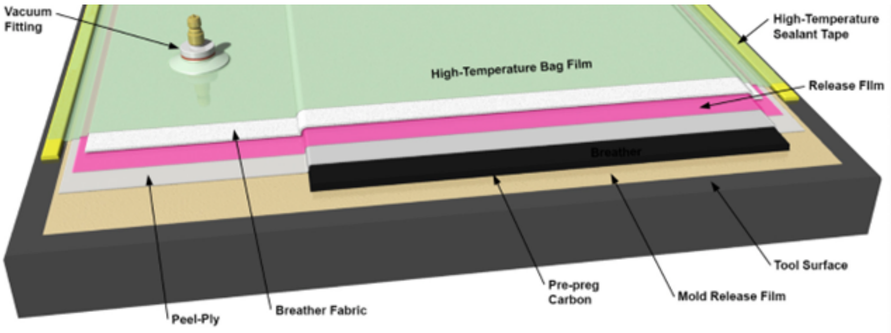

Figure 2.4: Prepreg Lay-up [16].

2.3.4 Continuous Processing Technologies

Pultrusion

Pultrusion is a continuous process in which reinforcing fibres are aligned and pulled from creel bobbins through a resin impregnation bath or injection system. The resin-soaked reinforcements then pass through shaping guides (pre-forming) and enter a heated die where the thermoset resin cures, resulting in constant cross-section profiles. After exiting the die, the continuous profile is cut to length. This method offers high throughput, excellent fibre alignment, and low production cost per unit, making it ideal for constant-section profiles such as rods and beams [13]. Its limitation lies in its restriction to prismatic geometries.

Filament Winding

Filament winding involves winding resin-impregnated fibre tows around a rotating mandrel. This process is widely used to produce pressure vessels, pipes and cylindrical structures. The winding angle can be precisely controlled, allowing excellent tailoring of hoop and axial stiffness. It enables high-fibre-volume components with good surface quality [5].

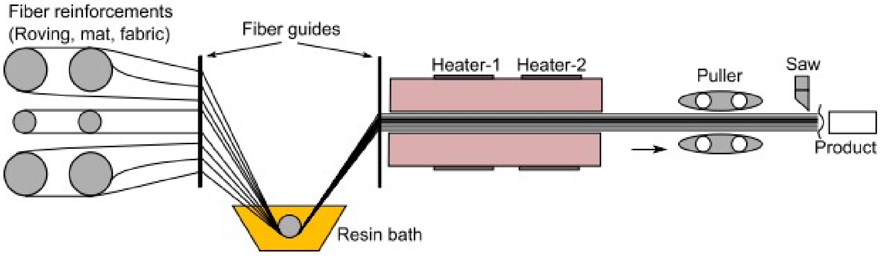

Figure 2.5: Thermosetting Pultrusion Process [17].

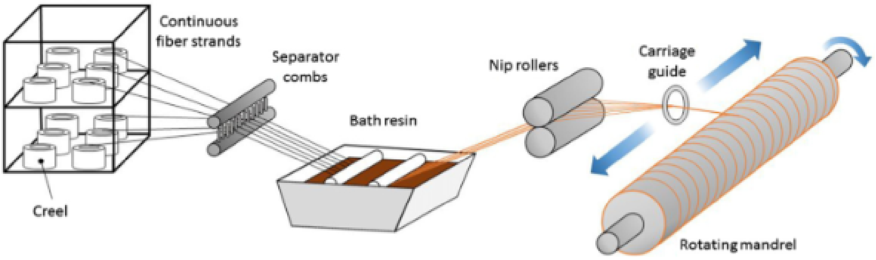

Figure 2.6: Filament winding process [18].

2.3.5 Advanced Automated Manufacturing

Automated Fibre Placement (AFP) and Automated Tape Laying (ATL)

AFP and ATL systems automate the placement of prepreg tows or tapes, enabling precise fibre orientation, reduced labour, and increased repeatability. AFP is especially advantageous for producing curved or variable-thickness laminates with complex fibre trajectories, reducing defects such as gaps and overlaps [19]. Automated methods also increase throughput and suitability for large aerospace components or high-rate production environments.

Additive Manufacturing of Composites

Although still emerging, additive manufacturing techniques for continuous- and short-fibre composites offer potential advantages in design freedom. Additive processes are an evolving field that can integrate complex fibre pathways and multifunctional features [5].

2.4 Key Properties of Composite Materials

Composite materials combine mechanical and functional properties that can be adjusted through the choice of fibre type, matrix system and reinforcement architecture. This tunability gives rise to a set of performance advantages that frequently make composites preferable to conventional engineering materials, such as metals [1].

A primary mechanical benefit of fibre-reinforced composites lies in their high specific stiffness and specific strength. Carbon- and glass-fibre laminates can reach elastic moduli and tensile strengths comparable to, or even greater than, those of aluminium alloys and certain steels, while maintaining substantially lower density. Recent studies on lightweight composite structures emphasise that this balance between low mass and elevated load-carrying capability is one of the main reasons behind the gradual displacement of metallic components in aerospace and transport systems [1]. In this regard, Bukvić et al. [5] note that the increasing demand for weight reduction in engineered systems has accelerated the adoption of polymer-matrix composites in areas traditionally dominated by metals.

Another important distinction between composites and metals is the ability to tailor their anisotropy. Whereas metallic materials generally exhibit isotropic elastic behaviour, fibre-reinforced laminates can be designed to display anisotropic or orthotropic responses. By aligning unidirectional plies or fabric layers along principal stress paths, designers can enhance stiffness and strength where required while reducing material in directions subjected to lower loads [9]. This level of directional optimisation is not feasible with isotropic metallic alloys and is one of the reasons for the increasing interest in composite lay-up strategies for weight-critical structures.

The fatigue behaviour of composites also differs markedly from that of metals: composite laminates tend to accumulate damage through a combination of matrix micro-cracking, fibre-matrix debonding, fibre fracture and interlaminar delamination [2], whereas metals typically fail under cyclic loading through the initiation and propagation of a dominant crack. Hamzat et al. [2] report that the stiffness loss in fibre-dominated laminates is often gradual, allowing the structure to retain a significant portion of its load-bearing capacity for much of its fatigue life, particularly under tension–tension or bending conditions. This behaviour underpins the widespread use of composites in applications such as wind turbine blades and aircraft primary structures, where long-term fatigue resistance is essential.

Beyond mechanical performance, polymer-matrix composites offer resistance to corrosion and chemical degradation, an important advantage in marine, offshore and chemically aggressive environments [8]. Their low density, especially in the case of carbon or aramid reinforcement, further contributes to significant mass savings when compared with aluminium and steel. These reductions translate into improved fuel efficiency and lower emissions in automotive and aerospace sectors [5].

In addition, composites can also be engineered to achieve specific thermal and electrical properties by combining appropriate fibres, matrices and fillers. Many polymer matrices also exhibit intrinsic damping capacity due to their viscoelastic nature, enabling composite structures to attenuate vibrations more effectively than metallic components. This characteristic can be further adjusted through the selection of matrix formulation and reinforcement architecture [5].

Lastly, modern composite manufacturing processes allow the production of complex geometries and integrated components that are difficult to realise through conventional metal production methods [5].

Taken together, the mechanical and functional attributes outlined above explain why fibre-reinforced composites are increasingly selected over metallic alternatives in advanced engineering applications. It remains important, however, to acknowledge their limitations, such as sensitivity to manufacturing defects, challenges in inspection and repair, and recyclability issues associated with thermosetting systems [5].

Chapter 3

Structural Health Monitoring

3.1 General aspects

Structural Health Monitoring (SHM) may be defined as the continuous or periodic observation of a structure through sensor measurements, with the aim of detecting, localizing, and assessing damage in real or near-real time [20].

Any SHM system relies on an appropriate data-collection strategy, in which different types of sensors are selected according to the quantities to be monitored and the nature of the expected damage. Before defining the sensing layout, several practical aspects should be considered [20]: the type and cost of the sensors, the number of sensing points required, the data-acquisition architecture and storage strategy, and the sensitivity of the sensors to long-term environmental effects such as temperature and humidity.

Functionally, SHM can be regarded as an evolution of classical nondestructive testing (NDT) towards an in-situ, real-time monitoring framework. Whereas NDT methods such as ultrasonics, thermography, or radiography are usually applied offline by trained personnel, SHM systems rely on embedded or permanently attached sensors that monitor the structural response during normal operation. Data-acquisition and signal-processing units then extract relevant features and apply pattern-recognition and statistical techniques to translate raw measurements into quantitative information on the structural state [20].

3.2 SHM in Composite Materials

The rapid expansion of composite materials in structural engineering has substantially altered how design, inspection, and integrity assessment are conceived. Despite their considerable advantages, composite materials exhibit complex, multi-scale damage mechanisms, including:

- Delamination between layers, typically caused by impact or out-of-plane stresses;
- Fibre breakage and fibre–matrix debonding, which reduce the load-carrying capacity;
- Matrix microcracking, which can propagate under fatigue loading;

- Barely Visible Impact Damage (BVID), which can significantly compromise the structural integrity despite minimal surface evidence [21].

These damage mechanisms are not easily detected or quantified using conventional nondestructive evaluation (NDE) techniques [22]. Indeed, unlike metallic alloys, composite structures may accumulate internal damage that propagates under cyclic loading while the external surface remains apparently undamaged. As a result, traditional inspection regimes based on scheduled maintenance and local manual inspections are increasingly inadequate for ensuring structural safety, especially in safety-critical components such as aircraft fuselages, rotor blades, and pressurized vessels [21]. In this context, SHM has emerged as a key technology for maintaining the reliability of composite structures over their entire service life.

A central driver for SHM in composites is the shift towards Condition-Based Maintenance (CBM), in which maintenance actions are triggered by the actual condition of the structure rather than by fixed time or usage intervals. This paradigm has the potential to reduce maintenance costs and downtime while improving safety, particularly for high-value assets such as aircraft and wind turbines, where maintenance constitutes a substantial portion of the life-cycle cost [22].

For composite materials, SHM typically involves the integration of sensing and processing capabilities within or on the structure, resulting in “smart” composites capable of self-diagnosis.

Implementing SHM in composite structures nevertheless remains technically challenging. The anisotropic elastic properties of laminated composites make guided-wave propagation strongly direction-dependent, complicating signal interpretation and damage localization. Environmental and operational variations (EOVs), including temperature, humidity, and variable loading, can mask or imitate damage signatures if not properly compensated. Moreover, embedding sensors within the laminate may influence mechanical performance or require adaptations of the manufacturing process [23].

Recent research aims to overcome these limitations by means of: hybrid sensing concepts that combine fiber-optic sensors, piezoelectric transducers, and self-sensing materials; advanced signal-processing schemes; and with the use of machine-learning algorithms for automated damage classification and prognosis. The convergence of these technologies is gradually transforming SHM from a purely diagnostic tool into a predictive framework for the next generation of smart, self-aware composite structures [24].

3.3 Main SHM Techniques for Composite Materials

Several sensing approaches are employed for SHM in composite structures, each exploiting different physical phenomena and offering complementary capabilities. Guided-wave (Lamb-wave) techniques use ultrasonic waves propagating in thin plates or laminates; structural discontinuities such as delaminations or cracks alter wave amplitude, phase and arrival time, so these methods can interrogate large areas while remaining highly sensitive to small defects [25].

Acoustic emission (AE) methods, by contrast, are passive: they record transient elastic waves released by damage events such as matrix cracking or fibre breakage and can often distinguish different damage mechanisms from their frequency content [20].

Global, vibration-based approaches monitor changes in modal properties (natural frequencies, damping, mode shapes) to identify stiffness loss at the structural level, although in composites their sensitivity to very localised defects is limited and environmental variability can obscure damage signatures.

To improve early-damage detectability, nonlinear techniques such as vibro-acoustic modulation (VAM) exploit frequency-mixing effects that arise in the presence of microcracks or interfacial degradation, and are therefore promising for capturing the onset of subtle damage [20].

Finally, recent advances in smart materials enable self-sensing concepts, in which sensors are embedded within the laminate so that the composite itself becomes a sensor network, providing distributed strain and damage information directly from the material [24]. In particular, optical fibre sensors (OFS) have emerged as a versatile and high-performance class of sensors for SHM of civil, aerospace and marine structures. Their deployment for long-term monitoring of strain and temperature is due to the many advantages they present: lightweight, small size, high sensitivity, fully distributed measurement capability (i.e. a longer gauge length delivers more accurate measurements), anti-electromagnetic interference [8], long-term stability and durability and so on, making them especially adapt to the SHM requirements, hence their use has increased over the years [26].

Chapter 4

Optical Fibres

4.1 Optical Fibres Functioning

Optical fibres are thin strands of glass or plastic, consisting of a core, a cladding, and a protective coating, as shown in Figure 4.1. They transmit light by exploiting the principle of total internal reflection: light propagates along the core and, when it reaches the core–cladding interface at an angle larger than the critical angle θ_c, it is reflected back into the core because the cladding has a slightly lower refractive index than the core. In this way, light is confined within the core and can be guided over long distances with limited attenuation [27, 28].

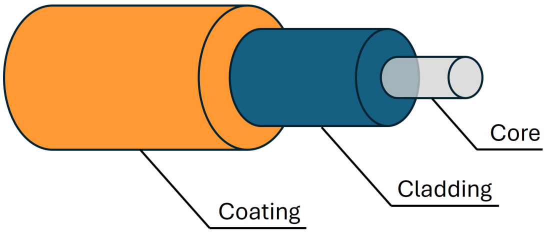

Figure 4.1: Scheme of Optical Fibre.

The refractive index n of a material is defined as

$$n = \frac{c_0}{v} \tag{4.1}$$

where c_0 is the speed of light in vacuum and v is the phase velocity of light in the material. A higher refractive index therefore corresponds to a lower light velocity in the medium. In the case of an optical fibre, the core is typically made of silica glass, whose refractive index is significantly higher than that of air. This means that light travels more slowly in the glass core than in air, and, combined with a slightly lower refractive index in the cladding, this contrast allows the fibre to guide light efficiently by total internal reflection over long distances [29].

A standard step-index fibre can be modelled by assuming that the refractive index is constant in the core and in the cladding. If we denote the core radius by a, the core refractive index by n_1, and the cladding refractive index by n_2, with $n_1 > n_2$, then the refractive index profile is:

$$n(r) = \begin{cases} n_1, & r \leq a \\ n_2, & r > a \end{cases}$$

The critical angle θ_c at the core–cladding interface follows from Snell's law and is given by:

$$\theta_c = \arcsin\left(\frac{n_2}{n_1}\right) \tag{4.2}$$

The light, in order to be admitted by the fibre and to be guided along it, has to enter within a specific range of input angles. This defines the acceptance cone of the fibre, depending on the difference between the refractive indexes of the core and cladding. The numerical aperture (NA) quantifies the range of angles over which the fibre can accept incoming light: it follows that a higher NA corresponds to a wider acceptance cone, allowing the fibre to capture light from a broader range of directions [27, 29]. For a step-index fibre, the numerical aperture NA is expressed as:

$$\mathrm{NA} = \sqrt{n_1^2 - n_2^2} \tag{4.3}$$

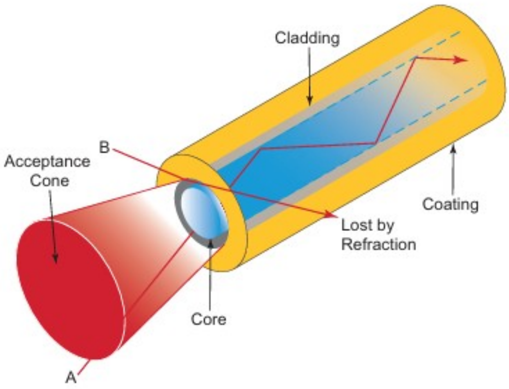

Figure 4.2: Acceptance cone and scheme of optical fibre [28].

Optical fibres can be treated as cylindrical dielectric waveguides. Hence, in order to obtain a rigorous description of light propagation, electromagnetic wave theory has to be taken into account, based on the Maxwell's equations. In the absence of free charges and currents, and for a linear, isotropic, dielectric medium, the time-harmonic Maxwell equations can be written as:

$$\nabla \times \mathbf{E} = -j\omega\mu\mathbf{H} \tag{4.4}$$

$$\nabla \times \mathbf{H} = j\omega\varepsilon\mathbf{E} \tag{4.5}$$

Where E and H are the electric and magnetic field vectors respectively, ω is the angular frequency, μ is the magnetic permeability, and $\varepsilon = n^2\varepsilon_0$ is the permittivity of the medium, with n being the refractive index.
Combining these curl equations leads to the vector Helmholtz equations:

$$\nabla^2\mathbf{E} + k^2n^2\mathbf{E} = 0 \tag{4.6}$$

$$\nabla^2\mathbf{H} + k^2n^2\mathbf{H} = 0 \tag{4.7}$$

where $k = \dfrac{2\pi}{\lambda_0}$ is the free-space wavenumber and λ_0 is the wavelength in vacuum [30].

Using cylindrical coordinates (r, ϕ, z), the electric field can be expressed as a mode function:

$$\mathbf{E}(r, \phi, z) = \mathbf{E}(r, \phi)\, e^{-j\beta z}.$$

where β is the propagation constant, which determines the phase evolution of the guided mode along the fibre axis [30].

Substituting this form into the Helmholtz equation and making the scalar approximation leads to the scalar wave equation in cylindrical coordinates:

$$\frac{1}{r}\frac{\partial}{\partial r}\left(r\frac{\partial E}{\partial r}\right) + \frac{1}{r^2}\frac{\partial^2 E}{\partial \phi^2} + \left(k^2n^2 - \beta^2\right)E = 0 \tag{4.8}$$

This equation describes how each mode is distributed in the transverse plane and how it propagates along the fibre.

4.2 Modes of Optical Fibres

Depending on the number of guided modes they support, optical fibres are classified as single-mode or multimode. Single-mode fibres support only the fundamental mode, usually denoted LP_{01}, for each polarization direction at a given wavelength [27]. Multimode fibres, in contrast, guide several transverse modes simultaneously.
This difference is reflected in both core size and typical applications:

- Single-mode fibres have a small core diameter, typically around 9 µm, and are used for long-distance communication because they minimise modal dispersion.
- Multimode fibres have larger cores, typically 50–62.5 µm, and are suitable for short distance applications such as local area networks (LANs) [27].

A key dimensionless parameter in fibre optics is the normalized frequency, or V-number [31]

$$V = \frac{2\pi a}{\lambda}\sqrt{n_1^2 - n_2^2} = \frac{2\pi a}{\lambda}\,\mathrm{NA}$$

The number of guided modes M in a step-index fibre can be approximated as:

$$M \approx \frac{V^2}{2}$$

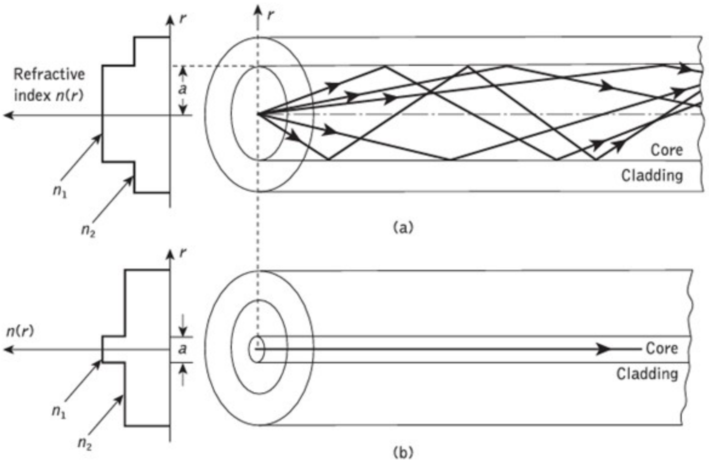

Figure 4.3: Refractive index profile in: (a) multimode step-index fibre; (b) single-mode step-index fibre [27].

For single-mode operation, only the fundamental mode LP_{01} is supported, which occurs when:

$$V < 2.405$$

4.3 Types of Optical Fibres

In the context of optical-fibre sensing, an important distinction concerns the spatial distribution of the sensing capability along the fibre. Optical fibre sensors are commonly categorised as [32]:

- Point Sensors
- Quasi-distributed Sensors
- Distributed Sensors (DFOS)

4.3.1 Point Sensors

Point sensors represent the most basic configuration: one, or a small number, of discrete sensing elements is interrogated to provide measurements at specific locations. A typical example is a single fibre Bragg grating (FBG) sensor. Point sensors offer high sensitivity and rely on well-established interrogation technologies. However, their spatial coverage is inherently limited, which means that damage occurring away from the sensor locations may go undetected.

4.3.2 Quasi-distributed Sensors

In this case, coverage is more extensive than a few discrete points, but still not truly continuous. They expand on the point model by multiplexing several discrete sensors along one fibre. Typically, a single fibre hosts a number of FBGs or sensing nodes spaced apart [32].

4.3.3 Distributed Sensors

They represent the highest level of spatial coverage: essentially every point (or a very fine grid of points) along the fibre is a sensing location. This is achieved by exploiting scattering phenomena in optical fibres and by interrogating the time, phase, wavelength or amplitude of the back-scattered light as a function of distance, it is possible to measure local physical quantities, such as temperature and strain, continuously along the fibre; this capability makes DOFS particularly attractive for structural health monitoring of large or complex structures, including composite materials [33]. The three main mechanisms of scattering in optical fibres used for DFOS are Rayleigh, Brillouin and Raman.

4.4 Fiber Bragg grating (FBG) sensors

Fiber Bragg grating (FBG) sensors are optical fibre sensors in which the sensing element is built directly inside the core of a standard single-mode fibre. An FBG is a short section of fibre where the core refractive index is made to vary periodically along the fibre axis. This periodic pattern acts as a narrowband mirror (a Bragg reflector): it strongly reflects a specific wavelength, called the Bragg wavelength, while allowing all the other wavelengths to pass through [34].

The behaviour of an FBG is described by the Bragg condition. For a uniform grating with period Λ written in a fibre with effective refractive index n_{eff}, the Bragg wavelength λ_B is given by:

$$\lambda_B = 2\, n_{\text{eff}}\, \Lambda$$

This means that only light with wavelength λ_B is efficiently reflected by the grating; light at other wavelengths is mostly transmitted. Both n_{eff} and Λ change when the fibre is stretched or when its temperature changes: as a result, λ_B shifts if the fibre is under strain or subjected to a temperature variation. In many practical cases, this shift can be written in a simple linear form:

$$\Delta\lambda_B = k_\varepsilon\, \varepsilon + k_T\, \Delta T$$

where ε is the axial strain, ΔT is the temperature change, and k_ε and k_T are calibration constants determined experimentally for that particular sensor [34].

FBGs are usually written in photosensitive silica single-mode fibres by exposing the core to an ultraviolet interference pattern. This process creates a permanent and well-controlled index modulation. The resulting gratings are compatible with standard telecommunication fibres and hardware, so they can be spliced and routed using conventional fibre-optic technology [27]. By choosing different grating periods (and therefore different Bragg wavelengths), many FBGs can be inscribed along the same fibre. Each grating reflects a different wavelength, so a single interrogation unit can read multiple sensing points along one fibre, forming a quasi-distributed sensor array [34, 35].

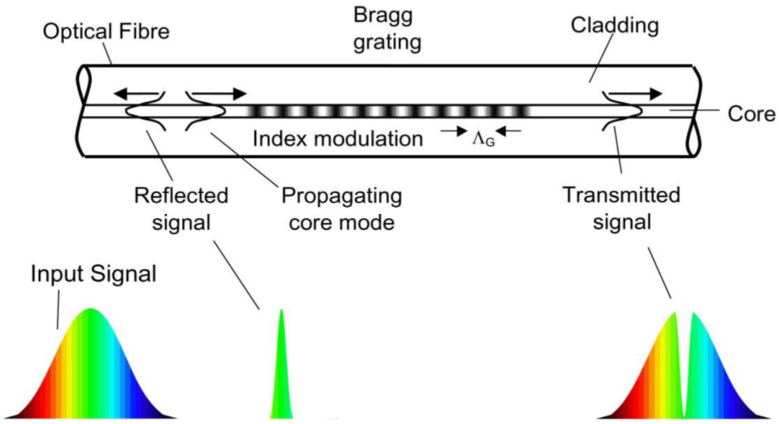

Figure 4.4: Schematic diagram of an FBG functioning [36]

Because they are small, lightweight and multiplexable, FBG sensors are widely used for SHM of composite structures. They can be bonded on the surface or embedded between plies during manufacturing to measure local strain, follow global deformation and detect damage such as delamination or impact-induced defects [20, 35].

FBG technology offers several important advantages. The quantity to be measured is converted into a wavelength shift rather than a change in optical power, thus the measurement is less sensitive to fluctuations of the light source and to losses along the fibre. The fibre and the grating are entirely dielectric, which makes the sensor immune to electromagnetic interference and suitable for harsh or high-voltage environments. Moreover, the very small diameter of the fibre also allows the sensors to be embedded with minimal impact on the host structure [27, 35]. On the other hand, FBGs require interrogation units capable of resolving wavelength, which are more complex and expensive than simple intensity-based systems, especially when many sensors or high sampling rates are needed. In addition, both strain and temperature shift the Bragg wavelength, so compensation techniques are needed to separate these effects. Lastly, when FBGs are embedded in composites, further uncertainties may arise from how well strain is transferred from the material to the fibre and from residual stresses after curing [20, 35].

4.5 DFOS - Scattering Methods

4.5.1 Brillouin Scattering

Brillouin scattering is an inelastic interaction between the incident light wave and the thermally generated acoustic waves (acoustic phonons) in the fibre core. In this light–sound interaction, part of the optical energy is transferred to the acoustic wave, giving rise to a backscattered Stokes component (and sometimes an anti-Stokes component) whose frequency is shifted by about 10–11 GHz for light at around 1,530–1,550 nm in standard silica fibre. This Brillouin frequency shift (BFS) depends on both strain and temperature, because changes in these quantities modify the acoustic velocity and the refractive index of the fibre. As a result, Brillouin-based distributed sensors can be used to obtain fully distributed measurements of strain and temperature along the fibre. Thanks to its capability of performing measurements over a very extended range (up to several kilometres), it is particularly well suited for applications in the civil engineering sector [33].

4.5.2 Raman Scattering

Raman scattering is also an inelastic process, but it involves the interaction between photons and molecular vibrations (optical phonons) in the glass. The scattered light exhibits a relatively large frequency shift, of the order of 13 THz at 1,550 nm, between the pump and the Stokes/anti-Stokes components. In Raman-based distributed sensing, the intensity of the anti-Stokes component is strongly temperature-dependent and only weakly affected by strain, which makes Raman scattering particularly suitable for distributed temperature measurements over long distances [33].

4.5.3 Rayleigh Scattering

Rayleigh scattering, by contrast, is an elastic process. A coherent optical field launched into a single-mode fibre is scattered by microscopic fluctuations of the refractive index (for example, density fluctuations or material inhomogeneities), but the scattered light retains essentially the same optical frequency as the incident light. The fibre can therefore be regarded as a continuum of randomly distributed scattering centres that reflect a small fraction of the guided light back towards the source [33, 37].

In Rayleigh-based distributed optical fibre sensing, this backscattered signal is interrogated using techniques such as optical time-domain reflectometry (OTDR) and optical frequency-domain reflectometry (OFDR). In OTDR, short optical pulses are injected into the fibre and the intensity of the backscattered light is recorded as a function of time; the time of flight is then converted into distance using the known group velocity, providing a spatially resolved trace along the fibre. Phase-sensitive OTDR (ϕ-OTDR) extends this concept by using coherent detection, so that changes in the optical phase of the backscattered signal can be monitored, enabling dynamic and vibration sensing with metre-scale spatial resolution [33, 37].

OFDR adopts a different approach. Instead of time-of-flight measurements, a narrow-linewidth laser is swept in frequency and the interference between the backscattered light and a reference arm is analysed in the frequency domain. A Fourier transform then maps the frequency content into position, yielding a high-resolution profile of the backscatter along the fibre. Coherent OFDR can achieve spatial resolutions in the millimetre–centimetre range over lengths of up to several tens of metres, at the expense of a more limited sensing range and stricter requirements on laser stability and environmental control. Commercial instruments based on this principle are often referred to as optical backscatter reflectometers (OBR) and are widely used in laboratory [33, 37], including in the experimental campaign carried out in this work.

In all the aforementioned techniques, the sensing mechanism does not rely on the Rayleigh cross-section being directly sensitive to strain or temperature. Instead, local perturbations (strain, temperature variations, vibration) modify the propagation conditions of the guided light, leading to changes in phase, attenuation, polarization state or interference of the backscattered field [33, 37]. Therefore, a reference, or “baseline”, backscatter profile is first acquired under known conditions. Subsequent measurements are compared to this reference; local changes in signal content indicate a change in the local optical path length, which can be related to variations in strain or temperature. Because each small fibre segment contributes a distinct backscattering signature, Rayleigh-based systems can provide a continuous or quasi-continuous profile of the measurand along the fibre [33, 37].

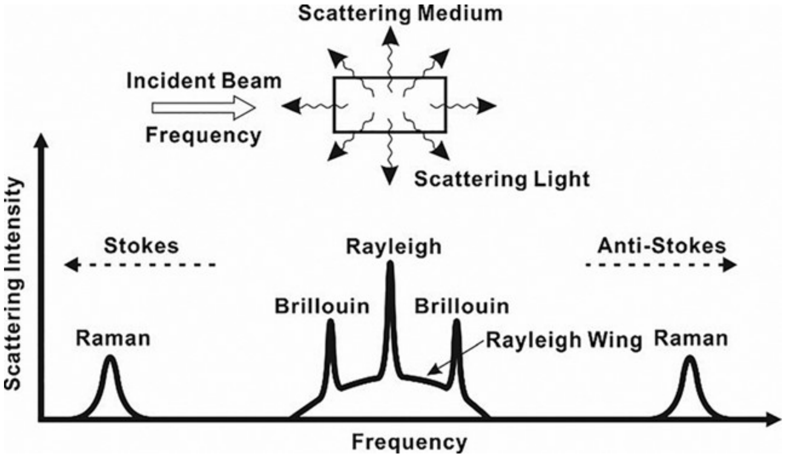

Figure 4.5: A typical light scattering spectrum with different scattering mechanisms [33].

Rayleigh DFOS present many advantages:

- High spatial resolution for localised damage detection: depending on the interrogation scheme, spatial resolutions in the millimetre–centimetre range can be achieved; this makes embedded or surface-bonded Rayleigh-based sensors well suited to detecting highly localised damage, such as crack initiation, delamination or fibre–matrix debonding in structural materials [33, 37].

- Capability for dynamic and vibration sensing: the relatively strong Rayleigh backscattered signal allows for high measurement rates, therefore systems based on phase-sensitive Rayleigh OTDR (ϕ-OTDR) or coherent OFDR can measure vibration or acoustic events, making them suitable for impact/damage-detection scenarios in composites [33, 37].

- Good signal-to-noise ratio and mature instrumentation: compared with inelastic Brillouin- and Raman-based methods, elastic Rayleigh scattering generally yields a stronger backscattered signal, enabling shorter integration times or fewer averages. This facilitates real-time or frequent monitoring in practical applications, supported by a growing range of commercial interrogators [33, 37].

A comparative summary of the different scattering type mechanisms is shown in Table 4.1.

Table 4.1: Comparison of Rayleigh, Brillouin, and Raman scattering mechanisms in distributed optical fiber sensing.

	Rayleigh	**Brillouin**	**Raman**
Sensitive to	Strain, temperature, vibration	Strain, temperature	Temperature only
Spatial resolution	mm to cm	metre-scale	0.5 m to metres
Main strength	High resolution, good SNR, suitable for dynamic/vibration	Long length coverage, absolute measurand	Temperature mapping over long distances
Main limitation	Full absolute measurement often requires calibration; shorter range; embedding/strain-transfer issues	Lower resolution, slower response, cross-sensitivity	No strain sensing; coarse resolution

4.6 Challenges of Using Rayleigh-Based DFOS in Composite Materials

When Rayleigh-based distributed fibre-optic sensing is incorporated into composite structures, several technical considerations must be addressed to ensure that the measured strain fields accurately reflect the mechanical response of the host laminate throughout its service life.

4.6.1 Strain Transfer

A fundamental requirement for the reliability of Rayleigh DFOS is the ability to transfer strain efficiently from the composite substrate to the fibre core. However, many aspects lead to potential difficulties.

For surface-bonded configurations, any degree of slip or partial debonding at the interfaces between the laminate surface, the adhesive layer and the fibre coating can distort the strain distribution reconstructed from the Rayleigh backscatter signal. Furthermore, experimental studies on bonded distributed sensors have demonstrated that adhesive stiffness and thickness, and the quality of the bonding process significantly influence strain-transfer efficiency and may introduce systematic measurement offsets if not properly controlled [38].

On the other hand, embedding fibres directly within the laminate avoids some of the limitations of surface bonding but introduces additional complexity. When a fibre is placed between plies or in resin-rich regions, its geometric presence, together with its coating, locally perturbs the stiffness field of the laminate. This disturbance may promote the formation of resin pockets, i.e., localised resin-rich zones generated around the fibre during lay-up and consolidation. These resin pockets may act as preferential sites for micro-void formation, fibre–matrix debonding and even delamination onset during curing or under cyclic loading conditions. As highlighted by Drissi-Habti and Raman [39], these resin-rich pockets can progressively evolve under fatigue through matrix cracking, interfacial degradation or local stiffness reductions, ultimately modifying the mechanical interaction between the host laminate and the embedded optical fibre.

Such degradation mechanisms influence the optical response in two ways. First, if the fibre becomes partially debonded or mechanically shielded by surrounding resin pockets, the strain transferred to the core may no longer represent the laminate deformation faithfully. Second, as cyclic loading accumulates, the surrounding composite may undergo progressive non-linear changes, such as micro-damage, residual-stress redistribution and local compliance variations, which can induce long-term drift or fluctuations in the Rayleigh spectral signature [39].

Maintaining accurate strain transfer throughout the structure's operational life therefore requires that the adhesive or embedding matrix remain mechanically stable under thermal excursions, moisture ingress and long-term fatigue loading. Phenomena, such as creep in the adhesive, environmental degradation of the coating, or post-cure relaxation of the composite, can gradually compromise strain-transfer integrity, resulting in measurements dominated by the behaviour of the bonding material or the optical fibre itself

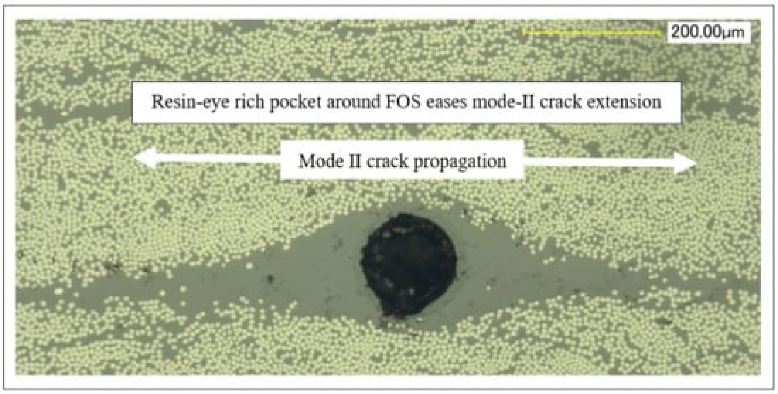

Figure 4.6: Resin-eye rich concentration around FOS [39].

rather than the true mechanical state of the laminate. For these reasons, an accurate selection of adhesive systems, embedding methodologies, laminate lay-up strategies and quality-assurance procedures remain essential when integrating Rayleigh-based DFOS into composite structures.

4.6.2 Embedment of Optical Fibres

The incorporation of optical fibres within laminated composite structures exposes the sensing element to several mechanical and thermal hazards throughout the manufacturing cycle. These challenges are particularly pronounced during resin infusion, consolidation under vacuum, and thermal cure, when the laminate undergoes large pressure gradients, resin flow forces and thermally driven dimensional changes.

First of all, during infusion-based processes, the advancing resin can impose local drag forces on the optical fibre. If the fibre is not properly stabilised within the preform, these forces may cause unintended displacement, excessive local bending or even fibre breakage [40].

Additional risks arise during consolidation and thermal cure. In fact, during autoclave cure or vacuum bagging, compaction forces may pinch or crush fibres at ply interfaces. Gabardi et al. [41] experimentally observed that breakage is especially likely in curved components, especially when the optical cable was poorly supported and subjected to bending during consolidation.

The most critical failure zones, however, are the entry/exit regions where the fibre transitions from inside the laminate to the outside environment. In fact, these locations act as geometric stress concentrators and are frequently exposed to handling, accidental bending and trimming forces after cure [42]. A detailed study by Quest Global Services [42] found that the fibre segment exiting the laminate was structurally very weak and highly susceptible to fracture due to:

- local stress concentrations at the laminate edge
- resin flashing surrounding the fibre: during infusion (or also prepreg curing), excess

resin can flow out of the laminate edges and solidify (i.e. taking the name of flash or flashing). If the optical fibre runs through the laminate and exits at the edge, this excess resin can solidify around the fibre, essentially clamping it tightly. When removing the cured composite part from the mould, if the fibre has been trapped inside this hardened resin flash, the cutting or peeling action pulls on the fibre, often leading to fibre breakage at or near the exit point, debonding or strain-relief failure, damage to the coating, or loss of optical continuity

- tensile/bending loads during trimming or clean-up
- insufficient mechanical protection around the exit region

A range of engineering solutions has been proposed to protect optical fibres during manufacture and ensure reliable embedding in both prepreg and infusion-based processes.

To mitigate these issues, Quest Global Services [42] employed a protection strategy centred on locally reinforcing the fibre near the exit zone. The optical fibre was encapsulated in polyolefin heat-shrink tubing to increase its bending stiffness and to shield it from mechanical abrasion during processing. Colour-coding was applied to the tubes to simplify sensor identification during lay-up and inspection. In addition to the primary heat-shrink layer, supplementary protective tubes were installed around the egress region to further isolate the fibre from tooling interactions and cutting operations. These tubes were sealed to prevent resin ingress, which could otherwise lock the fibre into the curing matrix and increase the likelihood of breakage. In some cases, the protected fibre segment was placed inside a small plastic containment bag during cure, ensuring that the egress assembly remained separated from resin flow, compaction forces and local thermal gradients. According to the authors, this combination of mechanical shielding and isolation substantially reduced fibre failures and improved overall reliability of the embedded sensing system [42].

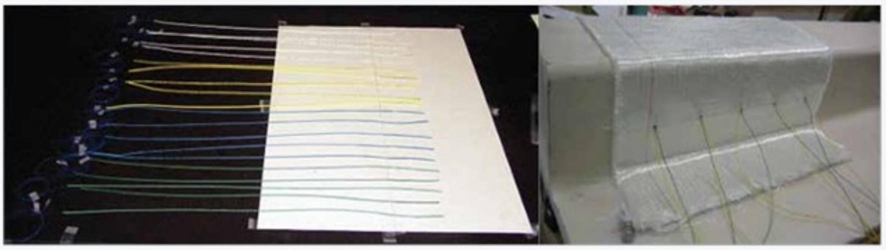

Figure 4.7: Optical Fibre Preparation and Positioning [42].

Moreover, several studies report the use of strain-relief loops (i.e. gentle fibre coils that prevent sharp bending at ingress/egress), and customized connectors embedded at the laminate boundary to avoid direct stress on the bare fibre [41]. These measures reduce tension and bending during manufacturing and service.

Reliable embedding also depends heavily on appropriate fibre routing. Nosseir et al. [43] recommend avoiding tight radii (<20–30 mm), positioning fibres along neutral-strain paths when possible, and ensuring stable fixation inside the preform to prevent

Figure 4.8: Material with Optical Fibres ready for infusion [42].

displacement by resin drag.

Zainal Abidin [40] emphasises that poor routing can introduce micro-defects and local stress concentrations even before cure begins.

Likewise, another technique is the free-spacing coupling, that places the sensing fibre not directly bonded to the composite but placed inside a protective capillary or loose sleeve. This configuration shields the fibre from mechanical loads during infusion and cure, while still allowing strain transfer through frictional or partial contact. Although widely used in concrete SHM systems, it is increasingly explored for composite structures as a strategy to reduce cure-induced fibre damage [33].

Latterly, a solution can be that of adopting prepreg materials: compared with liquid-infusion processes, embedding fibres in prepreg laminates is significantly more controlled because the tacky resin holds the fibre in place, preventing displacement, the consolidation is more predictable, and finally no resin-flow forces act on the fibre, reducing the likelihood of buckling or breakage [41]. Prepreg also allows controlled ply-by-ply placement, enabling precise fibre routing and the creation of designed channels or protective layers around the optical fibre.

Although such manual integration remains the standard, efforts toward automation are beginning to emerge, even if these approaches are still in early development. In particular experimental systems have demonstrated the feasibility of embedding sensing fibres using robotic fibre-optic placement heads mounted on Automated Fibre Placement (AFP) robots, as well as the automated deposition of micro-tubing during AFP that can later serve as conduits for optical fibres [44].

4.6.3 Temperature-Strain Coupling

Composite structures operating in real service environments are subjected to continuous fluctuations in temperature, humidity and mechanical loads. These environmental variations directly influence the behaviour of Rayleigh-based distributed fibre-optic sensors because the Rayleigh backscatter signature inherently couples strain and temperature.

Specifically, both mechanical deformation of the glass core and temperature induced changes in refractive index or fibre length produce nearly indistinguishable spectral shifts. As a result, temperature variations can mask, distort, or even simulate true structural strain unless effective discrimination strategies are implemented. This dual sensitivity represents one of the primary challenges in interpreting DFOS data from composite structures [33].

Several approaches have been proposed to decouple strain and temperature contributions. One class of techniques relies on multi-region or multi-parameter calibration, where the spectral response is characterised under independent strain and temperature fields to derive correction functions. Another approach, particularly relevant for composite structures, involves using reference fibres that experience similar temperature fields but negligible mechanical strain; by subtracting the reference response, it is possible to isolate the true mechanical strain component. More advanced strategies exploit the wavelength-dependence of Rayleigh spectral shifts, or combine Rayleigh DFOS with Bragg-grating sensors or embedded thermocouples to provide complementary measurements, thereby enabling more robust separation of thermal and mechanical effects [33]. Each method must be adapted carefully to account for local composite anisotropy and heterogeneous thermal gradients.

In addition to spectral coupling, there is a thermal expansion mismatch between the silica fibre, its polymeric coating, the adhesive layer and the surrounding composite laminate that introduces further complexity. In fact, differences in coefficients of thermal expansion (CTE) cause differential strains during temperature changes; therefore, even a perfectly bonded fibre may experience an apparent strain that does not correspond to the laminate's mechanical state. Reviews on distributed fibre-optic sensing emphasise that viscoelastic relaxation in polymer matrices, adhesive creep and coating ageing can progressively alter the strain-transfer function, especially under cyclic or long-term temperature exposure [33]. These effects accumulate over the service life, meaning that the calibration obtained during installation may not remain valid indefinitely.

The problem becomes even more prominent when fibres are embedded within composite laminates, where temperature-dependent resin shrinkage, micro-cracking, or stiffness degradation, due to fatigue around the fibre, can alter the optical response over time. Such interactions highlight the need for periodic reassessment of baselines or the adoption of compensation algorithms capable of adapting to evolving material states.

Ultimately, achieving reliable Rayleigh-based distributed sensing in composite structures exposed to environmental and operational variability, requires a combination of robust temperature–strain discrimination techniques, careful sensor placement, stable bonding or embedding procedures, and long-term calibration strategies that take into account the evolving mechanical and thermal behaviour of the laminate.

4.6.4 Durability and Reliability

Applications in offshore, aerospace and wind-energy environments demand sensing systems capable of reliable operation over decades; however, Rayleigh-based DFOS are particularly sensitive to long-term degradation phenomena such as coating ageing, micro-bending and fibre breakage. The stability of the reference spectral fingerprint is crucial: even small micro-movements or ageing processes within the laminate can produce gradual baseline drift, complicating the interpretation of strain maps. Reviews and targeted studies underscore that damage mechanisms such as delamination, impact events or fibre breakage can affect the mechanical interaction between the sensing fibre and the host laminate, altering the strain–optical transfer relationship and making long-term calibration an ongoing requirement [33, 39, 45].

Understanding how the sensing fibre interacts with the evolving damage state of composite laminates is therefore essential for correct interpretation of distributed strain fields, particularly during progressive fatigue or post-impact scenarios.

4.6.5 Data Interpretation

Rayleigh DFOS offer exceptionally high-resolution spatial strain mapping, enabling the detection of minute structural changes long before they become apparent through conventional sensing methods. This capability is particularly valuable for composite structures, where damage often initiates at the microscale and progresses in complex, spatially distributed patterns. However, the same high resolution that makes Rayleigh DFOS attractive also introduces substantial challenges in data handling and interpretation. The technique produces very large datasets, often comprising millions of measurement points per scan, each sensitive to environmental variability and operational noise.

Interpreting such dense information requires advanced processing strategies capable of isolating physically meaningful features from background fluctuations. Robust filtering algorithms are essential to suppress spectral noise and temperature-induced variations, while pattern-recognition and anomaly-detection methods must be employed to identify the early signatures of delamination, matrix cracking, fibre breakage or local stiffness degradation. These early-stage indicators are often subtle (e.g. appearing as localised strain concentrations, shifts in deformation patterns, or changes in strain-gradient continuity) and are easily obscured without sophisticated analytical tools.

Industrial assessments further highlight that cost–benefit considerations remain a major barrier to widespread adoption of Rayleigh-based DFOS outside many sectors. Although high resolution distributed sensing offers rich data, the infrastructure cost, sensor installation, interrogator expense and data analytics must be justified in lifecycle terms, especially in composite components outside aerospace [45].

4.7 Fibre Coatings

The mechanical coupling between the host structure and the fibre is strongly influenced by the fibre construction and, in particular by the coating applied to the glass core. Different coatings trade off mechanical protection, maximum operating temperature, strain-transfer fidelity, robustness during manufacturing/handling and longevity when embedded in composites. The most commonly used types in Rayleigh DFOS deployments are acrylate-coated fibres, polyimide-coated fibres, bare or tight-buffered fibres, and metal-coated/specialty fibres [46]. The present work focuses on the first two types.

4.7.1 Acrylate Coating

Acrylate coatings (single or dual layer) are the standard protection applied to telecom single-mode fibres: a relatively soft polymer layer (typical outer diameter ≈ 250 μm with primary coating ≈125–245 μm) that protects the glass from handling damage and microbending [46].

They present different advantages: excellent flexibility and ease of handling, low cost and wide availability; they offer compatibility with commercial OFDR interrogators for standard single-mode fibre [46–48], and a good strain transfer when the surface is bonded with proper adhesive and sufficient bonded length [49].

However, this type of fibre presents also several drawbacks, such as low maximum temperature: acrylate softens or degrades above ≈ 80–150 °C (dependent on formulation), making acrylate fibres poorly suited for high-temperature cure cycles or high-temperature service without special precautions [46]. This limits their use for some composite manufacturing processes (e.g. high-temperature cure) [46, 48]. Moreover, the relatively compliant coating and any adhesive layer introduce viscoelastic creep, which reduce strain-transfer fidelity over short gauge lengths and long durations; in practice the measured strain on acrylate fibres can be lower and slower to follow the host strain under dynamic loading compared to stiffer coatings [49]. Lastly, regarding their durability when embedded: softer coatings can be damaged during composite consolidation or become a preferential path for micro-voids if not carefully routed and protected [48].

These characteristics make acrylate-coated fibres appropriate for surface bonding, short-term tests, laboratory demonstrators, or composite parts cured at low temperatures. They are economical for quasi-permanent installations where high-temperature exposure is not expected [46, 48].

4.7.2 Polyimide Coating

Polyimide is a thin, high-temperature polymer coating applied directly to the glass (typical coated diameter ≈ 155–190 μm). Among the many advantages, it can be included:

- High temperature capability: polyimide retains mechanical integrity at elevated cure and service temperatures, enabling embedding in high-temperature cured composites or use in hot environments [46, 47];
- Thin, stiffer coating: the thin polyimide layer provides closer mechanical coupling to the glass and generally improves strain-transfer fidelity (less shear-lag than thick acrylate), which is beneficial for accurate localized strain mapping using Rayleigh OFDR [47, 49];
- Smaller overall diameter: it eases embedding between plies without creating thick inclusions and reduces any risk of local ply distortion [47].

Nevertheless, it is difficult to overlook several drawbacks:

- Brittleness and handling fragility: polyimide coatings are thinner, therefore the fibre can be more easily scratched during handling and must be treated carefully in manufacturing operations. This increases the risk of breakage at routing bends or pinch points [48];

- Adhesion issues on some surfaces and processing constraints: some polyimide formulations can adhere strongly to metal tooling or mandrels during high-temperature exposure, so special process controls are sometimes required [46];
- Higher cost: polyimide-coated sensing fibres (especially low-bend loss fibres for Rayleigh systems) are more expensive than standard acrylate telecom fibre [47].

For these reasons, polyimide-coated fibre is the preferred option for embedded Rayleigh DFOS in load-bearing composite laminates that undergo elevated-temperature cure or operate in harsh thermal environments, or where high strain-transfer fidelity is required (e.g., mm-scale localization) [46, 47].

From a design point of view, the choice of fibre coating type therefore represents a practical trade-off among different requirements:

- If high spatial resolution and embedded sensing during high-temperature cure are required, polyimide-coated single-mode fibre is preferred as it offers the best strain fidelity and thermal tolerance, provided that careful handling and validated embedding procedures are used [46, 47].
- If low cost and surface-bonded experiments are the main objectives, acrylate-coated fibre is generally sufficient (cheap and flexible), but elevated cure or service temperatures should be avoided [46].

4.7.3 Hybrid Fibre

Experimental investigations have compared the fibres in acrylate coating and polyimide coating in both embedded and surface-bonded configurations, highlighting how the coating properties influence strain-transfer efficiency and the spatial uniformity of the measured signal [50, 51].

In particular, it has been demonstrated that polyimide-coated optical fibres provide superior strain-transfer performance when embedded in composite materials, independently of the fibre length employed. The thin and stiff polyimide layer enables efficient mechanical coupling between the glass core and the surrounding matrix, thus ensuring that the measured strain closely reflects the actual deformation of the host composite [50, 51]. Conversely, acrylate-coated fibres, which feature a thicker and more compliant coating, tend to absorb part of the imposed deformation. As a result, only longer bonded or embedded lengths of acrylate fibre can reproduce the effective mechanical strain with acceptable accuracy [37, 50].

These measurements have been validated against conventional strain-measurement techniques such as strain gauges and digital image correlation (DIC), confirming the reliability of Rayleigh-based distributed sensing in reproducing the global and local strain fields of composite laminates [50]. Such results demonstrate that the accuracy of Rayleigh

DFOS is primarily governed by the coating–matrix interaction, the bonding method, and the fibre installation process.

Particular attention has been devoted to the evaluation of the elastic modulus under semi-static tensile loading. Unlike metallic materials, composites typically exhibit a progressive reduction of the elastic modulus already in the early stages of damage initiation, due to matrix cracking, fibre–matrix debonding, or interlaminar delamination, well before catastrophic failure occurs [21]. For this reason, Rayleigh-based DFOS systems, which provide high spatial resolution (on the order of millimetres), are especially suitable for detecting stiffness degradation and for quantifying the onset and evolution of micro-damage in real time [37, 50, 51]. These studies confirm that polyimide-coated fibres outperform acrylate-coated ones in capturing the local strain distribution and the effective elastic modulus of composite coupons, thus providing a more faithful assessment of structural integrity.

Based on these findings, a hybrid optical fibre design has been proposed to exploit the advantages of both coatings. The configuration consists of sequential segments arranged as: acrylate-coated section – polyimide-coated section – acrylate-coated section, as shown in Figure 4.9. The central polyimide-coated region and its junctions with the acrylate sections are intended to be embedded within the composite laminate, whereas the outer acrylate-coated parts remain external to the material to improve handling robustness and installation flexibility. This hybrid layout preserves the high strain-sensing accuracy of the polyimide section, while maintaining the mechanical resilience and ease of manipulation of the acrylate-coated segments [51].

In summary, the combined results from these studies highlight that, for Rayleigh-based DFOS applied to composites, the coating selection represents a critical design parameter affecting strain-transfer fidelity, measurement repeatability, and long-term reliability. The hybrid-fibre concept provides a promising solution that balances measurement precision, manufacturability, and robustness for next-generation composite SHM systems.

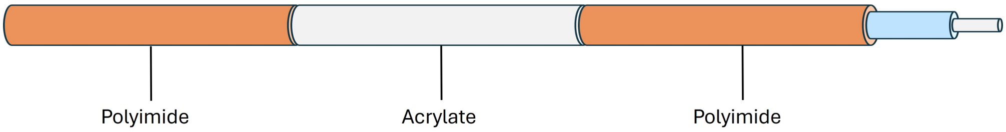

Figure 4.9: Hybrid Fibre Scheme.

Chapter 5

Specimen Preparation and Experimental Setup

5.1 Preparation of fibres

5.1.1 Types of fibres

In the context of the present work, the following fibres have been employed both individually and in combination for the development of the hybrid configuration:

1. Single-mode G.657.A1 fibre of Optokon with a dual acrylate UV-cured coating

2. SM1550P fibre of Thorlabs with a polyimide coating

The characteristics of the two fibres are shown in Table 5.1.

Table 5.1: Optical Fibres General Specifications.

General Specifications	**G.657.A1 - Optokon**	**SM1550P - Thorlabs**
Core Material	Germanium doped silica	Doped Fused Silica
Cladding Material	Silica, step index and matched clad type	Fused Silica
Coating Material	Dual layers of UV-cured acrylate	Polyimide
Core Diameter	Not Provided	9.0 ± 0.5 μm
Cladding Diameter	125.0 ± 0.7 μm	125 + 1/-3 μm
Coating Diameter	242 ± 5 μm	145 ± 5 μm
Mode Field Diameter at 1310 nm	8.9 ± 0.4 μm	9.0 μm
Effective group index of refraction at 1550 nm	1.468	Not Provided
Attenuation	$\leq$0.40 dB/km	$\leq$0.7 dB/km
Operating Temperature	-55 to 85°C	-65 to 250°C

5.1.2 Fusion Splicer

In order to employ the optical fibres for sensing, either individually or in combination within the hybrid fibre, splicing represents a fundamental step. To this aim, the terminal portions of the optical fibre was carefully prepared to ensure clean and reliable splicing. Approximately 2 cm of coating were removed from each fibre end using a precision mechanical stripper, exposing the bare glass core. The stripped sections were then cleaned with isopropyl alcohol and lint-free wipes to remove coating residues and contaminants that could interfere with the fusion process [52].

The cleaned fibre ends were subsequently cleaved using a Fujikura CT60 high-precision optical fibre cleaver, which produces a smooth, perpendicular end face essential for low-loss splicing [53]. Cleaving quality was visually inspected to ensure the absence of cracks or chips on the fibre surface.

Following the cleaving operation, the fibres were fusion spliced using a Fujikura 90S+ automatic splicer, a core-alignment system designed for both standard and specialty fibres. The 90S+ employs high-resolution cameras and active core alignment technology to achieve optimal axial positioning before the fusion arc is applied. The splicer automatically monitors the joint during fusion and provides real-time splice loss estimation, expressed in decibels (dB), at the end of the operation [54]. Only splices with insertion losses below the manufacturer's acceptable threshold (typically ≤ 0.02 dB for single-mode fibres) were retained for use.

Representative images of the splicing process and the resulting joint geometry are shown in Figure 5.1.

Figure 5.1: Shot of the open splicer.

After the fusion splicing of the optical fibres, the joint, being temporarily without its

Figure 5.2: Splicing Process [51].

protective coating, remains mechanically fragile. For this reason, it is recommended to reinforce the splice using a splice protection sleeve. These heat-shrink sleeves shield the splice region and incorporate a stainless-steel inner rod that prevents bending and local pressure concentrations. As a result, they provide mechanical protection while preserving the optical transmission properties after splicing, which would otherwise be compromised by micro-bending or pressure-induced attenuation [55].

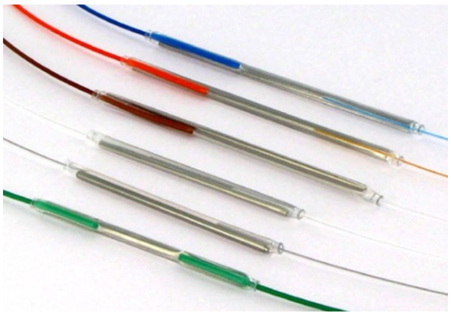

Figure 5.3: Splice Protection Sleeves.

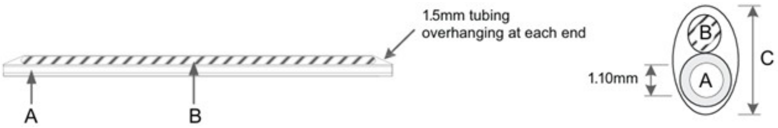

Figure 5.4: Splice Protection Sleeves scheme before shrinking.

5.2 Manufacturing of specimens

The composite specimens were fabricated using carbon/epoxy pre-impregnated fabrics supplied by Easy Composites Ltd. (model XC110 6k, 2×2 twill weave). This material features a nominal fibre areal weight of 200 g/m^2 and is reinforced with 6k T300 carbon fibres pre-impregnated with an epoxy resin system designed for low-temperature vacuum curing [56]. The main material characteristics are summarized in Table 5.2.

Table 5.2: Fabric Specifications.

Consolidate Thickness	0.45 mm
Resin Weight	38%
Min Cure Temperature	85°C
Max Cure Temperature	120°C
Max Service Temperature	115°C
Filament Diameter	7μm
Tensile Strength	521 MPa
Tensile Modulus	55.1 GPa

Each specimen measured 25 mm in width and 200 mm in length, and consisted of four plies stacked with identical fibre orientation. To ensure accurate cutting after curing, the prepreg sheets were initially trimmed into strips slightly wider than the target specimen, approximately 5 mm extra on each side, as the final geometry would later be defined by waterjet cutting.

Prior to lay-up, the glass substrate used as the mould base was thoroughly cleaned with acetone to remove contaminants. The working area was then defined using sealant tape, forming a rectangular boundary to contain the prepregs during lay-up. A thin layer of Easy Composites Mould Release Wax was uniformly applied within this boundary using a lint-free cloth, spreading the wax in small circular motions to ensure an even coating. After allowing the wax to dry for approximately 15 minutes, a layer of PP230 nylon peel ply (Easy Composites, Nylon 66 release fabric) was carefully laid over the prepared area [57]. This fabric facilitates demoulding after cure and produces a smooth, resin-rich surface on the specimen.

Figure 5.5: Wax-coated glass plate.

Figure 5.6: Prepreg strips laying on the peel-ply.

Figure 5.7: Optical fibre fixed on the peel-ply.

Figure 5.8: Breather and valve.

The first two carbon/epoxy layers were then positioned on the peel ply, ensuring correct alignment of the fibre directions. Next, the optical fibre, previously prepared and cleaned with isopropyl alcohol, was placed centrally and longitudinally along the specimen, leaving both fibre ends extending beyond the shorter sides of the laminate. The fibre was gently tensioned to keep it straight and lightly pressed into the prepreg surface to improve adhesion. The remaining two plies were then laid on top, completing the four-ply stack. Manual compression was applied over the lay-up to promote uniform contact between layers.

The optical fibre segments protruding from the specimen were kept clear of the uncured prepreg and any excess resin expelled during curing. They were fixed onto the underlying peel ply using masking tape to prevent movement and contamination. After removing the protective blue film from the outermost prepreg layer, an additional sheet of peel ply was applied, followed by a layer of breather cloth, a nonwoven polyester/polyamide felt fabric designed to allow air evacuation and absorb excess resin from the material.

A vacuum valve was then positioned over the breather cloth, and the entire assembly was sealed using vacuum bagging film firmly adhered to the sealant tape [58]. The bag was cut at the valve position and connected via a rubber hose to a vacuum pump through a dedicated connector. Once a steady vacuum was achieved, the assembly was transferred into the oven for the curing cycle, as shown in Figures 5.9 and 5.10.

According to the manufacturer's datasheet, the minimum cure temperature for the XC110 prepreg system is 85 °C [56]. The specimens were cured under vacuum at this temperature for approximately 16 hours, ensuring that vacuum integrity was maintained throughout the entire cycle. After curing, the composite plate was allowed to cool gradually to ambient temperature before demoulding.

A scheme of the obtained specimen is depicted in Figure 5.11.

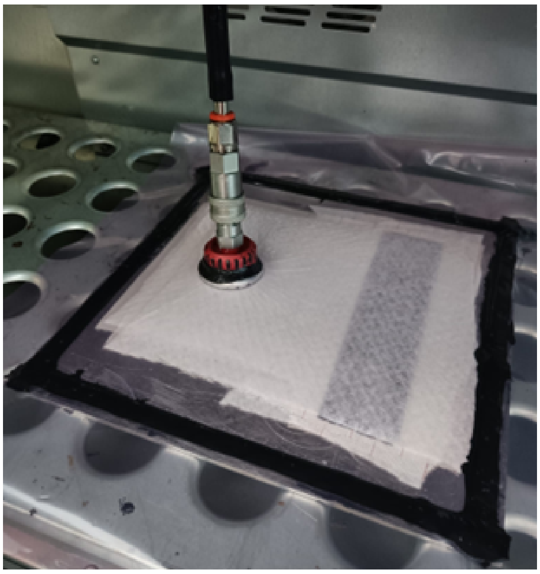

Figure 5.9: Glass plate in oven under vacuum.

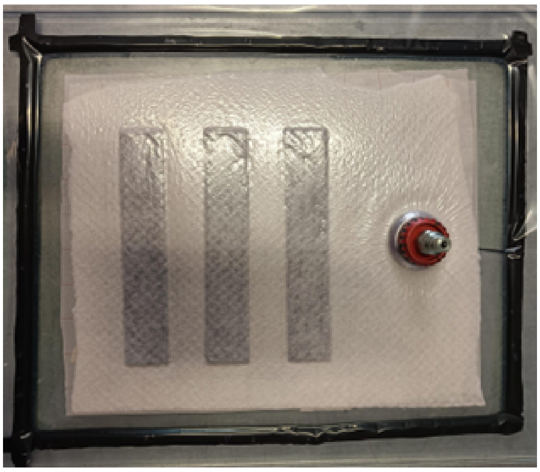

Figure 5.10: Specimens after cure, before demoulding.

Figure 5.11: Scheme of specimen with the optical fibre embedded between the second and the third layer.

5.2.1 Waterjet cutting

After curing, the composite laminates were trimmed along their vertical edges to obtain the nominal specimen width of 25 mm, in order to ensure a uniform cross-sectional area along the gauge length. This operation was carried out using a WAZER G6 Pro waterjet cutting system (Figures 5.12 and 5.13), which employs a high-pressure water stream mixed with fine abrasive sand to perform precise cutting on a wide range of materials [59]. The system's computer numerical control (CNC) enables high accuracy, allowing complex geometries to be produced within a few minutes.

Before the cutting process, the portions of the embedded optical fibres, sticking out of the material, were carefully folded back and secured onto the specimen surface using sealant tape, chosen for its water resistance during the operation, as depicted in Figure 5.14. This precaution prevented accidental damage or severing of the fibre ends during trimming.

It should be noted that only the specimen width was trimmed; the total length was left unchanged, as the optical fibres extended beyond the shorter edges of the laminate. Each specimen was firmly fixed to the cutting bed of the machine using stainless-steel screws to prevent vibration or movement during processing, as shown in Figure 5.15.

After cutting, the specimens were thoroughly cleaned to remove residual abrasive sand. They were then gently dried with a lint-free cloth. Finally, the sealant tape was carefully

Figure 5.12: Wazer waterjet.

Figure 5.13: Wazer open with cut bed.

Figure 5.14: Specimen with fibre folded before the cutting.

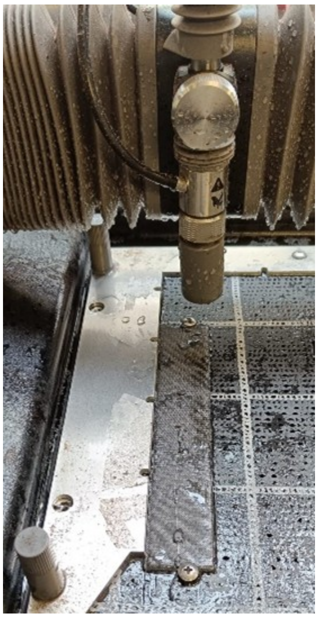

Figure 5.15: Specimen after the cutting, still fixed to the cut bed.

removed from the surface, leaving the optical fibres intact and ready for subsequent testing.

5.2.2 Application of Tabs

To prevent local damage during mechanical testing, the application of protective tabs at the gripping regions of composite specimens is essential. Tabs help to distribute the clamping pressure from the testing machine's grips and mitigate premature failure caused by stress concentrations or crushing near the ends of the specimen [60]; it has to be noted that tabs were employed only for the tensile-to-failure and fatigue test campaigns, since these tests involved repeated or high-load gripping cycles. The geometry and dimensions of the tabs were selected according to the recommendations of the ASTM D3039/D3039M standard for tensile testing of polymer-matrix composites. Based on this guideline, the tabs used in the present work had a length of approximately 44 mm, consistent with the nominal geometry of the composite specimens [60].

The tab material was a carbon-fibre composite laminate of lower stiffness compared to the main specimens, a choice intended to enhance strain compatibility and reduce the risk of interfacial debonding during loading.

Each tab was cut from a composite plate using the WAZER G6 Pro waterjet system. Following cutting, the tabs were lightly abraded with 400-grit sandpaper to remove the glossy surface layer and to promote better adhesion. Both the tabs and the specimen surfaces were subsequently cleaned with acetone to eliminate dust and residues prior to bonding.

Figure 5.16: Specimens with tabs and weight applied.

For the adhesive bonding, the SikaPower®-880 structural adhesive was used. This is a two-component, thixotropic, and fast-curing epoxy adhesive specifically designed for bonding carbon-fibre-reinforced polymer (CFRP) laminates [61]. It cures at room temperature, providing high shear strength, and resistance to fatigue and impacts. The formulation contains 0.3-mm glass beads, which act as spacers to maintain a uniform bond-line thickness between the tab and the specimen [61]. The adhesive was dispensed from 1:1 dual cartridges, and the two components were mixed until obtaining a homogeneous paste. A thin, uniform layer of the adhesive was applied to each tab surface, which was then positioned on the specimen ends under light compression. Small weights were applied on top of the assembly to stabilize the bonding area and to prevent slippage during curing. The adhesive bond was allowed to cure for approximately five hours at ambient temperature, after which a consistent and durable adhesion was achieved.

5.3 Luna ODiSI 6100

5.3.1 Components and Functioning

To enable strain or temperature measurement through distributed optical fibre sensing, a dedicated interrogator is required. In this work, all measurements were carried out using a Luna ODiSI 6100 system. The Luna ODiSI 6100 distributed sensing system is composed of four principal components: the interrogator unit, the remote measurement module, the optical connection cables, and the control workstation. Together, these elements form an integrated measurement chain capable of acquiring, processing, and transmitting high-resolution strain and temperature data along the optical fibre. The ODiSI platform is based on Rayleigh backscattering analysis and provides real-time acquisition of strain and temperature profiles with high spatial resolution [62, 63].

Figure 5.17: Luna ODiSI Components [62].

The interrogator unit represents the core of the system. It contains the swept-wavelength laser source, the interferometric detection module, and the digital control electronics required for real-time data processing. The interrogator performs continuous laser wavelength scans and processes the Rayleigh backscattered signals to obtain distributed strain or temperature measurements with sub-millimetre spatial resolution [64]. This module also includes the data acquisition hardware, cooling system, and communication interfaces for external control. The ODiSI 6100 can be operated locally or remotely through the ODiSI Control Software, which allows configuration of test parameters and visualization of real-time data [65].

The remote module is designed to extend the sensing capability of the interrogator to environments where direct instrument installation is not feasible, such as vibration testing rigs, thermal chambers, or large structural setups. It connects to the main interrogator via a ruggedized optical cable and provides low-loss optical routing to the sensing fibre. The module is equipped with internal optical switches and connectors that preserve signal

integrity while allowing flexible routing between channels. The design ensures that the laser source remains isolated from external mechanical or thermal disturbances, maintaining measurement stability and accuracy over long distances [66].
The connection cables play a critical role in ensuring system reliability and measurement fidelity. The ODiSI system employs armoured or reinforced single-mode fibre patch cords terminated with FC/APC connectors, chosen for their low insertion loss and minimal back reflection.
Finally, the control workstation, a dedicated PC equipped with the ODiSI Control and Analysis Software, serves as the user interface and data management hub of the system. It is used to configure acquisition parameters such as gauge pitch, measurement rate, and channel assignment, and to visualize strain or temperature maps in real time. The PC also stores the acquired data and enables post-processing and exporting [62, 65].

The system operates with single-mode fibres and offers dynamic measurement capability, making it suitable for static and fatigue tests in composite materials [51, 64].

5.3.2 Sensor Connection and Termination

Before connection to the interrogator, the sensing fibre must be prepared properly to ensure optical continuity and protect the system components. To this end, two auxiliary elements are attached to the fibre ends: the pigtail and the coreless fibre segment.
The pigtail is a short optical fibre, typically 1–2 metres long, featuring a factory-installed connector (such as an FC/APC or LC type) on one end and a stripped, bare fibre on the other. The bare end is fusion-spliced to the sensing fibre, while the connectorized end enables a secure and low-loss connection to the interrogator input port.

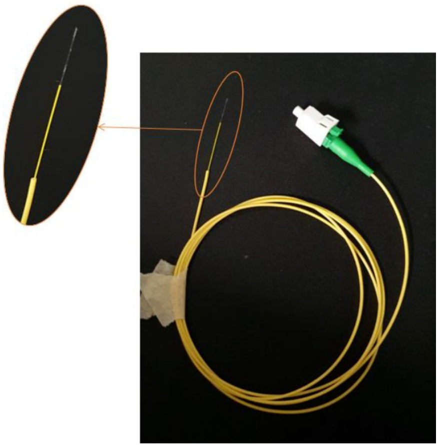

Figure 5.18: Pigtail.

At the opposite end of the sensing line, a coreless fibre is spliced to the terminal portion of the optical fibre. This segment consists of pure silica glass without a defined core, surrounded only by a cladding of similar refractive index, and is typically coated with a protective acrylate layer [67]. The absence of a core causes the light exiting the fibre to expand gradually within the coreless section, reducing the optical power density and minimizing back reflections at the fibre end. This design prevents undesired light feedback into the interrogator and enhances both optical stability and sensor durability during testing.

Luna Innovations supplies standard optical fibres, specifically the HD6S polyimide-coated low bend loss single-mode fibres. These fibres are factory-prepared with an integrated pigtail connector and a coreless termination, both designed to ensure low insertion loss and stable back-reflection characteristics across the sensing length [62]. Each Luna sensor is supplied with a unique electronic key (USB drive) containing the Sensor ID and calibration data, which allows plug-and-play recognition and automatic configuration by the ODiSI software suite. This system ensures that the interrogator immediately identifies the connected sensor, loading its reference spectral pattern and calibration coefficients for strain or temperature measurement [65].

However, due to the high cost of these pre-assembled Luna fibres, in this work, custom optical sensors were fabricated. The custom sensors were created by splicing together standard single-mode optical fibres with the appropriate pigtail and coreless sections, achieving similar performance at a significantly lower cost [51].

5.3.3 Optical Fibre Installation in ODiSI

Once the optical fibre was fully assembled, it was necessary to perform an identification and mapping procedure, unlike Luna's factory-calibrated sensors. During this process, the fibre's Rayleigh backscatter signature is acquired and stored as a reference "key". The backscattered light is interferometrically mixed with a portion of the original reference beam, producing an interference spectrum, a frequency-domain signal that represents the optical path differences between the reference and scattered light within the fibre [64].

By applying a Fourier transformation to the interference spectrum, the system converts the data from the frequency domain into the spatial domain, reconstructing the Rayleigh amplitude profile versus distance. The resulting profile is known as the Optical Frequency Domain Reflectometry (OFDR) spectrum, which displays the optical fibre's length, refractive index, and insertion and return losses at both the connector and terminal ends [62, 63].

The OFDR trace displays two main vertical red lines corresponding to the beginning (connector) and end (termination) of the fibre; to the right of the second line, the spectrum consists only of background noise. For a well-defined sensing signal, a minimum 5 dB signal-to-noise ratio between the fibre response and the noise level is required [62].

Any mechanical strain or temperature change along the fibre modifies the local refractive index and physical length, producing a small but measurable shift in the Rayleigh backscatter pattern. The magnitude of the frequency shift ($\Delta\nu$, in GHz) is then converted into strain (ε) or temperature (ΔT) using the following relation:

$$\Delta\nu = K_{\varepsilon} \cdot \varepsilon + K_T \cdot \Delta T \tag{5.1}$$

where K_ε and K_T are calibration constants representing the strain and temperature sensitivities of the fibre, respectively [63, 64].

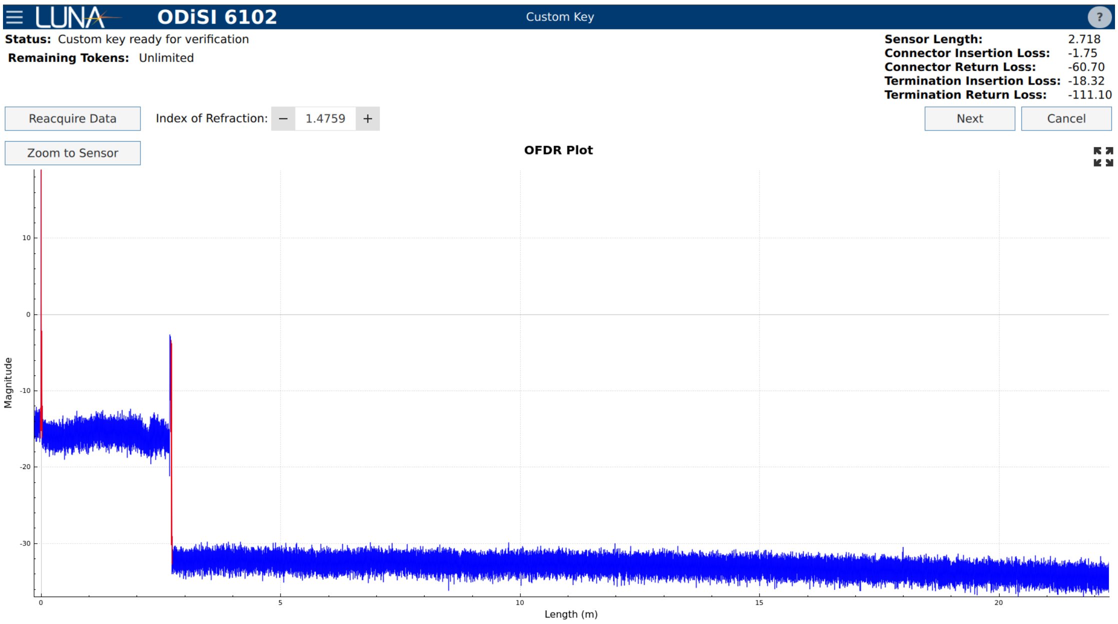

Status: Custom key ready for verification
Remaining Tokens: Unlimited

Sensor Length: 2.718
Connector Insertion Loss: -1.75
Connector Return Loss: -60.70
Termination Insertion Loss: -18.32
Termination Return Loss: -111.10

Index of Refraction: 1.4759

Figure 5.19: OFDR Spectrum.

Once the spectrum is validated, the system proceeds to the sensor calibration stage, where the operator specifies the intended measurement mode, strain or temperature. For both modes, calibration coefficients must be defined to translate the optical frequency shift (in GHz) into mechanical strain ($\mu\varepsilon$) or temperature (°C). For most standard single-mode fibres, the frequency–strain relationship is nearly linear, described by a single proportionality constant b, whereas the frequency–temperature relationship is linear only near ambient conditions and may require higher-order polynomial calibration for wider temperature ranges [63, 64].

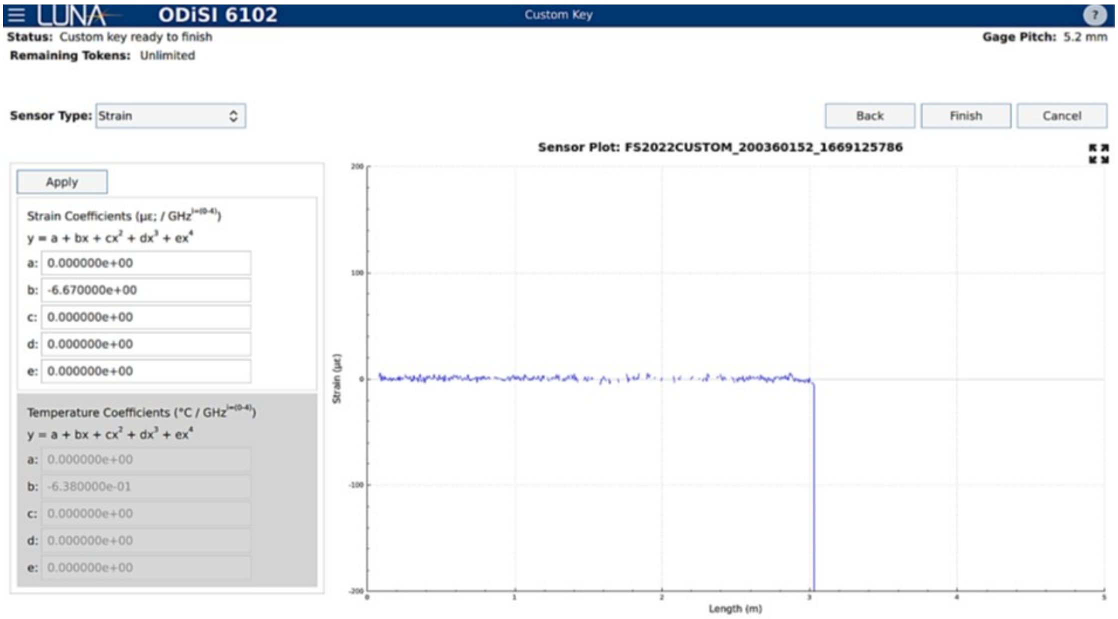

Status: Custom key ready to finish
Remaining Tokens: Unlimited
Gage Pitch: 5.2 mm
Sensor Type: Strain
Sensor Plot: FS2022CUSTOM_200360152_1669125786

Strain Coefficients (με; / $GHz^{i=(0-4)}$)
$y = a + bx + cx^2 + dx^3 + ex^4$
a: 0.000000e+00
b: -6.670000e+00
c: 0.000000e+00
d: 0.000000e+00
e: 0.000000e+00

Temperature Coefficients (°C / $GHz^{i=(0-4)}$)
$y = a + bx + cx^2 + dx^3 + ex^4$
a: 0.000000e+00
b: -6.380000e-01
c: 0.000000e+00
d: 0.000000e+00
e: 0.000000e+00

Figure 5.20: Sensor Calibration [51].

After completing the calibration, the fibre is ready for measurement. A critical acquisition parameter is the gauge pitch, defined as the spatial interval between consecutive sensing points along the fibre. The ODiSI 6100 allows selectable gauge pitches of 2.6 mm, 1.3 mm, or 0.65 mm, corresponding respectively to sampling frequencies of 250 Hz, 125 Hz, and 62.5 Hz [63, 65]. Users can also select between two operational modes:

- Full Optimisation, which halves the acquisition frequency for enhanced signal processing and precision;

- Maximum Rate, which prioritises the highest possible temporal resolution for dynamic measurements [63].

Prior to initiating a test, the zeroing (or baseline calibration) of the sensor must be performed to define the initial unstrained condition. The ODiSI software allows real-time visualisation of the strain distribution along the fibre during measurement, displaying both temporal evolution and spatial mapping of strain data. In cases where the sensor has been re-spliced or subjected to high strain, a Rekey operation can be executed to capture a new Rayleigh backscatter reference. This procedure is also recommended to re-center the strain range or to remove permanent strain gradients induced during prior loading [62, 65].

During acquisition, users can define specific gages of interest along the fibre to monitor local strain averages or to extract mean values over selected sections. Once the test is completed, the acquired data are automatically saved in a tab-separated values (TSV) format, where each column corresponds to the strain measured at each gage position, and each row represents the corresponding time step during acquisition. This format facilitates subsequent post-processing [51, 63].

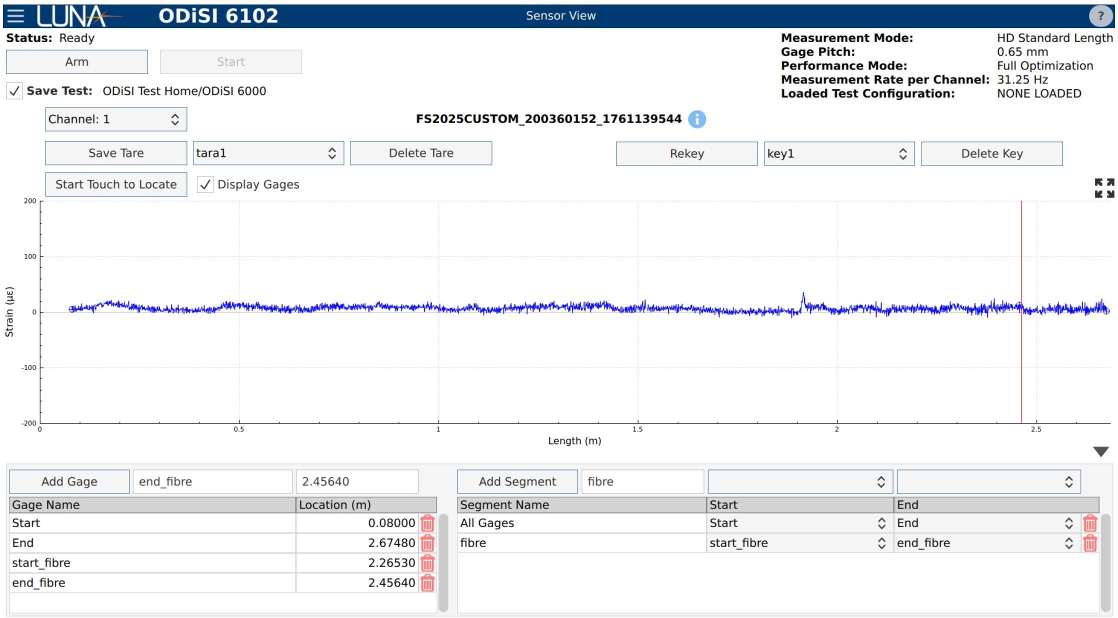

Status: Ready

☑ **Save Test:** ODiSI Test Home/ODiSI 6000

Measurement Mode: HD Standard Length
Gage Pitch: 0.65 mm
Performance Mode: Full Optimization
Measurement Rate per Channel: 31.25 Hz
Loaded Test Configuration: NONE LOADED

FS2025CUSTOM_200360152_1761139544

Save Tare: tara1
Rekey: key1
☑ Display Gages

Add Gage: end_fibre 2.45640

Gage Name	Location (m)
Start	0.08000
End	2.67480
start_fibre	2.26530
end_fibre	2.45640

Add Segment: fibre

Segment Name	Start	End
All Gages	Start	End
fibre	start_fibre	end_fibre

Figure 5.21: Optical Fibre Gages.

5.4 Testing Machines

5.4.1 Zwick Roell Z050

The Zwick Roell Z050 is a universal testing machine belonging to the AllroundLine series, specifically designed for precise mechanical characterisation of materials such as composites, polymers, and metals. It represents a compact version of conventional tensile testing machines, capable of applying loads up to 50 kN, which makes it particularly suited for laboratory-scale experimental investigations and coupon testing of advanced composite laminates [68].

Structurally, the Z050 consists of a dual-column electromechanical load frame that provides high stiffness and alignment accuracy during testing. Its design allows for a wide range of mechanical tests, including tensile, compression, and flexural tests, with dedicated gripping systems supplied for each configuration [68]. The crosshead speed can be adjusted within a broad range—from very low quasi-static rates to higher testing velocities—depending on the specimen material and testing standard requirements.

The machine is equipped with Zwick's testControl II electronics and managed through a software, which provides real-time closed-loop control of load and displacement.

In addition to traditional extensometers, the Z050 is equipped with an optical laser extensometer system, which enables non-contact strain measurement of the central portion of the specimen. The system tracks the displacement of a series of points marked on the sample surface using laser light, thereby providing a highly accurate measure of longitudinal strain without physical contact or risk of specimen disturbance. This capability was particularly advantageous when testing composite coupons with embedded optical fibres, where maintaining an undisturbed gauge section was essential to ensure correct sensor readings [51].

Figure 5.22: Zwick Roell Z050.

5.4.2 Instron 8801

The Instron 8801 is a servohydraulic testing system designed for both static and dynamic mechanical testing of materials and components. It is a compact, floor-standing fatigue testing machine particularly suited for fatigue, fracture mechanics, and durability investigations of metals, composites, and structural materials. The system provides a maximum axial load capacity of ±100 kN, allowing high-cycle and low-cycle fatigue tests under tension, compression, or alternating loading conditions [69].
Mechanically, the 8801 features a stiff, high-strength load frame equipped with hydraulic actuation for rapid and precise load application. The Instron 8801 relies on a servohydraulic actuator powered by a high-pressure oil supply, which enables extremely responsive force and displacement control across a wide dynamic range. This configuration allows the system to achieve high loading frequencies, typically up to several tens of hertz [69].
The machine is controlled by the Instron 8800MT digital controller, a modular and high-performance control system capable of closed-loop control for force, displacement, or strain. The 8800MT integrates seamlessly with Instron's universal software platforms, which provide an intuitive interface for test configuration, execution, and analysis and

supports complex loading histories for fatigue and durability studies.

Figure 5.23: Instron 8801.

Chapter 6

Tensile Tests

An unidirectional tensile test was performed to evaluate the capability of the hybrid optical fibre to measure strain with the same accuracy as a fully polyimide-coated fibre. The test was conducted along the same axis in which the hybrid fibre was embedded within the composite laminate. For this purpose, the Zwick Roell Z050 universal testing machine was employed.

The tensile test was carried out in strain-controlled mode at a crosshead speed of 1 mm/min, applying a maximum load of 10 kN. During the test, the optical fibre was connected to its pigtail and coreless termination and continuously interrogated in real time using the Luna ODiSI 6100 system [62]. The system was configured with a gage pitch of 0.65 mm and operated in Full Optimization mode, resulting in an acquisition frequency of 31.25 Hz; in parallel, the Zwick Roell machine acquired mechanical data at 50 Hz. Given the different acquisition frequencies of the Luna ODiSI system and the tensile testing machine, a preliminary data resampling was performed to interpolate the mechanical stress values to match the optical acquisition rate.

The strain distribution along the fibre revealed a clear distinction between the polyimide-coated and acrylate-coated sections embedded in the composite: the polyimide coating, due to its higher stiffness, accurately followed the deformation of the host composite; conversely, the acrylate coating, characterized by its lower elastic modulus, partially absorbed local deformation, resulting in slightly underestimated strain readings, as it is shown in Figures 6.1 and 6.2.

The strain profile also displayed a periodic oscillation pattern, which can be attributed to the alternating twill weave architecture of the carbon fabric: in fact, the undulating fibre tows produce local stiffness variations, leading to periodic modulation in the strain field.

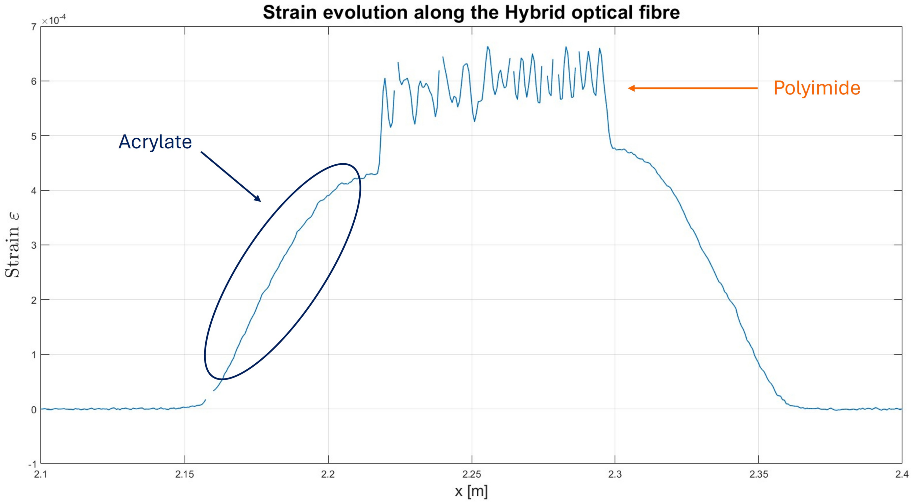

Figure 6.1: Strain evolution along the hybrid optical fibre, with the acrylate and polyimide trends.

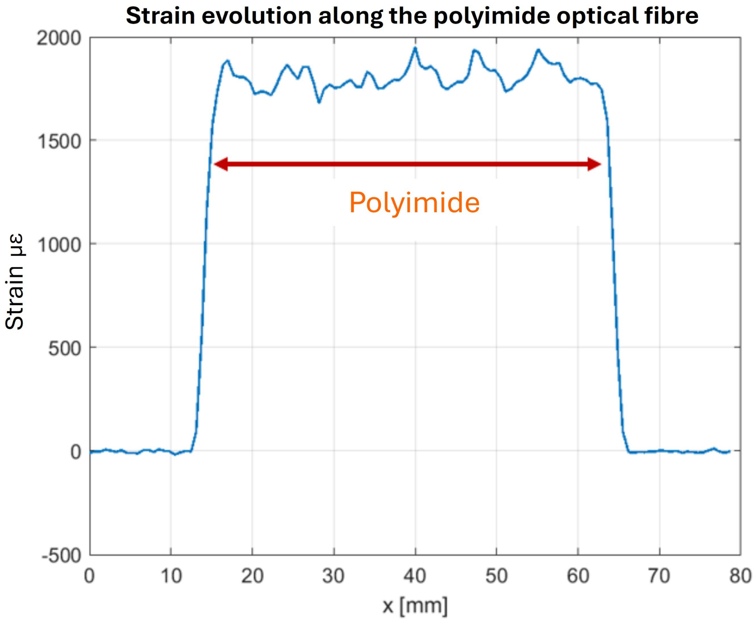

Figure 6.2: Strain evolution along the polyimide optical fibre [51].

The main objective of the test was to determine the elastic modulus E of the composite specimen by correlating the optical strain data with the mechanical stress data. Stress values were obtained from the tensile machine's load cell, while strain values were recorded by the distributed optical fibre sensor. Considering the material's homogeneous behaviour along the loading direction, a constant elastic modulus was expected throughout the entire gauge length. The elastic modulus was computed using the least-squares regression method:

$$E = \frac{\sum_{i=1}^{n}(\varepsilon_i - \bar{\varepsilon})(\sigma_i - \bar{\sigma})}{\sum_{i=1}^{n}(\varepsilon_i - \bar{\varepsilon})^2} \tag{6.1}$$

where ε_i and σ_i are the i-th strain and stress values, $\bar{\varepsilon}$ and $\bar{\sigma}$ represent their respective mean values, and n is the total number of data points [50].

Only the linear elastic region of the stress–strain curve was considered for the regression analysis.

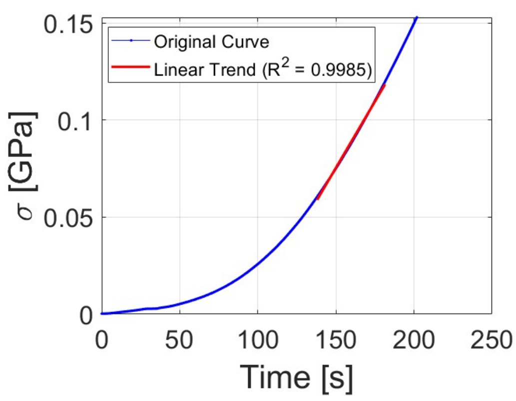

Figure 6.3: Sigma vs Time.

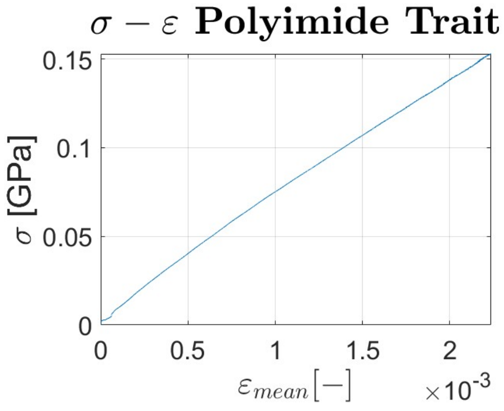

Figure 6.4: Sigma vs Epsilon.

The results demonstrated that the elastic modulus obtained from the hybrid optical fibre was comparable to that measured using a fully polyimide-coated fibre, as reported in previous experimental campaigns [50, 51]. This confirms that the inclusion of short acrylate-coated sections within the hybrid configuration does not compromise the fibre's ability to accurately track mechanical strain.

From the processed data, the elastic modulus along the polyimide-coated section was extracted and plotted in Figure 6.5, showing a uniform distribution consistent with theoretical expectations. In contrast, the acrylate-coated portions exhibited locally reduced apparent stiffness. Minor variations in the mean strain and modulus along the fibre length can be associated with small misalignments or non-uniform embedding of the fibre within the composite laminate during the curing process.

These findings confirm that the hybrid fibre architecture successfully combines the measurement fidelity of the polyimide-coated section with the mechanical robustness and ease of handling offered by the acrylate-coated ends. As such, the hybrid configuration represents a technically reliable solution for distributed strain monitoring in composite materials.

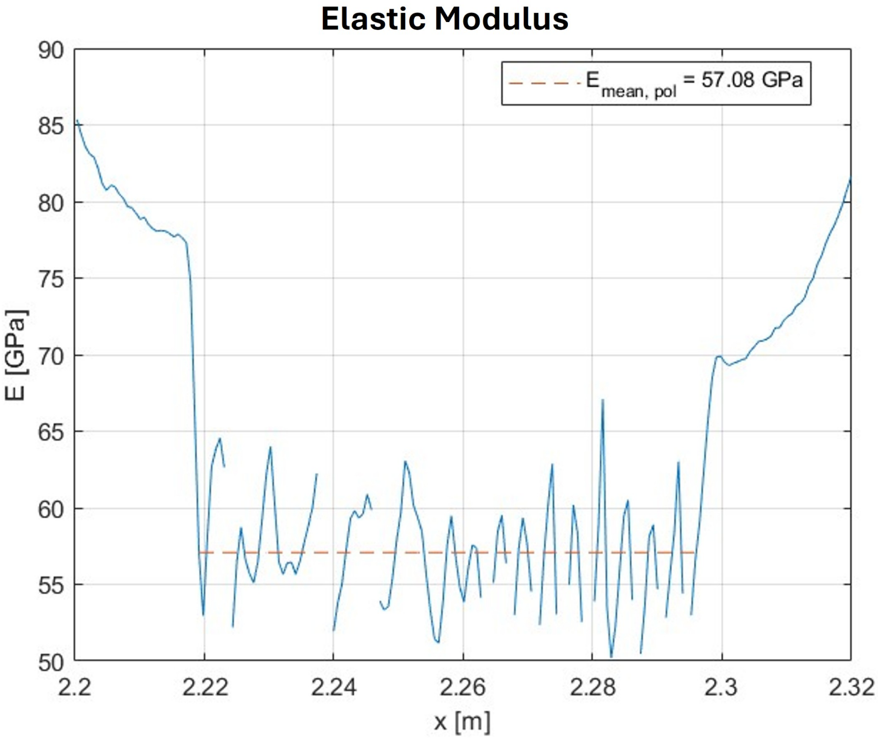

Figure 6.5: Elastic Modulus along the fibre.

6.1 Quasi-static Failure Tests

Before starting the fatigue testing campaign, preliminary tensile failure tests were carried out to determine the appropriate load levels to be applied to the specimens. For this purpose, the Instron 8801 universal testing machine was employed, operating under displacement control at a constant crosshead speed of 2 mm/min. Two specimens of identical geometry were tested, one containing a hybrid optical fibre embedded between the second and the third layers, and the other without any optical fibre.

The results of these tests indicated that the ultimate tensile strength (UTS) values of the two specimens were comparable, demonstrating that the presence of the embedded optical fibre did not significantly influence the overall tensile performance of the material.

Hence, the mean UTS value was considered for the subsequent fatigue testing campaign.

Specimen	**Layout**	**Width [mm]**	**Thickness [mm]**	$F_{\mathbf{max}}$ **[N]**	**UTS [MPa]**	**Mean UTS [MPa]**
Specimen #1	Without Fibre	24.45	1.81	24955.50	563.91	540.40
Specimen #2	With Fibre	24.45	1.81	22876.25	516.90	

Table 6.1: Quasi-static Failure Tests results.

Chapter 7

Fatigue Tests

The fatigue test campaign was conceived with a twofold aim: to compare the fatigue response of specimens containing embedded optical fibre sensors with that of reference specimens manufactured without any sensing element; the second objective was to assess the capability of the embedded optical fibre, interrogated using a Luna ODiSI system, to provide accurate strain measurements within the laminate under different load levels and test frequencies. In both cases, a tension–tension loading configuration was adopted.

Accordingly, this chapter is organised into two sections, each addressing one of these aims.

7.1 Influence of the embedded optical fibre on fatigue behaviour

To investigate the effect of embedding an optical fibre (placed between the second and third ply) on the fatigue response of the material, a fatigue test campaign was carried out on a total of 24 specimens: 12 with an embedded optical fibre and 12 without any sensor. Three load levels were considered, 50%, 65%, and 80% of UTS, as summarised in Table 7.1, and a stress ratio $R = 0.1$. For each load level, three specimens per configuration were tested.

The test frequency was set to 5 Hz as a practical compromise that allows the fatigue loading without causing a temperature increase which, in the case of composite materials, could alter the mechanical properties of the matrix, and thus influence the measured response.

Load Level (% UTS)	**Maximum Load Applied [kN]**	**Minimum Load Applied [kN]**
50%	11.957	1.1957
65%	15.57	1.557
80%	19.17	1.917

Table 7.1: Fatigue tests load levels.

Table 7.2 reports the number of cycles reached in each test, distinguishing between specimens that achieved the run-out limit (set at one million cycles) and those that failed; complete fracture was observed only at 80% UTS. The table also differentiates specimens with an embedded optical fibre from those without any sensor.

Optical Fibre		
Specimen	**%UTS**	**N Cycles**
#16	50%	1000000
#27	50%	1000000
#22	50%	1000000
#9	65%	1000000
#13	65%	1000000
#29	65%	1000000
#8	80%	126000
#12	80%	396000
#20	80%	29000

(a)

No Optical Fibre		
Specimen	**%UTS**	**N Cycles**
#7	50%	1000000
#14	50%	1000000
#17	50%	1000000
#3	65%	1000000
#23	65%	1000000
#26	65%	1000000
#1	80%	14000
#4	80%	137000
#6	80%	89000

(b)

Table 7.2: Number of cycles of specimens tested at different load levels: (a) specimens with embedded optical fibre, and (b) specimens without optical fibre.

To analyse the mechanical response of the specimens, several damage-related parameters were considered.

7.1.1 Elastic Modulus

During the fatigue testing campaign, the specimens were equipped with gripping tabs to prevent potential damage in the clamping regions of the testing machine, as described in Chapter 5. However, in order to ensure that the estimated stiffness values, and their subsequent reduction during cycling, were attributable exclusively to the material behaviour and not influenced by secondary effects such as possible slippage between the specimen and its gripping tabs, an extensometer was applied to a subset of specimens, at the three different load levels. The extensometer allowed direct measurement of strain, which, combined with the load data supplied by the testing machine and the cross-sectional area of the specimen, enabled the evaluation of the elastic modulus throughout the fatigue cycles.

For these specimens, both the stiffness and the elastic modulus were plotted as a function of the number of fatigue cycles. The trends of the two curves were found to be consistent with each other, differing only by a scaling factor dependent on the specimen's cross-sectional area and effective gauge length, according to the relation:

$$E = \frac{L_0}{A} K$$

Where:

- E is the elastic modulus;
- L_0 is the gauge length of the specimen;
- A is the cross-sectional area of the specimen;
- K is the stiffness.

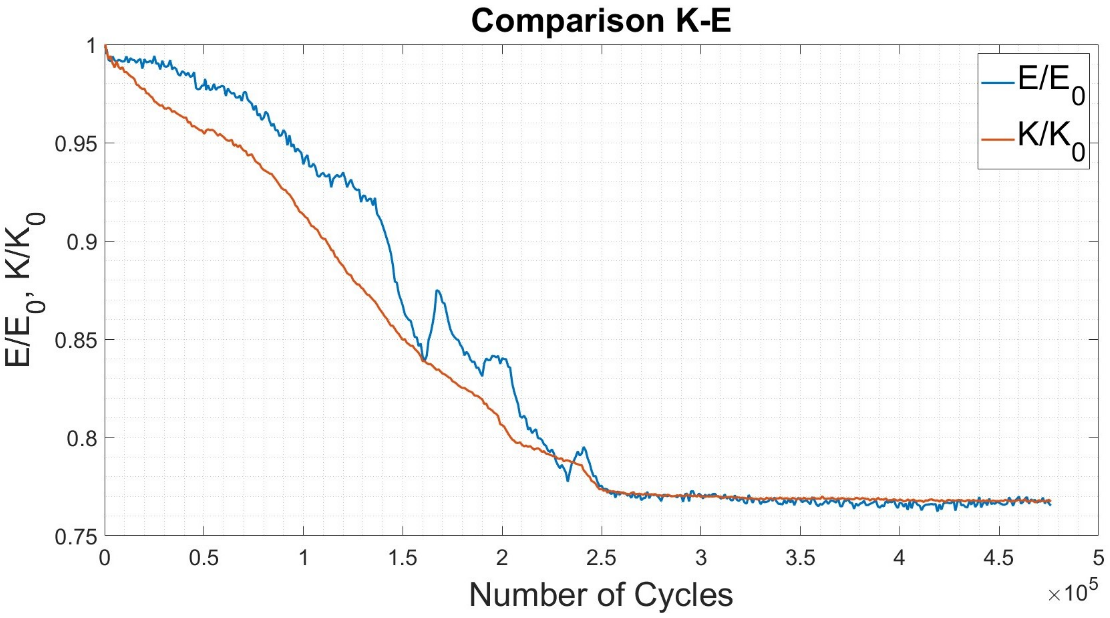

Figure 7.1: 65% UTS – Comparison K-E.

This comparison confirmed that the observed reduction in stiffness is primarily attributable to degradation of the specimen material itself. Consequently, stiffness, was adopted as the principal parameter for assessing damage evolution in the fatigue tests.

7.1.2 Stiffness Analysis

The application of a cyclic tension–tension load at different amplitudes induces progressive damage within the material, leading to a reduction in stiffness. In this work, the force–displacement relationship was used, where the stiffness is represented by the slope of the curve.

$$K = \frac{F}{\delta}$$

Where:

- F is the force applied
- δ is the displacement

During the initial loading cycles, regardless of the selected load level, a rapid decrease in stiffness was observed, followed by a stabilization phase likely due to microstructural rearrangements within the composite structure. Lastly, during the final cycles prior to failure, a pronounced and rapid decline in stiffness was recorded, indicating the imminent failure. This behaviour is consistent with recent studies reporting similar stiffness degradation mechanisms in fibre-reinforced polymer composites under cyclic loading [70].

At 50% of the UTS, all tested specimens successfully reached one million cycles without exhibiting any signs of failure. Examination of the stiffness evolution revealed that the stiffness reduction reached the 10% only for two specimens, while it was lower for the rest of the samples, without any differences between the "smart" specimens and the reference ones (Figure 7.2).

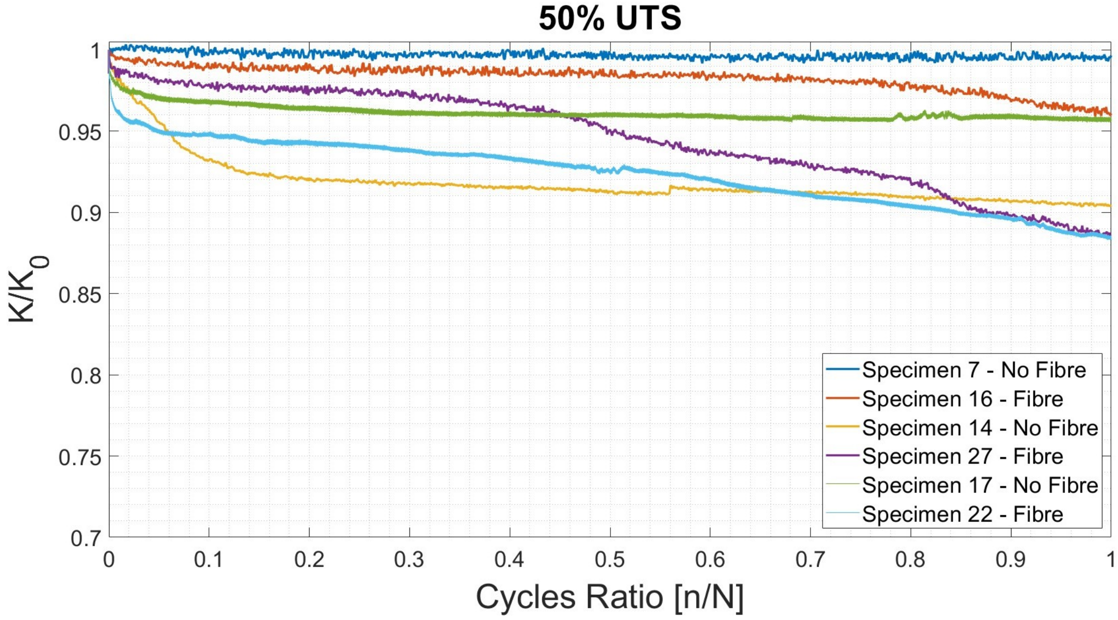

Figure 7.2: 50% UTS – Normalized Stiffness vs Cycle Ratio.

These results indicate, first, that failure was not expected to occur for many additional cycles for most specimens, and second, that the presence of the optical fibre does not meaningfully affect the stiffness of the specimen at a load level of 50% UTS.

When the applied load was increased to 65% of the UTS, the reduction in stiffness becomes more evident than at the previous load level, as shown in Figure 7.3. No meaningful difference was observed between specimens containing embedded optical fibres and those without; accordingly, neither group exhibited a substantially greater or faster stiffness degradation.

All specimens reached 1 million cycles without complete failure; however, unlike at the lower load level, significant delamination and crack formation were observed during testing. Although these damage mechanisms did not lead to complete material failure, they contributed to a marked reduction in stiffness, severely compromising the structural integrity of the specimens.

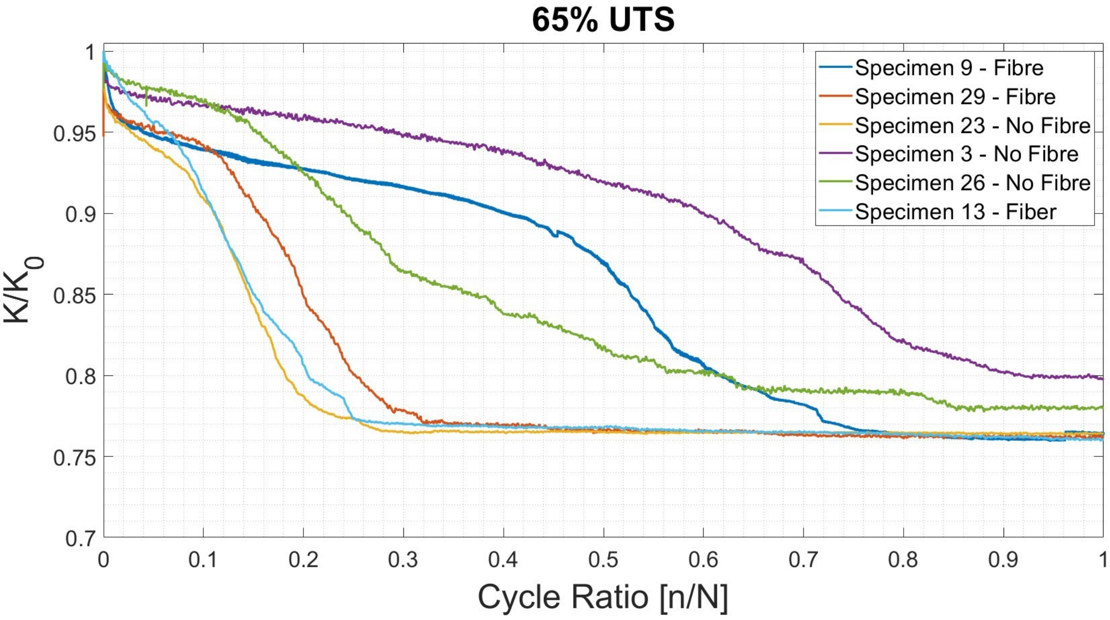

Figure 7.3: 65% UTS – Normalized Stiffness vs Cycle Ratio.

At 80% UTS, all specimens experienced failure, although the number of cycles to failure varied among them while remaining within the same order of magnitude.

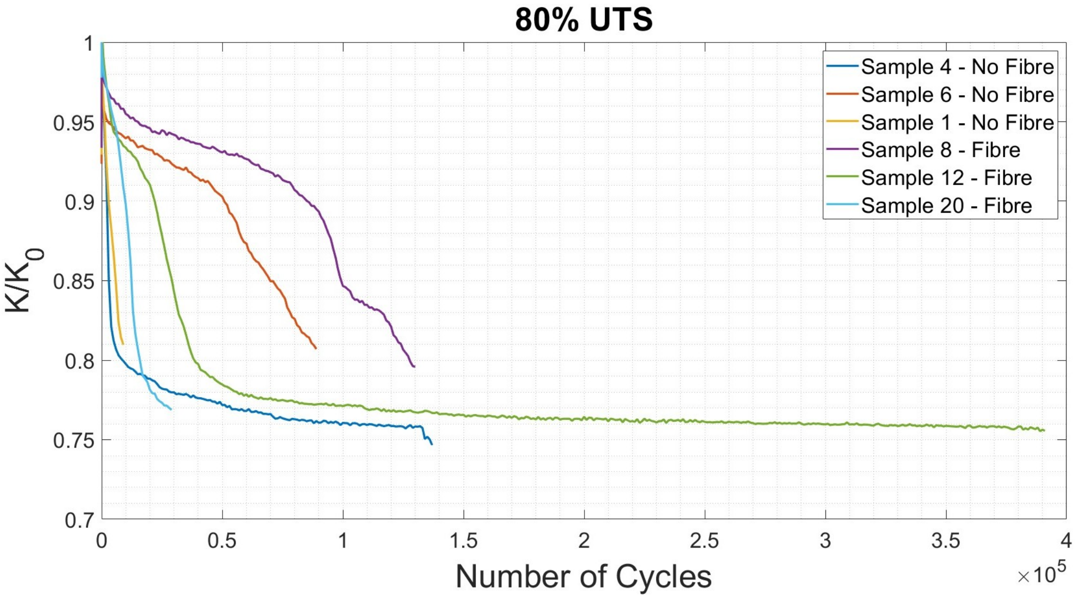

Figure 7.4: 80% UTS – Normalized Stiffness vs Number of Cycles.

However, this variability does not appear to be attributable to the presence of the embedded optical fibre, as both fibre-embedded and reference specimens failed at comparable cycle counts.

Instead, the observed differences are more likely associated with manufacturing-related imperfections, such as inclusions generated during the lay-up of the composite plies, or defects exposed at the specimen edges during waterjet cutting.

By normalizing the stiffness with respect to its initial value, it becomes evident that specimen failure tends to occur once the stiffness has decreased by approximately 20–25%, as shown in Figure 7.4.

7.1.3 Damage Index

The damage accumulation in the specimens was estimated based on the material's stiffness, and calculated using the following equation.

$$D_{\text{stiff}}(N) = 1 - \frac{K(N)}{K_0}$$

Where:

- K_0 is the initial stiffness
- $K(N)$ is the stiffness at cycle N

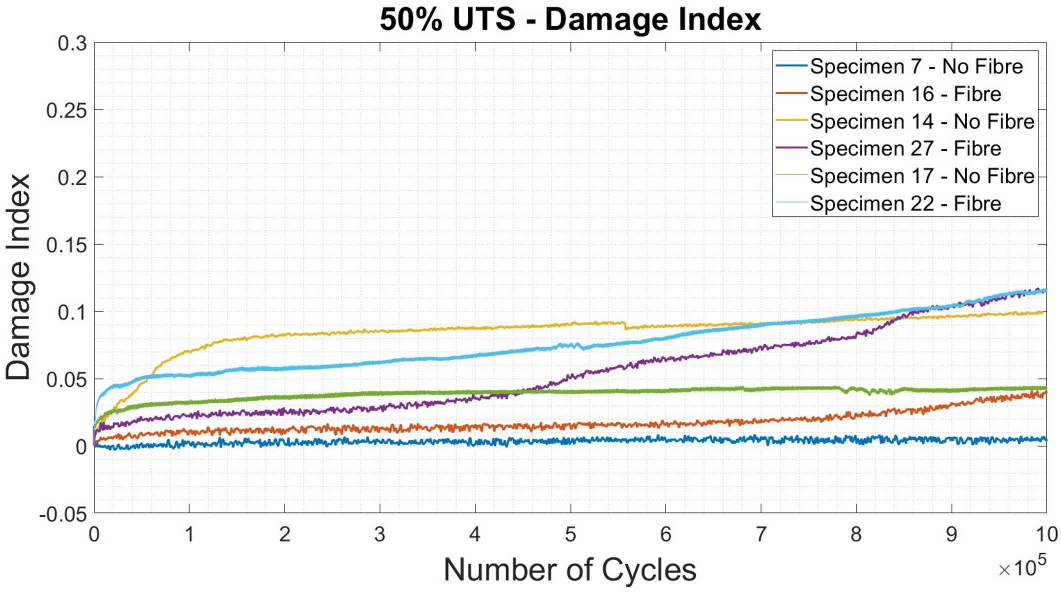

Figure 7.5: 50% UTS – Damage Index vs Number of Cycles.

At the beginning of the fatigue test, the damage is essentially zero; however, a rapid increase is observed within the first cycles, followed by a stabilization phase. In the cycles approaching failure, the damage rises once more, marking the final stage of degradation. The following figures illustrate the evolution of fatigue damage for the three investigated loading levels.

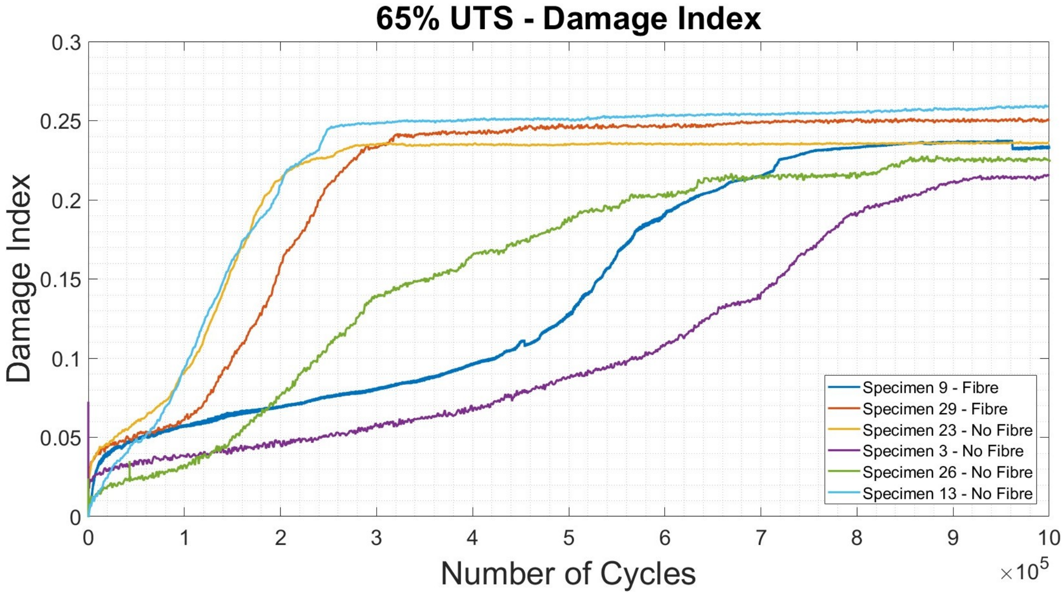

Figure 7.6: 65% UTS – Damage Index vs Number of Cycles.

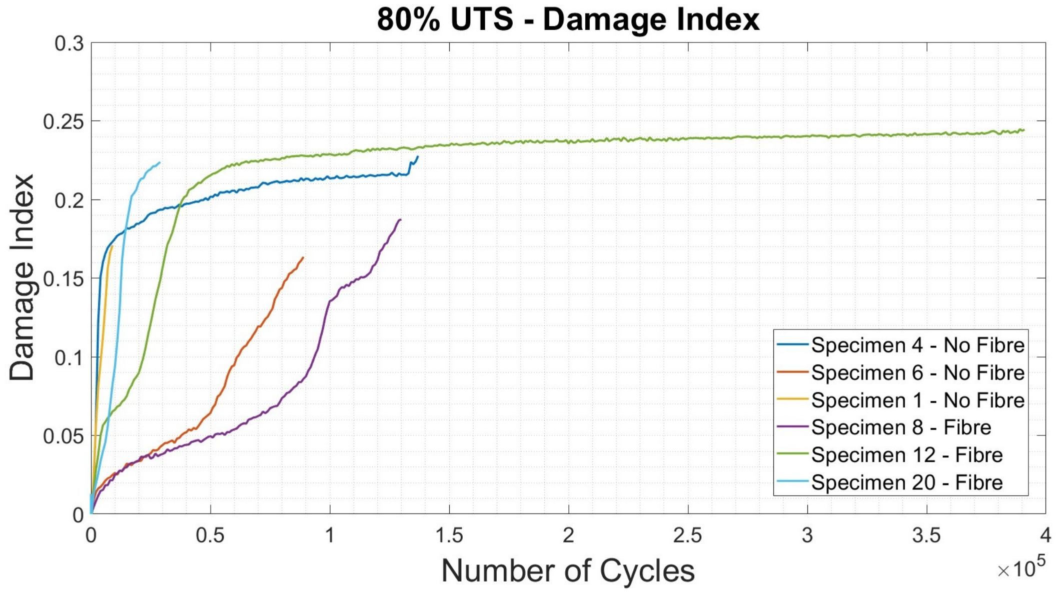

Figure 7.7: 80% UTS – Damage Index vs Number of Cycles.

7.1.4 Hysteresis Dissipated Energy

The force–displacement hysteresis loop provides a useful indicator of damage evolution during cyclic loading, as the area enclosed by the loop corresponds to the energy dissipated within the material.

$$E_h = \oint F \, dx$$

Where:

- F is the force applied
- dx is the displacement

At the beginning of the fatigue test, the hysteresis loop is narrow and nearly stable, reflecting a predominantly elastic response and a minimal internal damage due to molecular reorientation and minor interfacial activity, as observed by Panin et al.[71]. These initial loops serve as a baseline, representing the material in an essentially undamaged state.

As the number of cycles increases, the loop area gradually enlarges. This widening is indicative of progressive microstructural degradation, such as matrix microcracking, interfacial debonding, fibre–matrix sliding, and the formation of localized interfacial defects, all of which contribute to additional energy losses per cycle and thus contribute to the material's reduced capacity to store elastic energy [71]. The increase in dissipated energy can therefore be used as an indirect measure of the material's damage state. Several studies have shown that this trend becomes particularly pronounced at higher stress amplitudes, where the rate of damage accumulation accelerates and the hysteresis energy grows more rapidly [71, 72].

As remarked in previous sections, a further effect of fatigue progression is the reduction in stiffness, which is reflected in a decrease of the slope of the force–displacement loop. As internal damage accumulates, the material progressively loses its ability to store elastic energy efficiently and the loops can exhibit increasing residual (permanent) deformation, visible as a progressive rightward shift of the cycle [71]. The combination of loop-shape evolution and translation therefore provides a clear representation of the transition from an initially stable condition to a progressively more damaged state.

Close to failure, the hysteresis-loop typically undergoes a sudden enlargment associated to the rapid propagation of critical defects, and the response collapses once the specimen breaks [71]. The sequence consisting of a period of stable dissipation, gradual intensification, and a final abrupt increase followed by collapse, constitutes a characteristic signature of fatigue-induced degradation in composite materials [72].

The representative cycles shown in the following graphs illustrate these observations. The initial cycles exhibit narrow, steep loops; intermediate cycles show widening and a moderate loss of stiffness; and the final cycles reveal both significant loop enlargement and a marked decline in stiffness. Moreover, the difference in loop behaviour across loading levels underscores the influence of stress amplitude on energy dissipation: higher stress conditions lead to larger hysteresis areas and thus a more accelerated accumulation of fatigue damage [71, 72]. In Figures 7.8 7.9 7.10, for easier visualisation, only four representative cycles have been depicted.

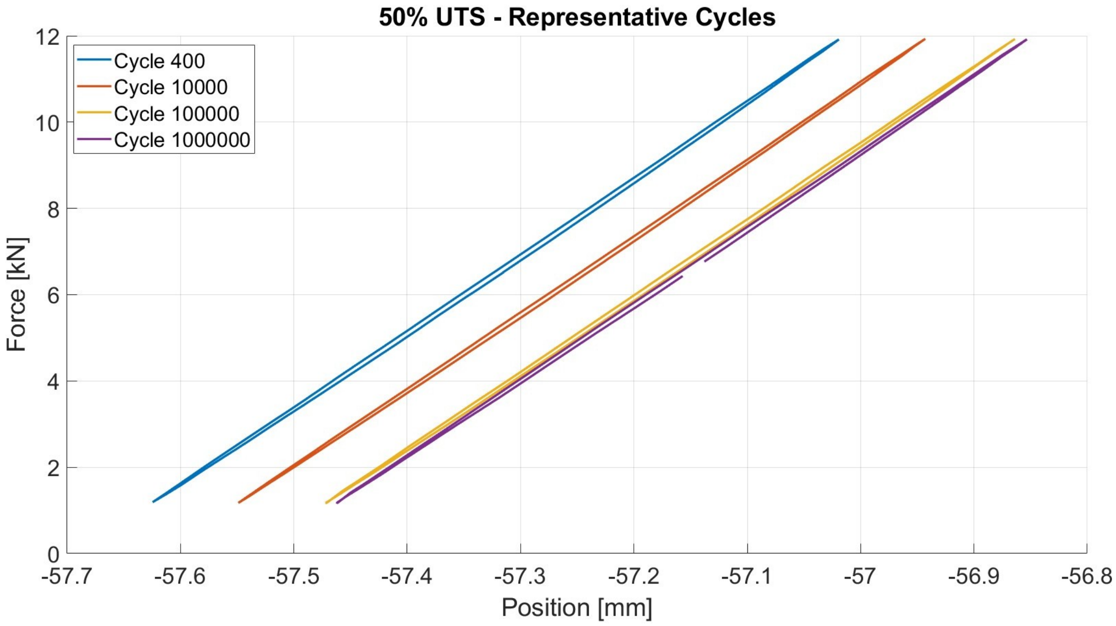

Figure 7.8: Analysis of the hysteresis dissipated energy of a specimen (#7) with no fibre tested at 50% UTS.

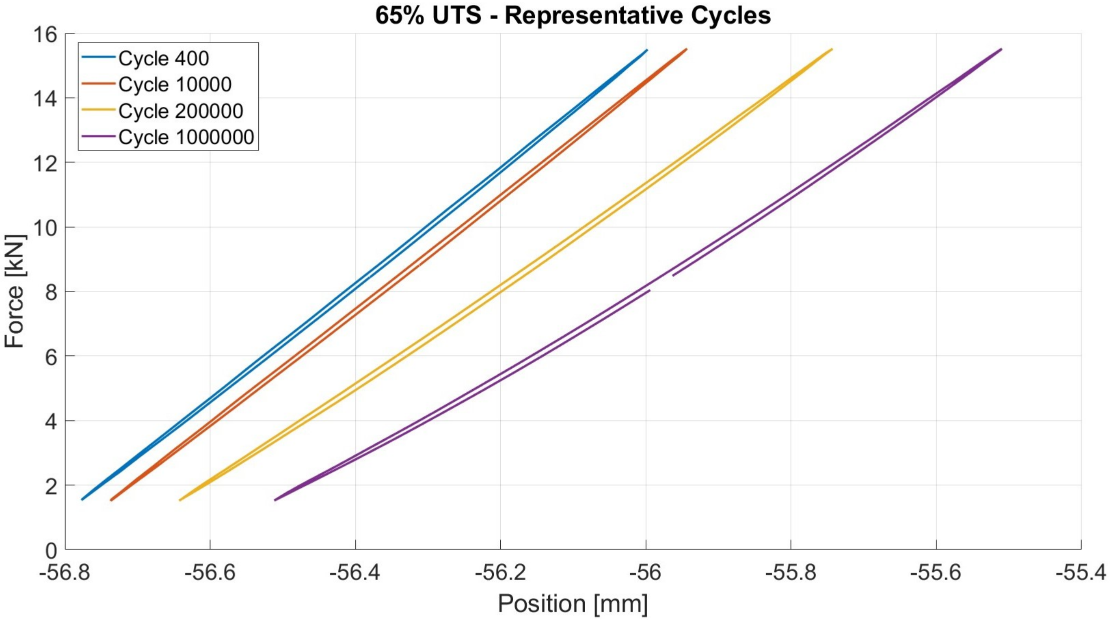

Figure 7.9: Analysis of the hysteresis dissipated energy of a specimen (#29) with embedded fibre tested at 65% UTS.

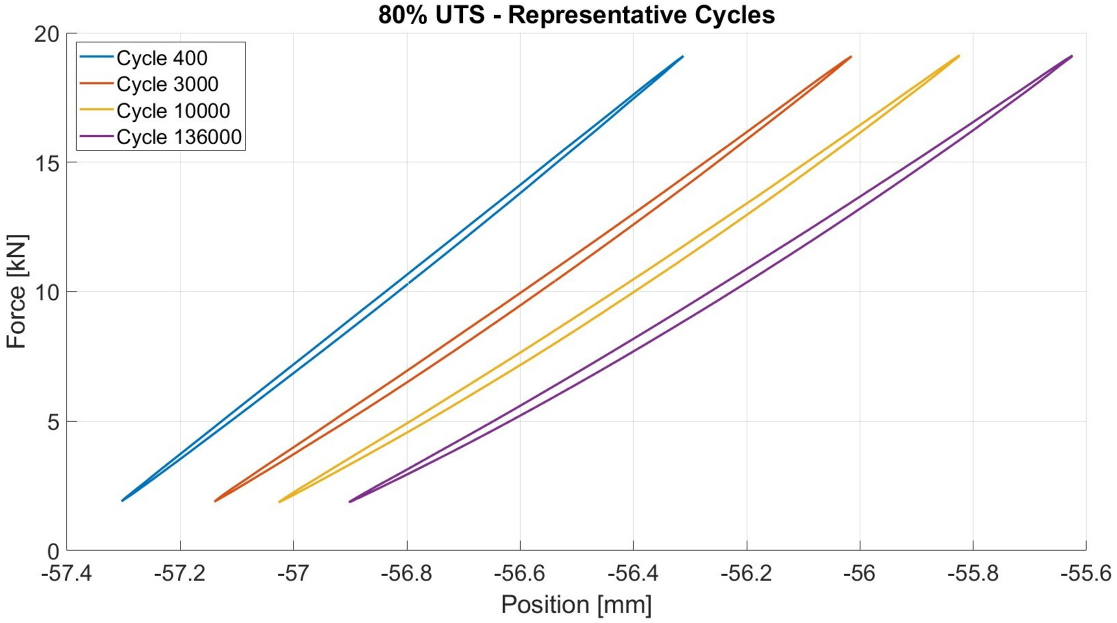

Figure 7.10: Analysis of the hysteresis dissipated energy of a specimen (#4) with no fibre tested at 80% UTS.

Rather than analysing each fatigue cycle individually, the overall effect of cyclic loading can be captured by considering their cumulative contribution, expressed as the energy accumulated throughout the test. The accumulated energy $E_{h,\mathrm{cum}}$ is therefore defined as the sum of the energy dissipated over all cycles (equation 7.1), and it provides an integral measure of progressive material degradation by accounting for the effects of the entire loading history.

$$E_{h,\mathrm{cum}}(N) = \sum_{i=1}^{N} E_h(i) \tag{7.1}$$

In practical terms, using cumulative energy has two main advantages: it captures the entire fatigue history into a single parameter that can be directly compared across specimens and test conditions, and it is typically less affected by cycle-to-cycle fluctuations than per-cycle indicators, thereby making long-term damage accumulation trends easier to recognise [71,72]. More generally, since fatigue damage and the associated stiffness loss evolve progressively with cycling, cumulative dissipated energy provides a physically meaningful indicator of the evolving damage state [70,72].

Figures 7.11, 7.12, 7.13 show the hysteresis energy per cycle compared to the cumulative energy for each load level. As expected, the higher the load level, the higher the accumulated energy; in detail, $E_{h,\mathrm{cum}}$ reaches around 400 J for the 50% UTS, 600 J for the 65% UTS, and 800 J for the 80% UTS.

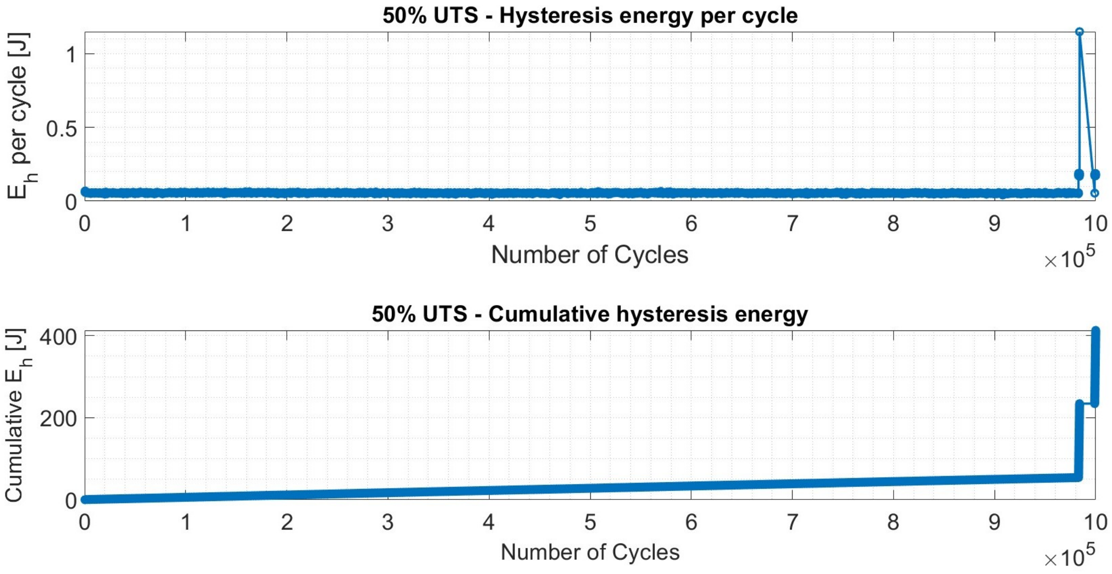

Figure 7.11: Hysteresis Energy per Cycle and Cumulative Hysteresis Energy for a specimen (#7) with no optical fibre subjected to 50%.

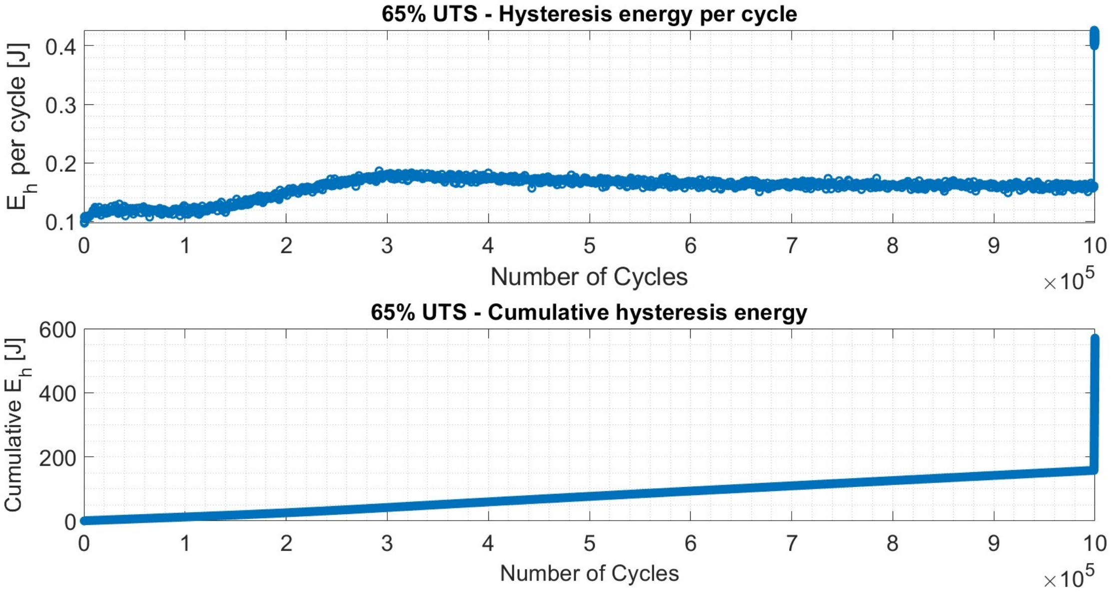

Figure 7.12: Hysteresis Energy per Cycle and Cumulative Hysteresis Energy for a specimen (#29) with embedded fibre subjected to 65%.

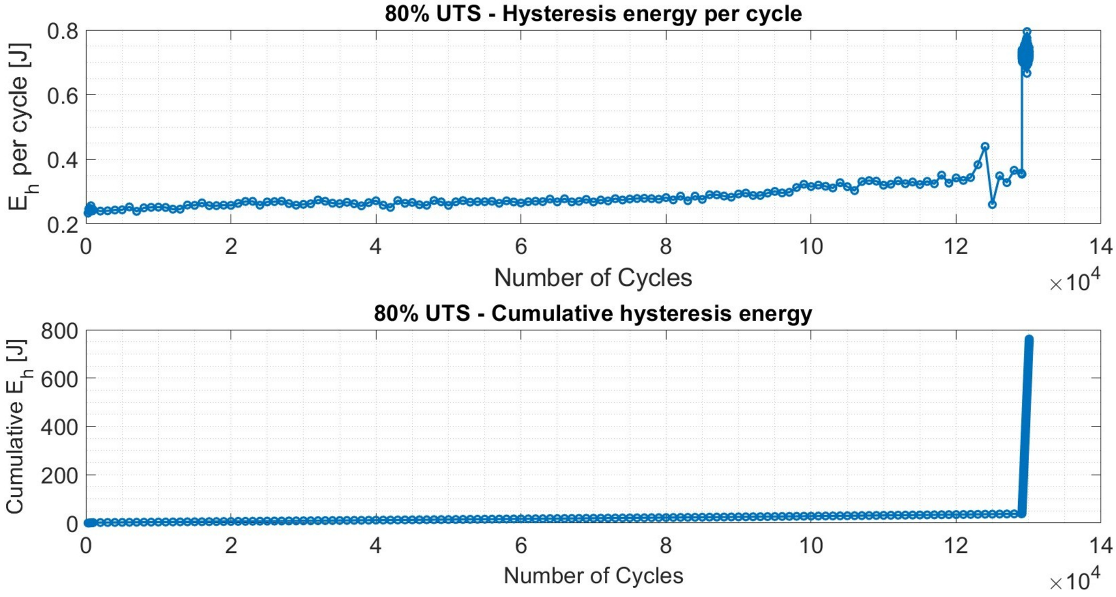

Figure 7.13: Hysteresis Energy per Cycle and Cumulative Hysteresis Energy for a specimen (#8) with embedded fibre subjected to 80%.

7.1.5 S-N Curves

As highlighted in the previous sections, the reduction in stiffness is a useful indicator of the material damage state. In particular, the extent of stiffness loss observed prior to failure depends on the applied load level; at 80% of the UTS, the stiffness decrement at the onset of fracture typically falls in the 20–25 % range.

This observation suggests the possibility of defining a maximum allowable threshold beyond which the specimen enters a condition associated with potential failure. Depending on the intended function of the final component, different threshold values may be selected. Indeed, even if the reduction in stiffness is not sufficient to cause catastrophic failure, it nonetheless alters the mechanical response of the component.

Therefore, if the sole requirement is to avoid complete rupture, a threshold greater than 15% may be adequate; however, if preserving a mechanical performance close to the original one is of greater importance, a more restrictive threshold must be adopted.

For this reason, when constructing logarithmic stress versus number of cycles (S–N) curves, specimen "failure" may be defined either as the occurrence of complete fracture or as the reaching of a prescribed stiffness reduction threshold; the corresponding cycle count is then taken as the fatigue limit associated with that criterion.

The S-N curves were constructed on a double-logarithmic scale by plotting the alternating stress, σ_a, against the number of cycles to failure, N_f, and fitting the data using the Basquin relationship 7.2 [73].

$$\sigma_a = \sigma'_f \, N_f^b \tag{7.2}$$

where σ'_f is the fatigue strength coefficient and b is the fatigue strength exponent.

To identify σ'_f and b, the equation was linearised and a least-squares regression was performed.

$$Y = \log_{10}(\sigma_a), \qquad X = \log_{10}(N_f), \tag{7.3}$$

$$Y = \log_{10}(\sigma'_f) + bX. \tag{7.4}$$

In addition, for each fitted curve, the corresponding Owen lower bound was computed as:

$$Y_{\text{LB}}(X) = \hat{Y}(X) - K_{\text{Owen}}\, s, \tag{7.5}$$

where s is the standard error of Y about the regression line, and K_{Owen} is a factor determined by the selected confidence and reliability levels, as well as by the number of specimens considered; in particular in this work it was chosen a level of confidence of 90% and a level of reliability of 95%, leading to a K_{Owen} of 2.650 for 9 specimens per category.

Figure 7.14 shows S-N Curves where the failure threshold was set at a decrement of stiffness of 10%.

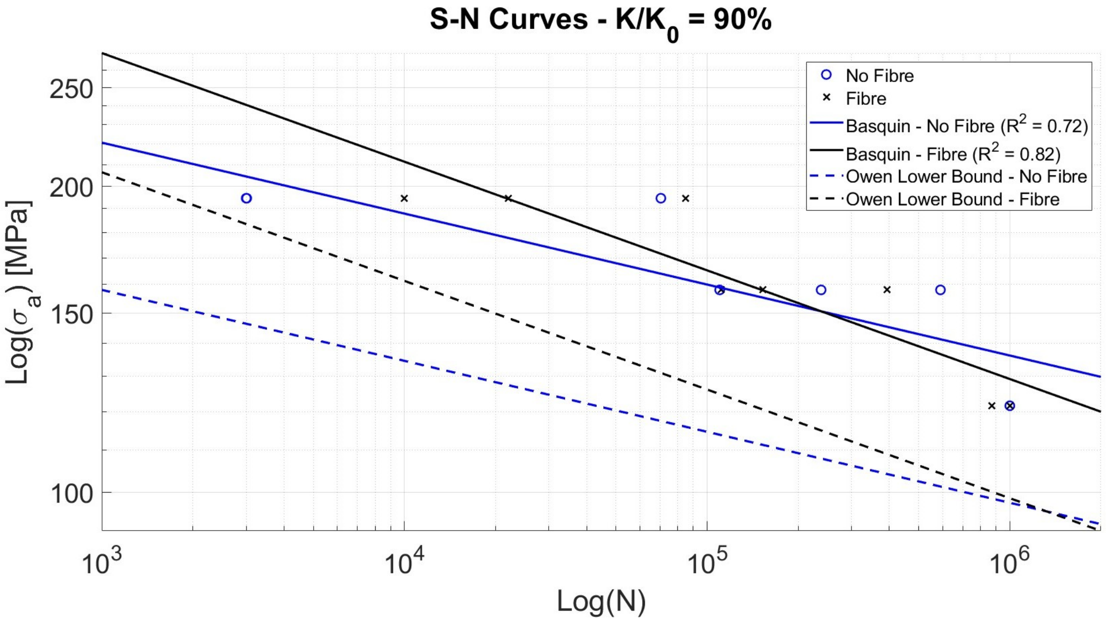

Figure 7.14: S-N Curves for a decrease of stiffness of 10%.

To verify that the presence of the embedded optical fibre did not affect the fatigue life of the specimens, an ANOVA test was performed on the two groups. To this end, the stress values from the S–N curves for the 10% of stiffness loss were shifted (normalised) to a reference life of 10^6 cycles, and the ANOVA was then applied. The test returned a p-value of 0.4642, which is greater than the chosen significance level (i.e., 0.05, or 5%). Therefore, it can be concluded that the two groups are not statistically different, as also shown in the box-plots in Figure 7.16.

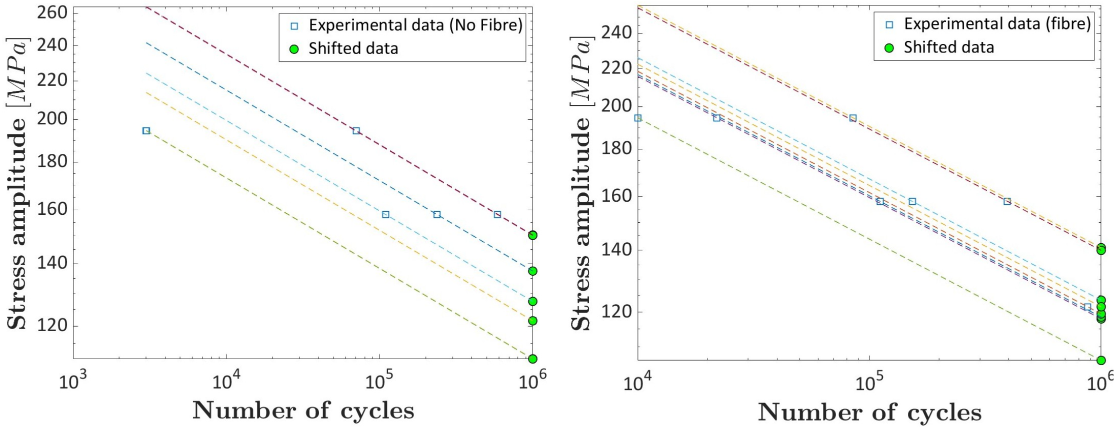

(a) (b)

Figure 7.15: Shifted S-N data for specimens without (a) and with (b) optical fibre.

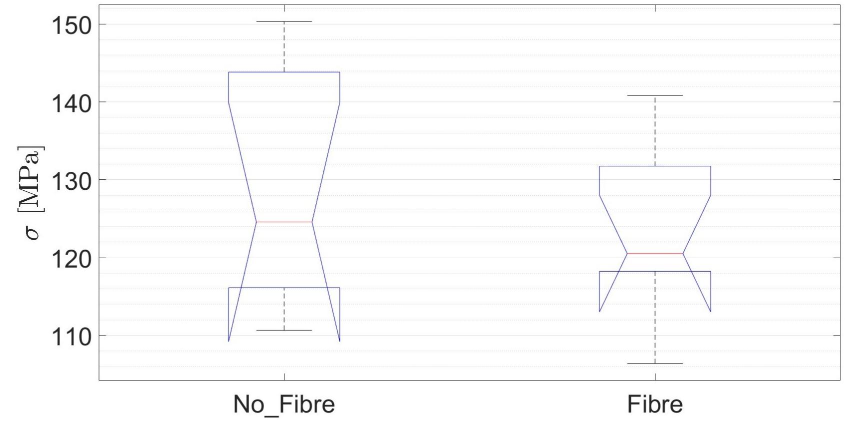

Figure 7.16: Boxplot Anova.

7.2 Optical Fibre Strain Measurements

This section investigates whether embedded optical fibres can accurately capture the strain developing within the laminate during tension–tension fatigue testing, with the load applied along the optical fibre longitudinal direction. In particular, the fibre response was examined as a function of both the applied load level and the test frequency. Test frequencies of 0.5, 1, 2, and 5 Hz were considered. At each frequency, the protocol consisted of 50 cycles at 50% UTS, followed by 50 cycles at 65% UTS and 50 cycles at 80% UTS.

In addition, to highlight potential differences in strain reading performance associated with the fibre coating, three specimens were considered, each embedding an optical fibre with a different coating type: a fully polyimide-coated fibre, a fully acrylate-coated fibre, and a hybrid-coated fibre, as described in Chapter 5.

Lastly, the study aimed to verify whether the optical fibre could continue to provide reliable strain measurements after being subjected to a large number of fatigue cycles at relatively high load levels and frequencies.

7.2.1 Frequency and Load influence

All three specimens were tested at the three prescribed load levels; however, their measurement response differed noticeably.

At 0.5 Hz (Figure 7.17), the fibre fully coated with acrylate was able to track the strain signal at all load levels. Nevertheless, owing to the compliant nature of the acrylate coating, the laminate deformation is not fully transmitted to the fibre core, since part of the deformation is effectively absorbed within the coating. As a result, the strain recorded by the interrogator is systematically lower, which in turn leads to an apparently higher elastic modulus.

By contrast, both the fully polyimide-coated fibre and the hybrid fibre, featuring a central polyimide-coated segment, provided a more faithful strain readout. The measured strain is therefore higher than that obtained with the fully acrylate-coated fibre, and the corresponding elastic modulus is lower and thus closer to the expected value, consistently with the earlier discussion and with findings reported in the literature [50, 51].

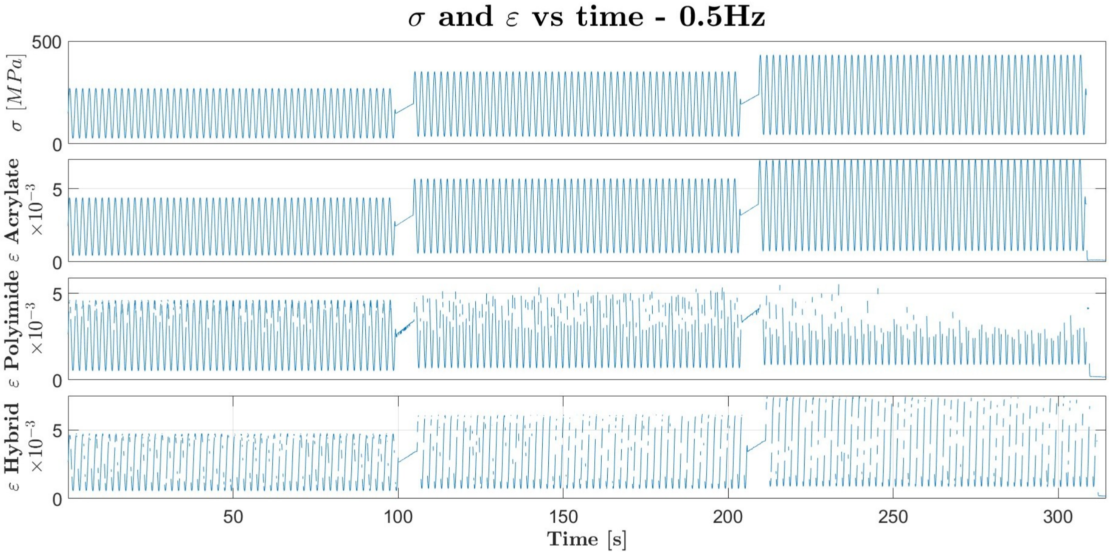

Figure 7.17: Stress and Strain for acrylate, polyimide and hybrid optical fibres, at 0.5 Hz.

Despite the high accuracy achieved with polyimide-based coatings, these fibres are extremely thin and stiff. Under the highest load level (80% UTS), the associated strain amplitudes could not be reliably captured by the Luna ODiSI interrogator, resulting in a sequence of “Not a Number” (NaN) or "Missing Values" entries in the exported TSV data.

A high incidence of NaNs was observed primarily for the polyimide-coated and hybrid fibres at 80% UTS already at 0.5 Hz; conversely, NaNs were also encountered for the acrylate-coated fibre when tests were performed at higher frequencies, even at lower load levels (Figures 7.18,7.19). This indicates that the ability to return valid (non-NaN) strain data depends on both the applied load level and test frequency, with a markedly stronger sensitivity for the polyimide-coated fibre compared to the acrylate-coated one.

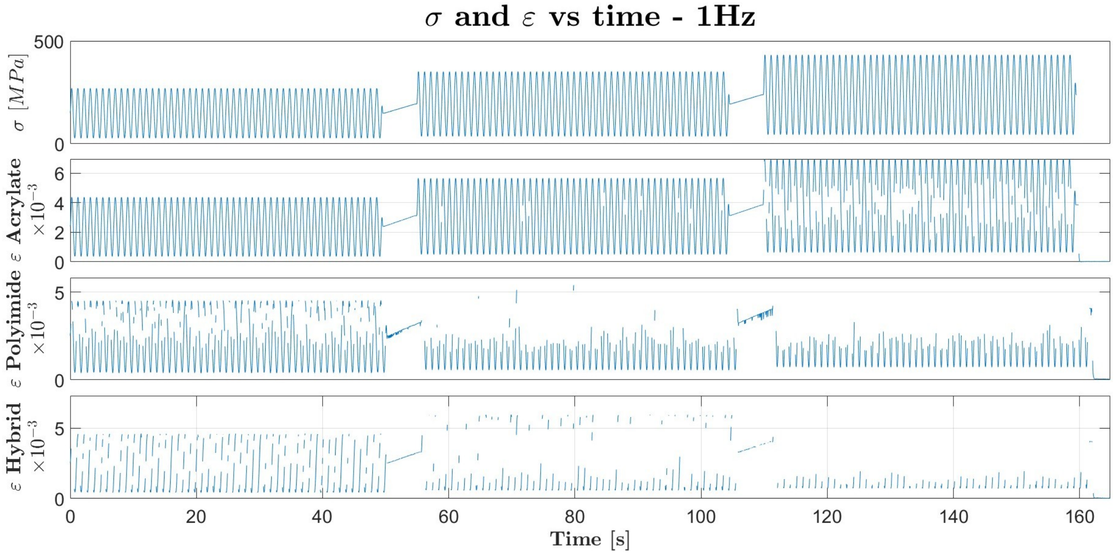

Figure 7.18: Stress and Strain for acrylate, polyimide and hybrid optical fibres, at 1 Hz.

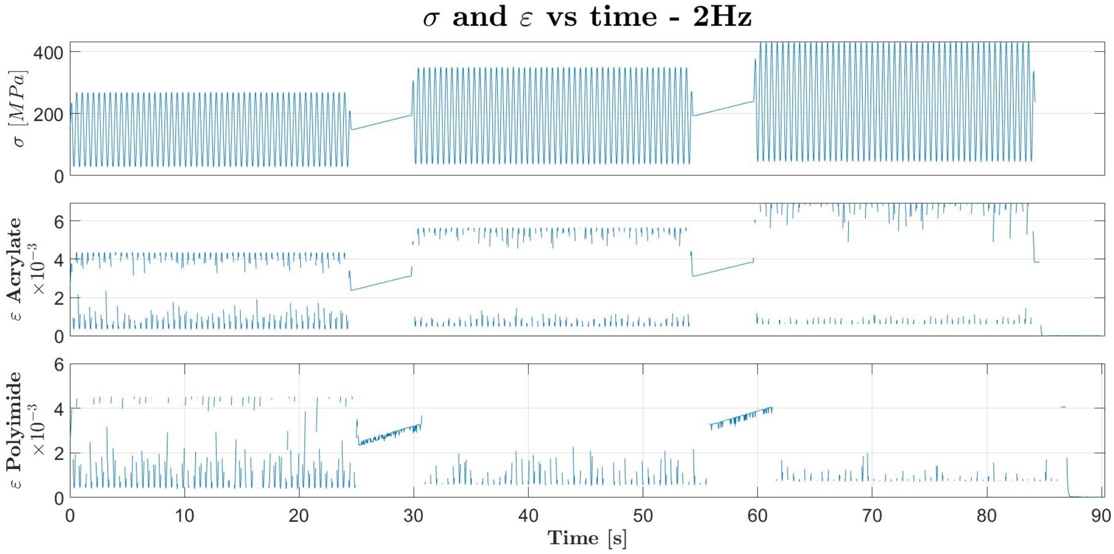

Figure 7.19: Stress and Strain for acrylate, polyimide and hybrid optical fibre, at 2 Hz.

For all three fibre configurations, the elastic modulus derived from the optical measurements decreases progressively with cycle count. This reduction is negligible at 50% UTS, also because only a limited number of cycles (50 cycles) were recorded at all load levels, whereas a more evident decrease is observed at the subsequent load levels, as shown in Figure 7.23. As outlined in the previous sections, and similarly to the observed stiffness degradation, this trend is attributed to the accumulation of damage mechanisms within the laminate. To verify that the observed elastic modulus trend is reliable, the stiffness evolution was also plotted using data obtained exclusively from the testing machine, and therefore independent of the optical fibre measurements.

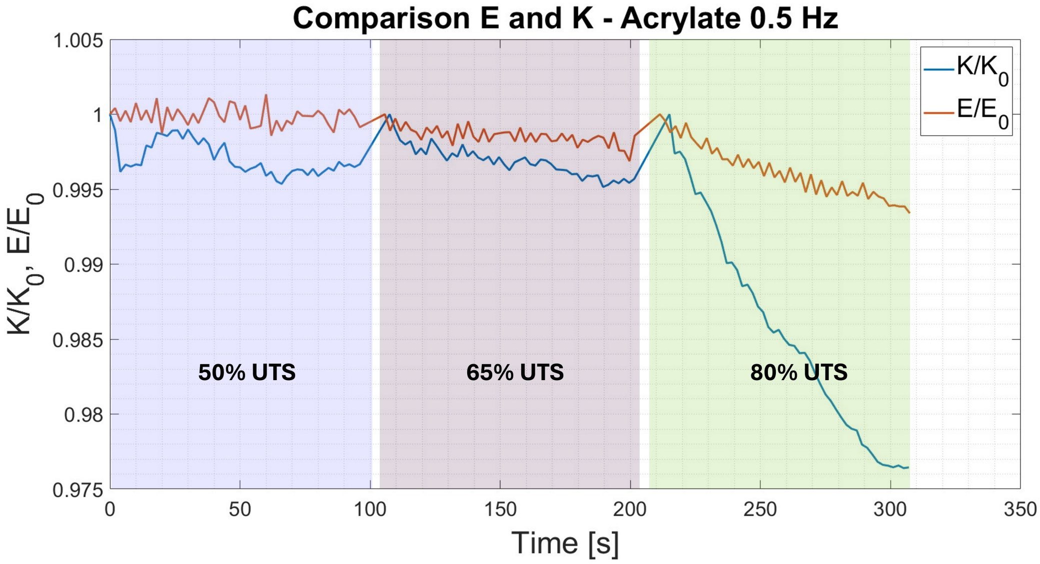

Figure 7.20: Comparison E-K of acrylate-coated fibre at 0.5Hz.

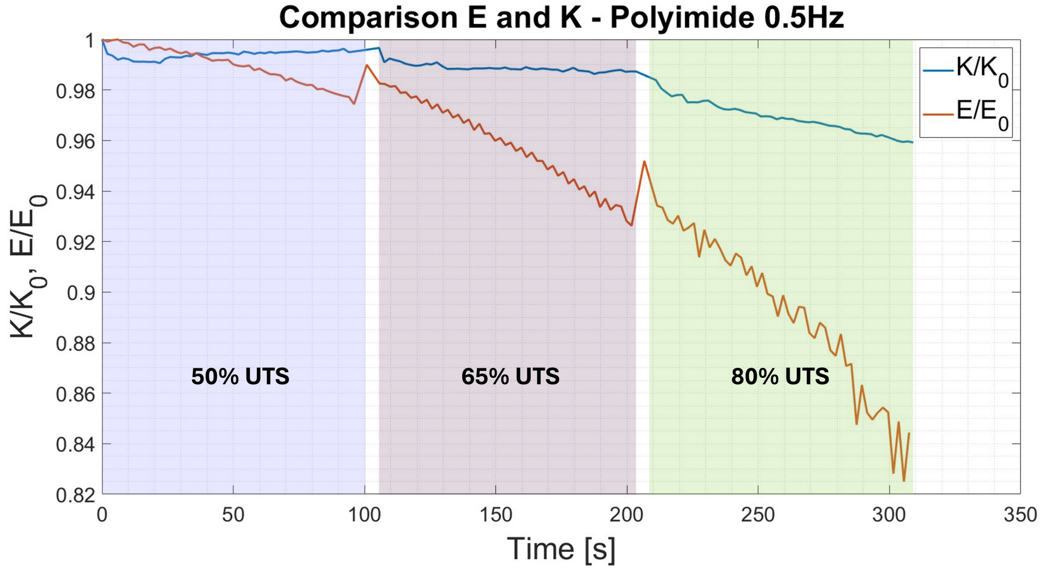

Figure 7.21: Comparison E-K of polyimide-coated fibre at 0.5Hz.

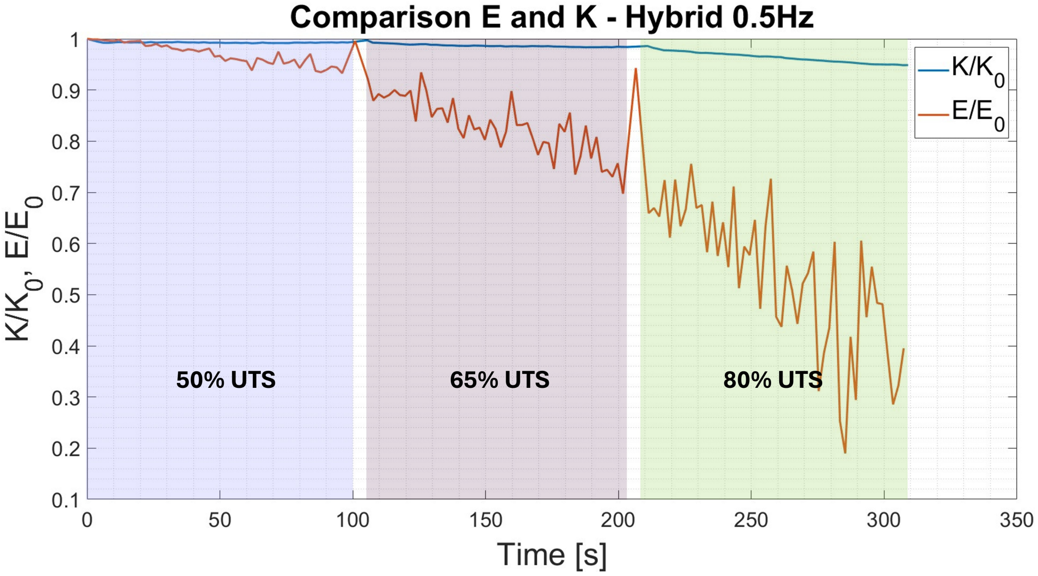

Figure 7.22: Comparison E-K of hybrid fibre at 0.5Hz.

Figures 7.20, 7.21, 7.22 indicate that the polyimide-coated and hybrid fibres measure strain accurately enough to provide a realistic elastic modulus. However, when the results are examined across the different load levels, the modulus trend is not reproduced consistently. Moreover, as the applied load increases, missing values become more frequent, which reduces the reliability of the modulus estimate and leads to a less robust trend.

Conversely, the fully acrylate-coated fibre, although it does not measure the absolute strain accurately, since part of the laminate deformation is absorbed by the coating rather than transmitted to the fibre core, does follow the expected modulus trend across the load levels.

The trends of the elastic moduli derived from the three optical fibre configurations at 0.5 Hz are shown in Figure 7.23 to highlight their differences.

The same analysis of the elastic modulus was also carried out for the tests performed at the higher frequencies, and the corresponding results are summarised in Figures 7.25 and 7.27. In particular, it can be observed that, as the test frequency increases, the elastic modulus evaluation becomes progressively less accurate due to the marked rise in missing values.

To better highlight the trend of the elastic modulus measured by the different optical fibres, the normalised elastic modulus was also plotted, as shown in Figures 7.24 and 7.26. It can be observed that, although the absolute modulus obtained with the fully acrylate-coated fibre is overestimated, its percentage decrease is captured correctly. The opposite behaviour is observed for the fully polyimide-coated and hybrid fibres, for which the absolute modulus is more representative but the relative reduction is not reproduced as reliably.

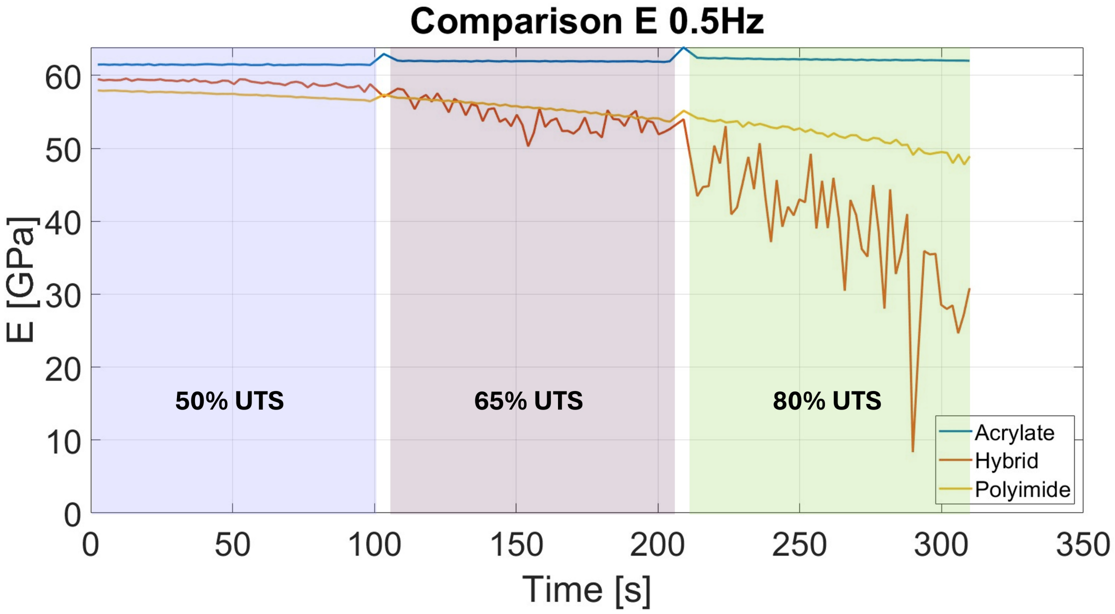

Figure 7.23: Comparison of the elastic modulus at different loading levels at 0.5 Hz for the three optical fibres.

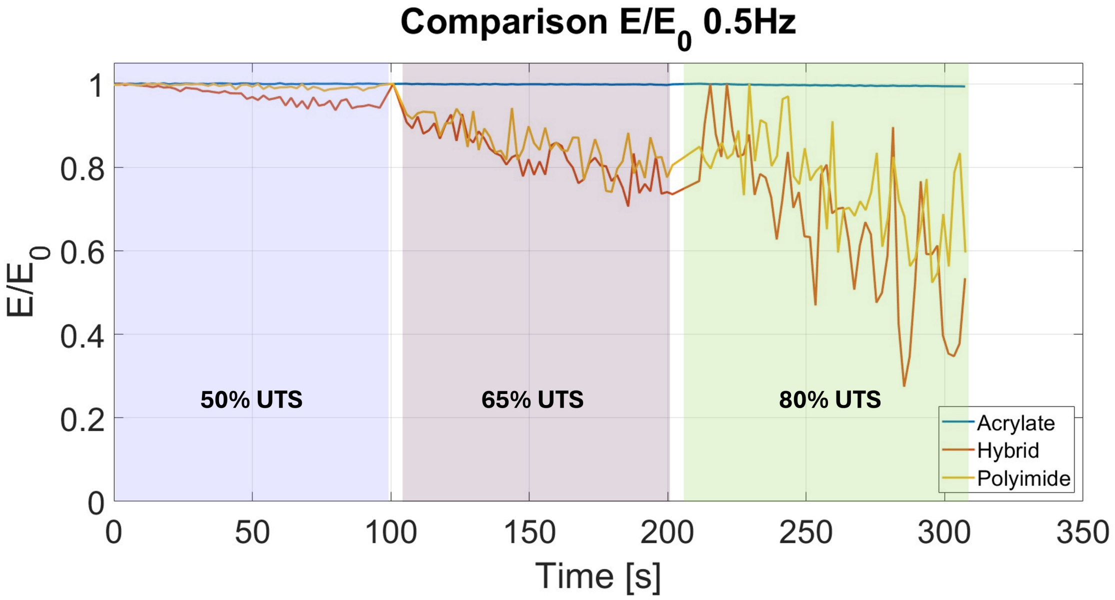

Figure 7.24: Comparison of the normalized elastic modulus at different loading levels at 0.5 Hz for the three optical fibres.

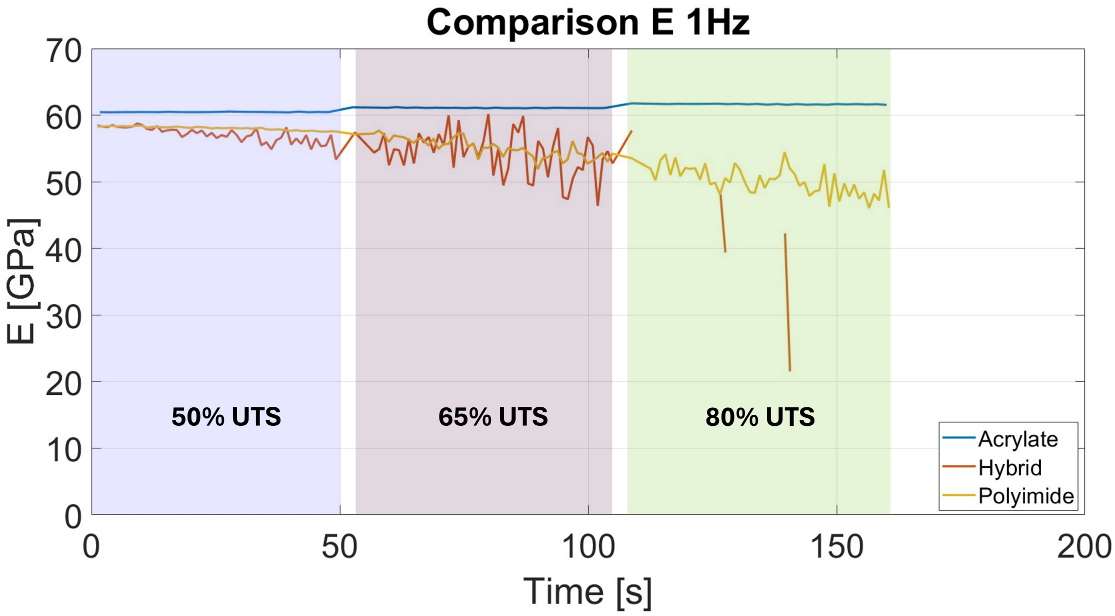

Figure 7.25: Comparison of the elastic modulus at different loading levels at 1 Hz for the three optical fibres.

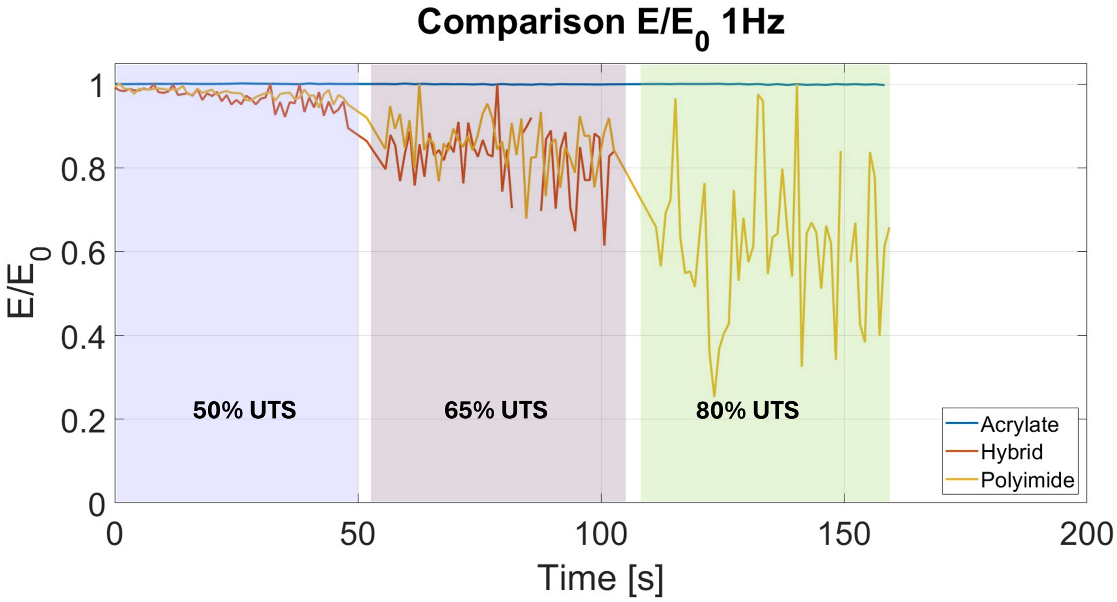

Figure 7.26: Comparison of the normalized elastic modulus at different loading levels at 1 Hz for the three optical fibres.

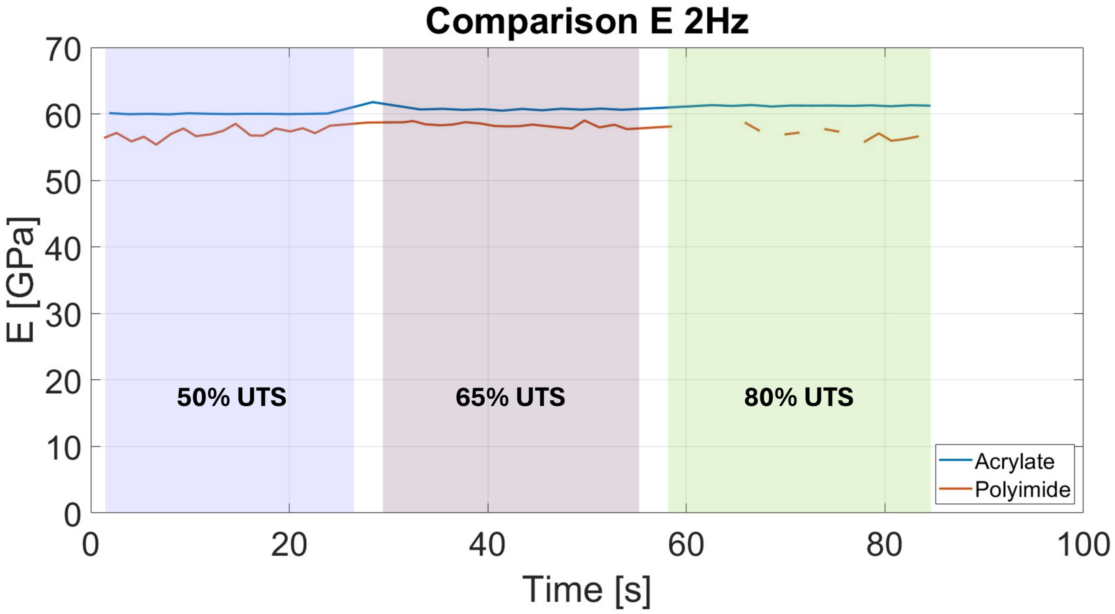

Figure 7.27: Comparison of the elastic modulus at different loading levels at 2 Hz.

7.2.2 Missing Value Count

Throughout this fatigue campaign, the presence of missing values had a strong impact on the strain measurements and, consequently, on the derived elastic modulus. It is therefore important to quantify and discuss their occurrence, in particular how the proportion of missing values increases with both load level and test frequency, and how this effect varies depending on the optical fibre configuration adopted, as shown in Figures 7.28, 7.29, 7.30. A clear and consistent trend emerges: the fraction of missing data increases with both frequency and load level, eventually reaching values that make the strain-based evaluation of the elastic modulus unreliable.

For the acrylate-coated fibre (Figure 7.28), missing values are essentially negligible at 0.5 Hz, and in particular absent for the 50% UTS (as shown in the results of previous section), while remaining limited at 1 Hz, with a noticeable increase only at the highest load level. The situation changes markedly at 2 Hz and 5 Hz, where the percentage of missing points becomes substantial and grows further as the stress level is increased, reaching the highest values at 80% UTS.

The polyimide-coated fibre (Figure 7.29) exhibits a systematically higher incidence of missing values across all conditions. Even at 0.5 Hz, approximately one fifth of the data is missing, and the percentage rises sharply with frequency. At 5 Hz, the missing fraction approaches saturation, particularly at 80% UTS, indicating that the acquisition becomes critically intermittent under the most demanding conditions.

The hybrid fibre (Figure 7.30), evaluated at 0.5 Hz and 1 Hz, shows comparatively high missing-value levels already at 50% UTS, with a further increase as the stress level is raised: 1 Hz consistently produces a higher proportion of missing data than 0.5 Hz, confirming the pronounced frequency sensitivity observed for the other coatings.

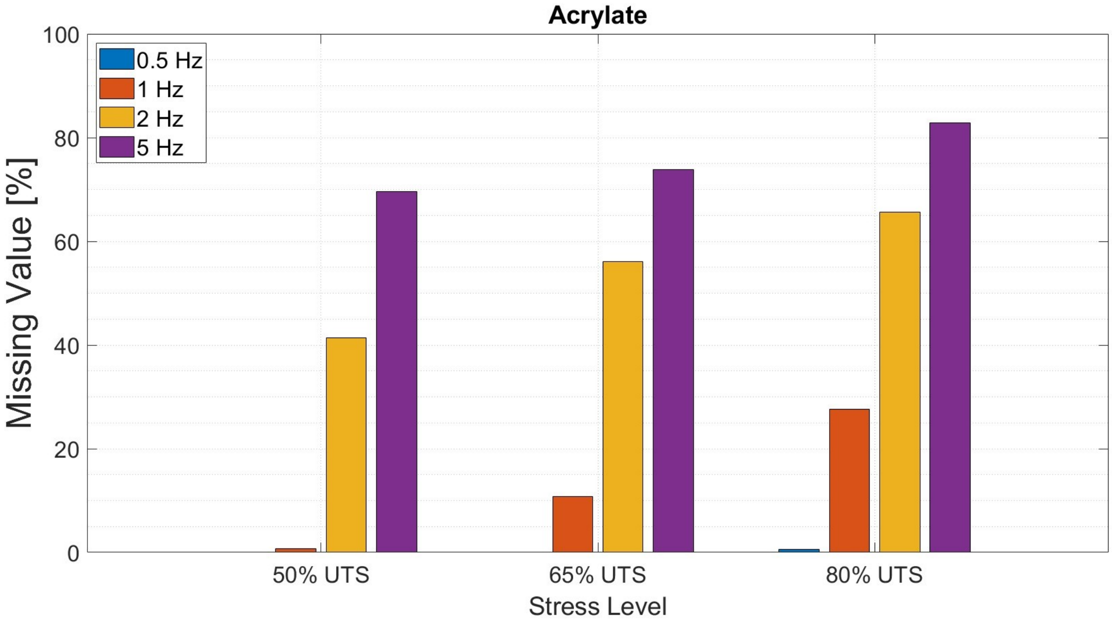

Figure 7.28: Acrylate Missing Values at different load levels and frequencies.

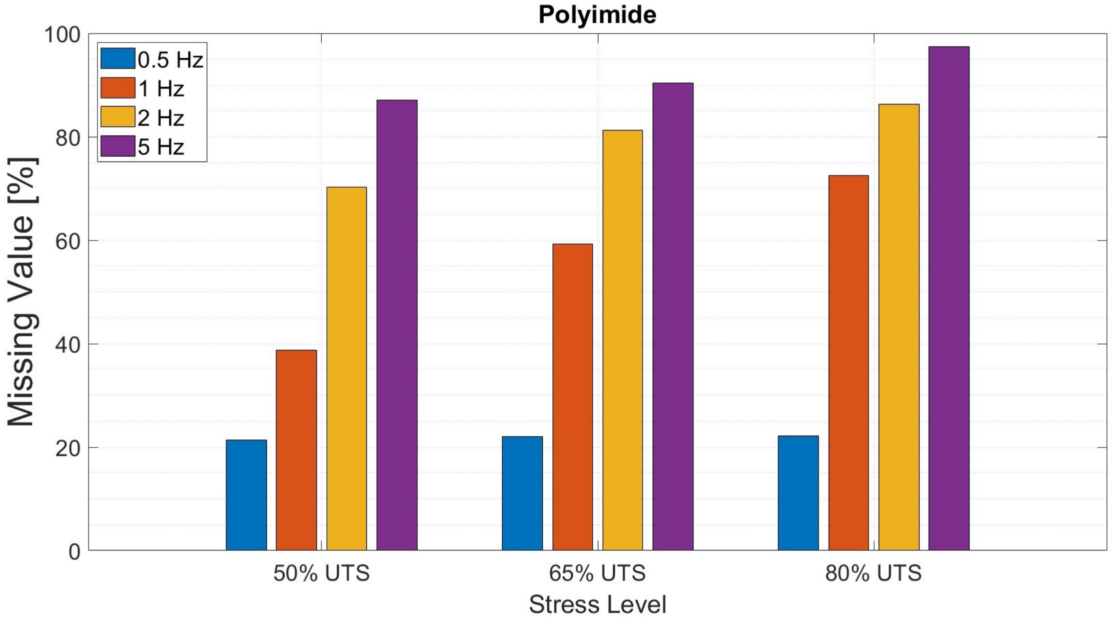

Figure 7.29: Polyimide Missing Values at different load levels and frequencies.

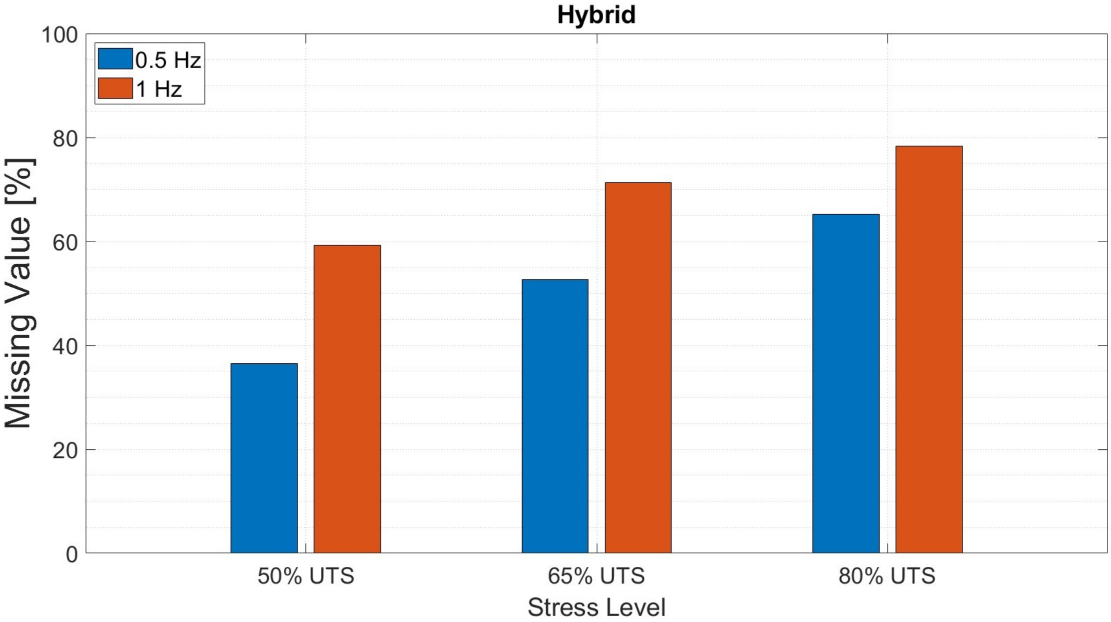

Figure 7.30: Hybrid Missing Values at different load levels and frequencies.

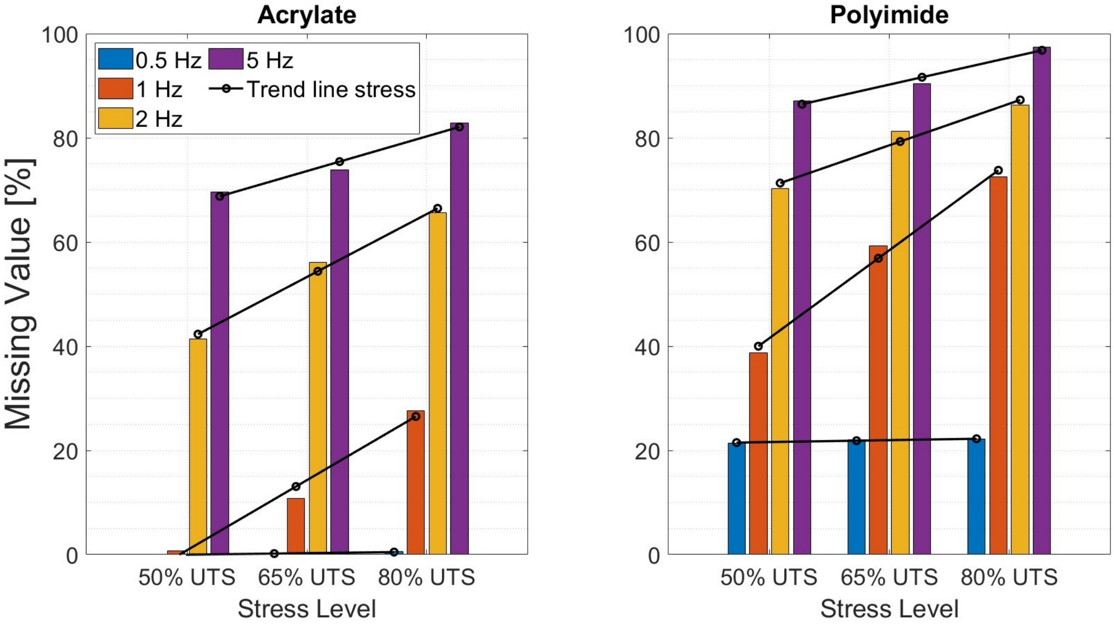

Figure 7.31: Comparison between Acrylate and Polyimide Missing Values at different stress levels and frequencies.

The direct comparison in Figure 7.31 further highlights that, at equal frequency and stress level, polyimide is more prone to missing data than acrylate. While both coatings show a strong deterioration as frequency increases, the separation between the two is most evident at the lower frequencies, where the acrylate-coated fibre still provides largely continuous datasets whereas the polyimide-coated fibre already suffers from significant data loss. Overall, these results indicate that frequency is the dominant driver for missing values, with load level acting as an additional aggravating factor, and with a clear dependence on fibre coating.

7.2.3 Reliability of the Optical Fibre with Time

After investigating if the optical fibres can measure strain across different load levels and test frequencies, the next step was to determine whether this capability deteriorates after prolonged fatigue cycling.

To this end, all three specimens were first subjected to a given number of tension–tension fatigue cycles at 80% UTS and 5 Hz. Following this conditioning phase, the fatigue test was slowed to 0.1 Hz and repeated at 80% UTS, for 5 cycles, while the strain response was acquired using the Luna ODiSI system. The choice of the low frequency of 0.1 Hz was motivated by the need to obtain stable strain measurements and to minimise the occurrence of NaN values in the exported TSV data, which had been observed at higher frequencies.

After completing the measurement sequence, the specimens were again cycled at 80% UTS and 5 Hz for an additional number of cycles, and subsequently re-tested under the same 0.1 Hz measurement protocol at the three load levels. This procedure was repeated iteratively until final fracture of the specimens. In this way, the investigation assessed both the survivability of the optical fibres (i.e., whether they remained intact until laminate failure) and their ability to continue providing accurate strain measurements throughout the fatigue life.

Referring to the following figure, the elastic modulus trend obtained from the optical fibre is compared with the stiffness evolution derived exclusively from the testing machine data.

The fully acrylate-coated fibre shows a stable measurement behaviour even after repeated fatigue intervals at 5 Hz. During the 80% UTS blocks at 5 Hz, the fibre does not break, yet the interrogation returns predominantly missing values and the modulus cannot be evaluated reliably. However, as soon as the test frequency is reduced to 0.1 Hz, while maintaining the same load level, the fibre resumes normal operation and provides continuous strain data, with no NaN values preventing the modulus estimation, as illustrated in Figure 7.33. The same procedure was applied to both polyimide-coated and hybrid optical fibres. In particular, the polyimide-coated fibre was able to capture strain once the test frequency was reduced to 0.1 Hz; however, after 4000 cycles, the specimen failed prematurely. Conversely, the hybrid optical fibre produced less reliable results at 80% UTS and subsequently suffered damage after only a few cycles at high frequency.

Overall, the acrylate-coated fibre emerges as the most robust option for monitoring strain under cyclic loading, particularly in terms of continuity of acquisition. Nevertheless, its intrinsic tendency to underestimate the true laminate strain, due to partial strain absorption within the coating, suggests that further work is required to quantify this effect and develop an appropriate compensation strategy, which is left for future investigations.

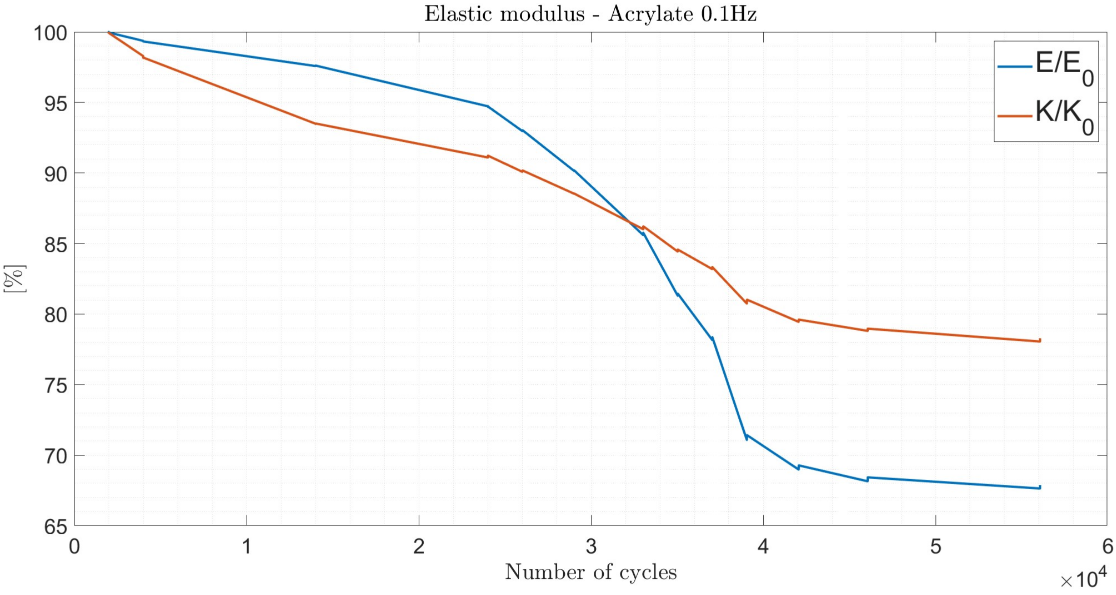

Figure 7.32: Comparison between elastic modulus and stiffness of the acrylate optical fibre subjected to iterative cycling.

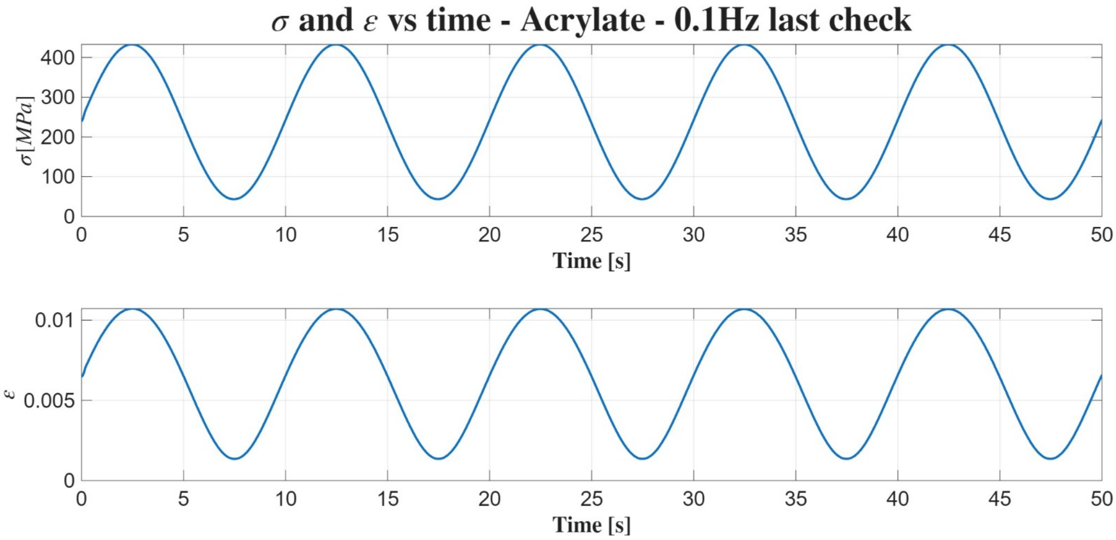

Figure 7.33: Last check to assess the optical fibre reading capability at 7000 cycles before the rupture.

7.3 Fracture surface observations

At the end of the fatigue tests at 80% UTS, which led to final fracture of the specimens, the broken samples were examined using a digital microscope in order to characterise the failure regions. The images reported below reveal several damage mechanisms that are typical of composite laminates subjected to tension–tension fatigue loading.

In particular, delamination is evident in Figure 7.34: rather than a clean, planar cut, the fracture surface shows a stepped profile, with plies locally separated, opened, and overlapping. In Figures 7.36, 7.37, and 7.38 a clear fibre pull-out morphology can be observed, indicative of progressive bundle debonding and failure, with the characteristic "brooming" appearance of fractured fibres; the presence of tow splitting can also be observed, giving the impression that a fibre tow detaches or separates along its length. In addition, the presence of dark lines and, especially, small voids along the boundaries of the fibre bundles suggests interfacial debonding and matrix cracking. Finally, a number of bright discontinuities are visible; these features are consistent with local resin-rich pockets, which are often associated with stress concentrations and may promote crack initiation and subsequent delamination.

In Figures 7.38 and 7.39, it is noteworthy that the optical fibre left a distinct groove on the two plies between which it had been embedded. This observation reinforces the idea that, even though the embedded fibre did not substantially alter the fatigue response in this specific configuration (i.e., tension–tension loading with the load applied along the fibre longitudinal direction), it still represents a local discontinuity, a flaw [39], within the laminate. For this reason, its role as a potential defect should be considered.

Figures 7.40 and 7.41 show the opposite fracture surface, where the optical fibre is still present. The fibre appears to be broken only at the location corresponding to the specimen fracture. Extensive delamination exposes the fibre, which remains resting along the surface of one ply. Moreover, a portion of the polyimide coating seems to have been locally removed, most likely during the laminate cure, without any macroscopic evidence of damage to the fibre core.

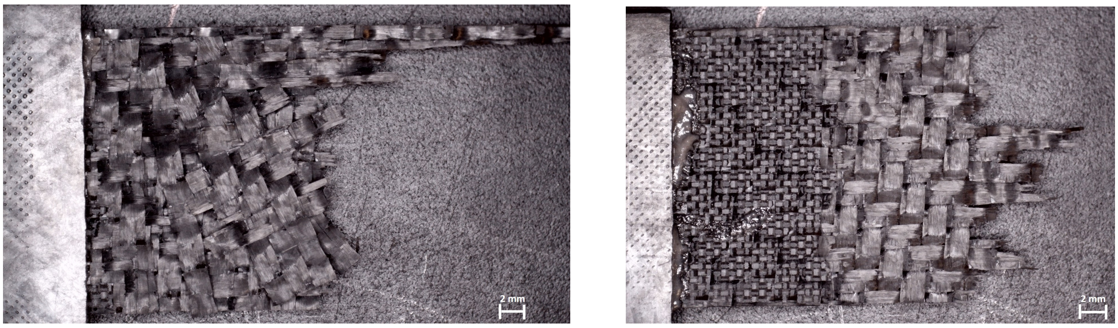

(a) (b)

Figure 7.34: Two specimens showing fibre breakage, delamination, and fibre pull-out.

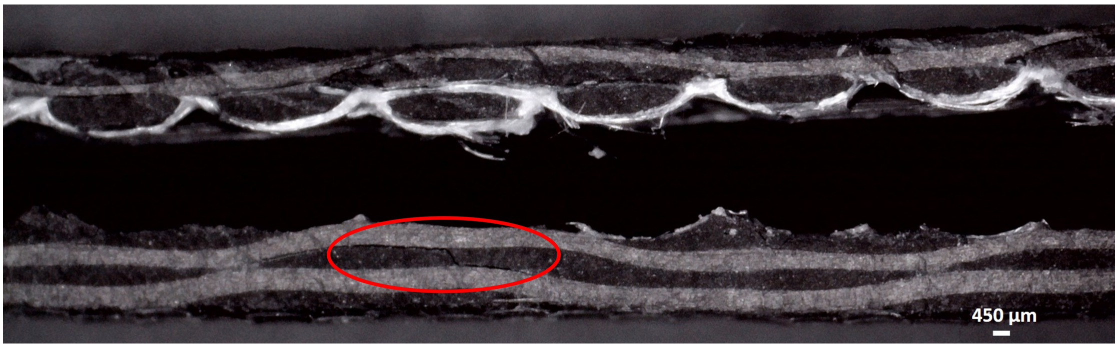

Figure 7.35: Thickness view of a specimen, fractured at the interface between the second and third ply, with evidence of the start of delamination also between the first and second ply, as highlighted by the red circle.

Figure 7.36: Enlargement of the fracture surface with small voids consistent with resin-rich pockets.

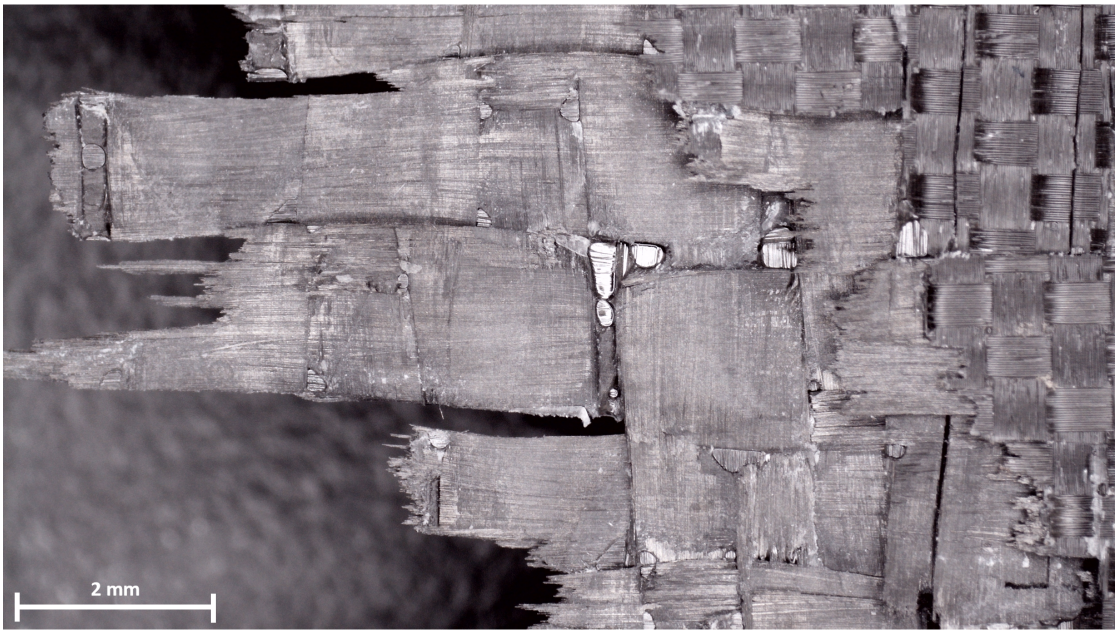

Figure 7.37: Presence of light-coloured resin pockets as well as fibre breakage, with the characteristic "brooming" aspect.

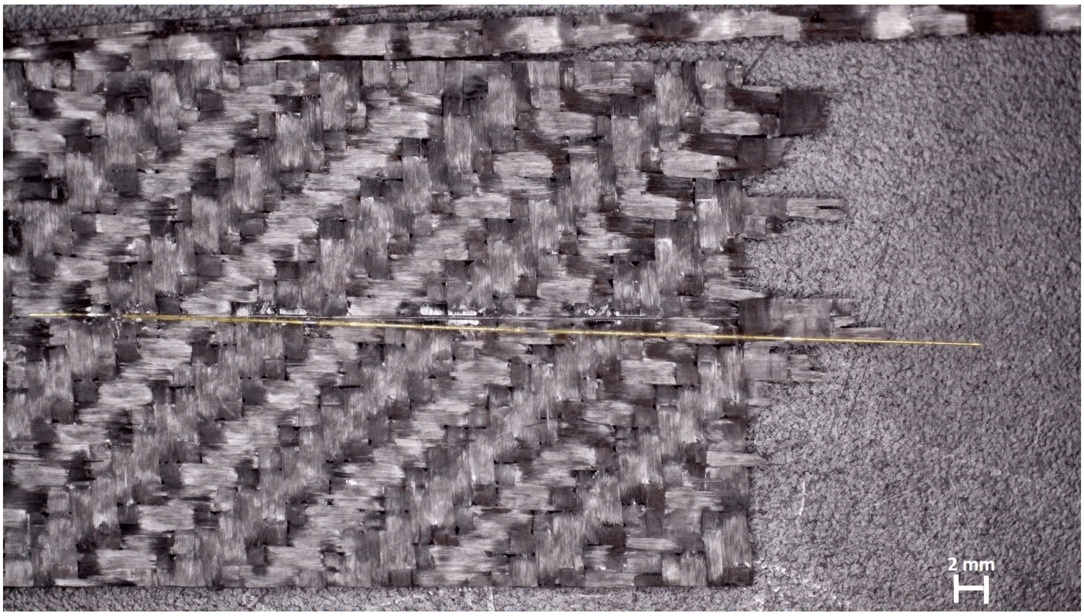

Figure 7.38: Specimen affected by extensive delamination and tow splitting, with the upper ply no longer visible; the optical fibre can be identified, together with the imprint left by it on the prepreg surface.

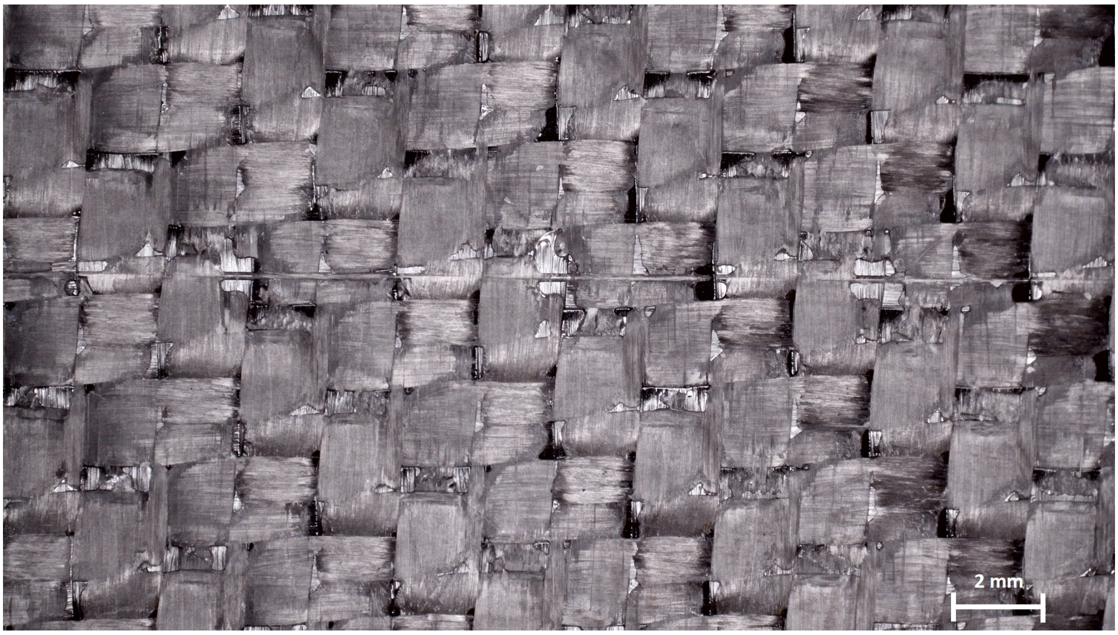

Figure 7.39: Groove left by the optical fibre along the length of the specimen.

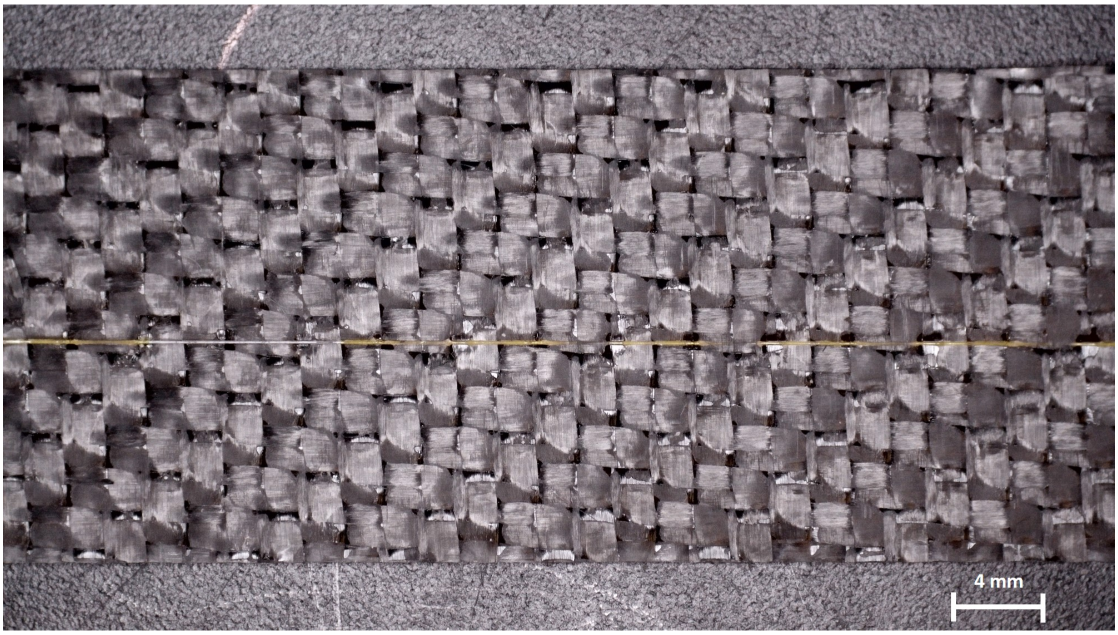

Figure 7.40: View of the full specimen width, traversed longitudinally by the embedded optical fibre.

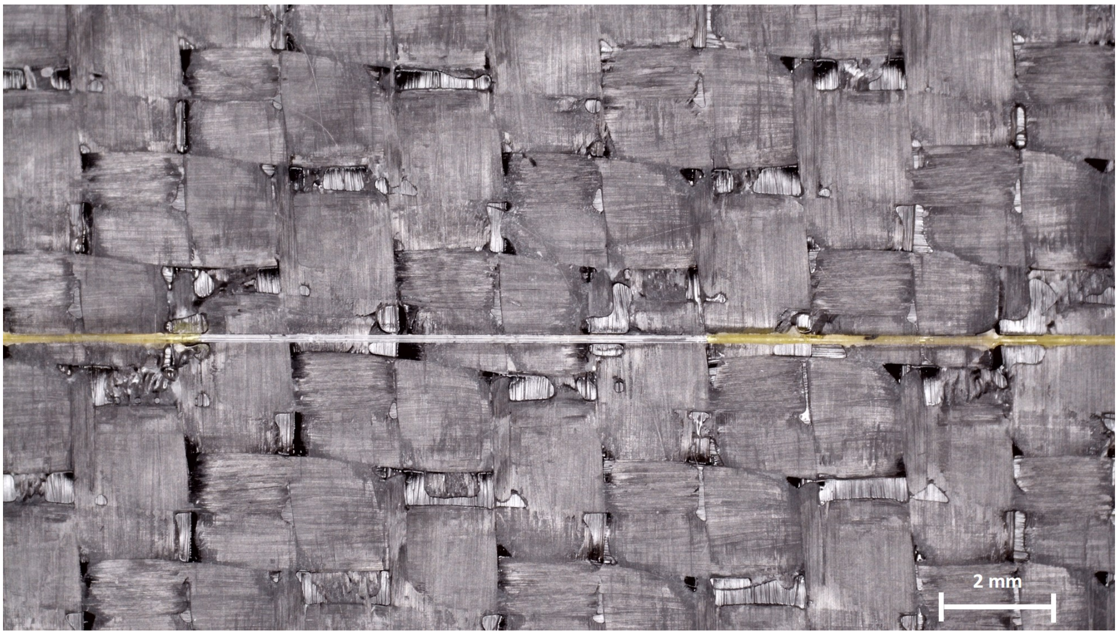

Figure 7.41: Enlargement of the previous image, showing that a portion of the polyimide coating is missing, while the fibre core does not appear to be damaged, at least at the macroscopic scale.


(a)

(b)

Figure 7.42: Specimen showing delamination, still gripped in the machine (a), and its broken surface in (b).

Figure 7.42 shows one of the specimens still mounted in the Instron testing machine at the end of a fatigue test. A pronounced delamination is clearly visible and is the damage mechanism that ultimately led to the final fracture of the sample. Lastly, Figure 7.43 shows a comparison between the fracture of a specimen after fatigue loading, and that of two specimens subjected to quasi-static tensile testing.

(a) (b)

Figure 7.43: Comparison between specimen broken after fatigue cycling (a), and after quasi-static tensile testing (b).

Chapter 8

Conclusions and Future Developments

This thesis addressed the integration of Rayleigh-based DFOS into carbon/epoxy composite laminates for SHM applications, with a particular focus on an embedded hybrid optical fibre configuration combining acrylate and polyimide-coated sections. The hybrid concept was conceived to retain the high strain-transfer fidelity typically associated with polyimide coatings, while improving handling robustness at the laminate entry/exit regions through the more compliant acrylate-coated portions.

A first validation step was performed under quasi-static tensile loading. Strain profiles acquired along the embedded fibre confirmed the expected behaviour of the two coatings: the polyimide-coated section reproduced the laminate deformation more faithfully, whereas the acrylate-coated section tended to underestimate strain due to the partial deformation absorption within the coating. Moreover, the elastic modulus derived from the hybrid fibre was found to be comparable to values reported for specimens instrumented with fully polyimide-coated fibres, validating its strain-sensing capability.

The experimental campaign was then extended to tension–tension fatigue loading with a twofold aim: to determine whether embedding an optical fibre affects the laminate fatigue response, and to evaluate whether DFOS can provide reliable strain measurements under cyclic loading across different stress levels and frequencies. Several damage metrics were adopted to interpret the fatigue response. A stiffness-based damage index reproduced the typical evolution observed in composite laminates under cyclic loading: an initial rapid increase, a stabilisation phase, and a final acceleration close to failure. In parallel, hysteresis-loop analysis confirmed the progressive widening of force–displacement loops with cycling, consistent with increasing dissipation associated with microcracking, debonding, and interfacial sliding.

The results indicate that embedding the fibre between plies (second/third) does not lead to a measurable reduction in stiffness evolution or fatigue life in the investigated configuration. At 50% and 65% UTS, all specimens reached the run-out limit of 10^6 cycles; despite the stiffness losses and visible damage (e.g., delamination and cracking), no meaningful differences emerged between "smart" and reference specimens in terms of

stiffness degradation rate.
At 80% UTS, all specimens failed, with scatter in cycles to fracture primarily due to manufacturing-related imperfections, rather than to the presence of the optical fibre itself. Consistently, specimen failure tended to occur once the normalised stiffness had decreased by approximately 20–25%, suggesting a practically relevant stiffness-loss threshold for defining damage states prior to catastrophic fracture.

S–N curves were constructed by adopting a stiffness-reduction criterion to define "failure", in addition to complete fracture. In order to statistically assess whether the embedded fibre influenced fatigue life, an ANOVA test was applied, demonstrating that the two populations (with and without embedded fibre) are not statistically different under the conditions examined.

Regarding DFOS strain measurements under fatigue, the experimental evidence highlights a trade-off between strain-transfer fidelity and data continuity that depends strongly on the coating type, load level, and test frequency. At low frequency (0.5 Hz), the acrylate-coated fibre tracked the strain signal at all load levels, but systematically underestimated strain, leading to an apparently higher elastic modulus. Conversely, the polyimide-coated and hybrid fibres provided more faithful strain amplitudes (and therefore more realistic modulus values), in line with the expected strain-transfer behaviour of stiffer coatings. However, under demanding conditions such as high load and/or high frequency, polyimide-coated sensors exhibited a pronounced rise in missing values, thus resulting in an unreliable modulus evaluation.
A systematic comparison of missing-value occurrence confirmed that frequency is the dominant driver, with load level acting as an aggravating factor, and with polyimide showing higher sensitivity than acrylate at comparable conditions.

Finally, an iterative "conditioning + measurement" routine proved that the sensing capability of the acrylate-coated optical fibre does not deteriorate after repeated high-stress cycling. This indicates that the loss of data at high frequency is not necessarily associated with fibre rupture, but rather with acquisition limitations under high-strain conditions; nonetheless, the acrylate underestimation of absolute strain motivates further work aimed at quantifying and compensating the coating-related transfer effect.

Based on these outcomes, future work should primarily focus on improving measurement robustness while preserving the advantages observed for each fibre configuration. In particular, a calibrated strain-transfer compensation for acrylate-coated fibres would be valuable to correct the systematic underestimation of absolute strain without sacrificing their strong acquisition continuity under cyclic loading. In parallel, the high incidence of missing values observed with polyimide-based solutions requires a dedicated investigation to clarify its underlying causes, ranging from interrogator settings and strain range limitations to local debonding or microbending effects, and to identify operating windows in the frequency–load domain where acquisition remains reliable. Finally, the mechanical assessment should be extended to different laminate architectures and loading scenarios, such as transverse loading with respect to the fibre direction, variable-amplitude spectra, or multiaxial conditions, where an embedded fibre could act as a more critical stress concentrator than in the present longitudinal tension–tension configuration.

Bibliography

[1] R. Phiri, S. Mavinkere Rangappa, S. Siengchin, O. P. Oladijo, and T. Ozbakkaloglu, "Advances in lightweight composite structures and manufacturing technologies: A comprehensive review," *Composite Structures*, 2024.

[2] A. K. Hamzat *et al.*, "Fiber-reinforced composites for aerospace, energy, and marine applications: an insight into failure mechanisms under chemical, thermal, oxidative, and mechanical load conditions," *Advanced Composites and Hybrid Materials*, vol. 8, 2025. Article 152.

[3] D. K. Rajak *et al.*, "A review on synthetic fibers for polymer matrix composites," *Materials*, vol. 15, no. 1, 2022.

[4] C. Wu *et al.*, "Manufacturing technologies of polymer composites—a review," *Polymers*, vol. 15, no. 3, 2023.

[5] M. Bukvić, S. Milojević, S. Gajević, M. Đorđević, and B. Stojanović, "Production technologies and application of polymer composites in engineering: A review," *Polymers*, vol. 17, p. 2187, 2025.

[6] H. Sharma, A. Kumar, S. Rana, N. G. Sahoo, M. Jamil, R. Kumar, S. Sharma, C. Li, A. Kumar, S. M. Eldin, and M. Abbas, "Critical review on advancements on the fiber-reinforced composites: Role of fiber/matrix modification on the performance of the fibrous composites," *Journal of Materials Research and Technology*, 2023.

[7] H. H. Parikh *et al.*, "Tribology of plant-based natural fiber reinforced polymer matrix composites – a short review," *Journal of Natural Fibers*, vol. 20, no. 1, p. 2172639, 2023.

[8] J. Qureshi *et al.*, "A review of fibre reinforced polymer structures," *Journal of Composite Science*, vol. 10, no. 3, 2022.

[9] Y. S. Mohamed *et al.*, "Theoretical and experimental study on the influence of fiber orientation on the tensile properties of cfre composites," *Composites Communications*, 2023.

[10] I. R. Chowdhury *et al.*, "Woven fabrics for composite reinforcement: A review," *Journal of Composite Science*, vol. 8, no. 7, 2024.

[11] H. Ning, *Thermoplastic Composites: Principles and Applications.* De Gruyter, 2021.

[12] Y. Qiao, L. Fring, M. R. Pallaka, and K. Simmons, “A review of the fabrication methods and mechanical behavior of continuous thermoplastic polymer fiber–thermoplastic polymer matrix composites,” *Polymer Composites*, 2023.

[13] C. Badini, *Materiali compositi per l’ingegneria.* Torino, 2013.

[14] S. R. Udupi and L. L. Raj Rodrigues, “Detecting safety zone drill process parameters for uncoated hss twist drill in machining gfrp composites by integrating wear rate and wear transition mapping,” *Indian Journal of Materials Science*, 2016. Fig. 1.

[15] EPP Composites Pvt Ltd, “RTM Process.” `https://www.eppcomposites.com/rtm-process.html`. Accessed: 2025-09-22.

[16] Heatcon Composite Systems, “Composite lay-up schedule diagram.” `https://www.heatcon.com/composite-lay-up-schedule/`. Accessed: 2025-10-04.

[17] T. Baran, *Analysis of pultrusion process for thick glass/polyester composites: transverse shear stress formations.* PhD thesis, University of Twente, Enschede, The Netherlands, 2016. Fig. 1.

[18] ADD Composites, “Filament winding process.” `https://www.addcomposites.com/post/filament-winding`, 2024. Blog post, accessed: 2025-11-10.

[19] A. Sayam *et al.*, “A review on carbon fiber-reinforced hierarchical composites,” *Composites Part B: Engineering*, 2022.

[20] S. Hassani, M. Mousavi, and A. H. Gandomi, “Structural health monitoring in composite structures: A comprehensive review,” *Sensors*, vol. 22, no. 1, p. 153, 2022.

[21] V. Giurgiutiu, “Structural health monitoring (shm) of aerospace composites,” in *CAMX Proceedings*, University of South Carolina, 2015.

[22] A. Güemes *et al.*, “Structural health monitoring in composite structures: A review,” *Materials*, vol. 13, no. 2, p. 372, 2020.

[23] I. Herszberg *et al.*, “Structural health monitoring of composite structures—challenges and opportunities,” in *Proceedings of ICCM-16*, 2006.

[24] X. Li *et al.*, “Recent advances in self-sensing composite structures,” *Advanced Composites and Hybrid Materials*, 2025. Springer.

[25] S. Mustapha *et al.*, “Structural health monitoring of cfrp using guided waves,” *Journal of Vibroengineering*, vol. 14, no. 2, pp. 683–693, 2012.

[26] B. Glisic, “Concise historic overview of strain sensors used in the monitoring of civil structures: The first one hundred years,” *Sensors*, vol. 22, no. 6, p. 2397, 2022.

[27] J. M. Senior, *Optical Fiber Communications: Principles and Practice.* Harlow: Pearson Education, 3 ed., 2009.

[28] The Fiber Optic Association, "Total internal reflection – the basic principle of optical fiber." FOA Online Reference Guide to Fiber Optics, 2018. Accessed: 2025-05-24.

[29] J. Hecht, *Understanding Fiber Optics.* London: Pearson Education, 6 ed., 2015.

[30] B. E. A. Saleh and M. C. Teich, *Fundamentals of Photonics.* Hoboken, NJ: Wiley-Interscience, 2 ed., 2007.

[31] G. P. Agrawal, *Fiber-Optic Communication Systems.* New York: Wiley-Interscience, 3 ed., 2002.

[32] A. Barrias, J. R. Casas, and S. Villalba, "A review of distributed optical fiber sensors for civil engineering applications," *Sensors*, vol. 16, no. 5, p. 748, 2016.

[33] P. Lu, N. Lalam, M. Badar, B. Liu, B. T. Chorpening, M. P. Buric, and P. R. Ohodnicki, "Distributed optical fiber sensing: Review and perspective," *Applied Physics Reviews*, vol. 6, no. 4, p. 041302, 2019.

[34] A. D. Kersey, M. A. Davis, H. J. Patrick, M. LeBlanc, K. P. Koo, C. G. Askins, M. A. Putnam, and E. J. Friebele, "Fiber grating sensors," *Journal of Lightwave Technology*, vol. 15, no. 8, pp. 1442–1463, 1997.

[35] D. Kinet, P. Mégret, K. W. Goossen, L. Qiu, D. Heider, and C. Caucheteur, "Fiber bragg grating sensors toward structural health monitoring in composite materials: Challenges and solutions," *Sensors*, vol. 14, no. 4, pp. 7394–7419, 2014.

[36] S. J. Mihailov, "Fiber bragg grating sensors for harsh environments," *Sensors*, vol. 12, no. 2, pp. 1898–1918, 2012.

[37] L. Palmieri, L. Schenato, M. Santagiustina, and A. Galtarossa, "Rayleigh-based distributed optical fiber sensing," *Sensors*, vol. 22, no. 18, p. 6811, 2022.

[38] M. F. Bado, J. R. Casas, and A. Barrias, "Performance of rayleigh-based distributed optical fiber sensors bonded to reinforcing bars in bending," *Sensors*, vol. 18, no. 9, p. 3125, 2018.

[39] M. Drissi-Habti and V. Raman, "Fatigue behavior of smart composites with distributed fiber optic sensors for offshore applications," *Journal of Composites Science*, vol. 6, no. 1, p. 2, 2022.

[40] D. Bin Zainal Abidin, S. Theminimulla, D. Waugh, and J. Griffin, "Optical fibers in composite materials: The effects on mechanical properties under flexural and tensile loading and acoustic emission monitoring," *Proceedings of the Institution of Mechanical Engineers, Part C: Journal of Mechanical Engineering Science*, vol. 236, no. 16, pp. 9169–9185, 2022.

[41] M. Gabardi, L. Tozzetti, S. Faralli, M. Solazzi, D. Benedetti, S. Rajbhandari, G. Buttaro, and F. Di Pasquale, "Embedding fiber bragg grating sensors in carbon composite structures for accurate strain measurement," *IEEE Sensors Journal*, vol. 23, no. 15, pp. 16882–16892, 2023.

[42] Quest Global Services, "Novel technique of embedding fibre optic sensors for curved composites for structural health monitoring," 2015. Technical report / conference paper.

[43] A. E. S. Nosseir, E. A. Slejko, A. Cervone, C. J. Oton, and F. Di Pasquale, "Composite structures with embedded fiber optic sensors: A smart propellant tank for future spacecraft applications," *Acta Astronautica*, vol. 223, pp. 144–158, 2024.

[44] D. Delbeke and A. Trita, "SMARTFIBER – miniaturized structural monitoring system with autonomous readout micro-technology and fiber sensor network," White paper D8.3, European Commission, 2012. FP7 Project 257733.

[45] X. Bao and L. Chen, "Recent progress in distributed fiber optic sensors," *Sensors*, vol. 12, no. 7, pp. 8601–8639, 2012.

[46] J. Li, X. Sun, L. Huang, and A. Stolov, "Optical fiber for distributed sensing in harsh environments," in *Fiber Optic Sensors and Applications XV*, vol. 10654 of *Proc. SPIE*, p. 106540E, 2018.

[47] Luna Innovations, "Odisi 6000 series data sheet — high-definition strain sensors (polyimide coated options)." `https://lunainc.com/products/odisi`, 2021. Technical datasheet.

[48] Luna Innovations, "High density fiber optic sensing (hd-fos) in composites — embedding fiber in composites," 2017. Technical white paper.

[49] S.-C. Her and C.-Y. Huang, "Effect of coating on the strain transfer of optical fiber sensors," *Sensors*, vol. 11, no. 7, pp. 6926–6941, 2011.

[50] C. Boursier Niutta, A. Tridello, R. Ciardiello, and D. S. Paolino, "Strain measurement with optic fibres for structural health monitoring of woven composites: Comparison with strain gauges and digital image correlation measurements," *Sensors*, vol. 23, p. 9794, 2023.

[51] M. Alemanni, "Strain measurement with rayleigh-based distributed fibre optic sensors in composite materials," Master's thesis, Politecnico di Torino, 2024.

[52] Thorlabs Inc., "Best practices for fiber cleaning and handling." `https://www.thorlabs.com`, 2023. Accessed: 2025-10-15.

[53] Fujikura Ltd., "Ct60 high precision fiber cleaver – technical specification sheet." `https://www.fujikura.co.jp/products/ct60`, 2023. Accessed: 2025-05-27.

[54] Fujikura Ltd., "90s+ fusion splicer – product datasheet and user manual." `https://www.fujikura.co.jp/products/90splus`, 2024. Accessed: 2025-05-24.

[55] AFL Global, "Heatshrink splice protectors – product specification sheet." `https://www.aflglobal.com`, 2023. Accessed: 2025-05-24.

[56] Easy Composites Ltd., "Xc110 epoxy prepreg carbon fibre datasheet, rev. 2.0." `https://www.easycomposites.co.uk/xc110-epoxy-prepreg-carbon-fibre`, 2023. Accessed: 2025-07-27.

[57] Easy Composites Ltd., "Pp230 peel ply technical datasheet, rev. 1.4." `https://www.easycomposites.co.uk/pp230-nylon-peel-ply`, 2023. Accessed: 2025-10-12.

[58] Easy Composites Ltd., "Sealant tape for vacuum bagging – product data sheet, rev. 2.1." `https://www.easycomposites.co.uk/sealant-tape`, 2023. Accessed: 2025-11-03.

[59] WAZER Inc., "Wazer g6 pro desktop waterjet cutter – technical specifications." `https://www.wazer.com/products/wazer-g6-pro`, 2024. Accessed: 2025-11-24.

[60] ASTM International, "Astm d3039/d3039m-17: Standard test method for tensile properties of polymer matrix composite materials," 2017.

[61] Sika AG, "Sikapower®-880 – two-component epoxy structural adhesive product data sheet." `https://industry.sika.com`, 2024. Accessed: 2025-11-14.

[62] Luna Innovations Inc., "Odisi 6100 user manual – system configuration and fibre calibration, rev. 3.0." `https://lunainc.com`, 2024. Accessed: 2025-08-04.

[63] H. Park, S. Yoon, and Y. Kim, "High-resolution optical frequency domain reflectometry for distributed sensing applications," *IEEE Photonics Technology Letters*, vol. 34, no. 3, pp. 189–192, 2022.

[64] B. Soller, M. Froggatt, M. Wolfe, *et al.*, "Distributed strain and temperature measurement using optical backscatter reflectometry," in *Proc. SPIE – Smart Structures and Materials*, vol. 6933, pp. 69330A–1–69330A–10, 2008.

[65] Luna Innovations Inc., "Odisi software user guide – control, visualization, and data export functions, rev. 2.1." `https://lunainc.com`, 2024. Accessed: 2025-09-10.

[66] Luna Innovations Inc., "Odisi remote measurement module user manual." `https://lunainc.com/support`, 2023. Accessed: 2025-09-10.

[67] Thorlabs Inc., "Coreless silica fiber (csf) – product specification sheet." `https://www.thorlabs.com`, 2024. Accessed: 2025-08-24.

[68] ZwickRoell GmbH & Co. KG, "Allroundline – universal testing machines for static applications: Product overview." `https://www.zwickroell.com/products/static-materials-testing-machines/universal-testing-machines-for-static-applications/allroundline/`, 2024. Accessed: 2025-07-30.

[69] Instron, "8801 fatigue testing system – product brochure." `https://www.instron.com/en/products/testing-systems/dynamic-and-fatigue-systems/8801`, 2024. Accessed: 2025-10-22.

[70] G. M. Yash, M. V. Shankar, P. Acharya, I. V. Thara Reshma, C. R. Kini, K. Shahapurkar, and N. H. Padmaraj, “Stiffness degradation and fatigue damage evolution in treated ramie fibre-reinforced epoxy composites,” *Results in Engineering*, vol. 27, p. 106712, Sept. 2025.

[71] S. V. Panin, A. A. Bogdanov, A. V. Eremin, D. G. Buslovich, and V. O. Alexenko, “Estimating low- and high-cyclic fatigue of polyimide-cf-ptfe composite through variation of mechanical hysteresis loops,” *Materials*, vol. 15, no. 13, p. 4656, 2022.

[72] G. Meneghetti, M. Ricotta, G. Lucchetta, and S. Carmignato, “An hysteresis energy-based synthesis of fully reversed axial fatigue behaviour of different polypropylene composites,” *Composites Part B Engineering*, vol. 62, pp. 17–75, 10 2014.

[73] Y.-L. Lee, J. Pan, R. B. Hathaway, and M. E. Barkey, *Fatigue Testing and Analysis: Theory and Practice.* Butterworth-Heinemann, 2005.